PLACE IN RETURN BOX to remove this checkout from your record.
TO AVOID FINES return on or before date due.
MAY BE RECALLED with earlier due date if requested.

DATE DUE	DATE DUE	DATE DUE
NOV 2 1 2005		

6/01 c:/CIRC/DateDue.p65-p.15

A GE
CAD

A GENERAL FRAMEWORK FOR AUTOMATED CAD-GUIDED OPTIMAL TOOL PLANNING IN SURFACE MANUFACTURING

BY

Heping Chen

A DISSERTATION

Submitted to
Michigan State University
in partial fulfillment of the requirements
for the degree of

DOCTOR OF PHILOSOPHY

Department of Electrical and Computer Engineering

2003

A GENER

This disse

mal tool plan

add material

forming, ind

of surface m

Tool plannin

manufacturi

feasible any

design char

sues. An a

of industria

In surfa

a free-form

isfied. Ac

manufactu

age. Base

is divided

for auton

on a plan

planning.

performe

ABSTRACT

A GENERAL FRAMEWORK FOR AUTOMATED CAD-GUIDED OPTIMAL TOOL PLANNING IN SURFACE MANUFACTURING

By

Heping Chen

This dissertation develops a general framework for automated CAD-guided optimal tool planning in surface manufacturing. Surface manufacturing is a process to add material to or remove material from the surface of parts. Spray painting, spray forming, indirect rapid tooling, spray coating and polishing are typical applications of surface manufacturing. Industrial robots are used to implement these processes. Tool planning of these processes, which builds a bridge between product design and manufacturing, is crucial for the product quality. Typical teaching methods are not feasible any more because products are subject to a shorter product life, frequent design changes, small lot sizes, small in-process inventory restrictions and quality issues. An automated tool planning process (ATPP) is desirable for the tool planning of industrial robots.

In surface manufacturing, automated tool planning develops a tool trajectory for a free-form surface based on a tool model such that the given constraints are satisfied. According to the material distribution constraints, the processes in surface manufacturing can be categorized into two groups: material uniformity and coverage. Based on a tool model and material distribution constraints, a free-form surface is divided into patches. The parameters (the spray width and tool velocity) used for automated tool planning are determined by optimizing the material distribution on a plane. Since different material deposition patterns are used in automated tool planning, comparison between the raster and spiral material deposition patterns are performed. The raster material deposition pattern is better than the spiral one for

continuous n

bounding bo

pattern. Th

surface. Sin

sired materi

the material

integration a

verify if a tra

The impleme

planning alg

surface manu

To increas

for industrial

criteria. Op

ing using gi

is challengin

model, cons

planning wit

surface man

mulated. T

analysis. T

tool traject

The gen

mensional i

tool planni

nanodevice

ufacture n

continuous material deposition. After the spray width is determined, an improved bounding box method is developed to generate a path for a patch using the raster pattern. The tool orientation is determined using the local geometry of a free-form surface. Since the material deposited on the free-form surface is less than the desired material thickness, a suboptimal velocity algorithm is developed to optimize the material thickness deviation. For a free-form surface with multiple patches, an integration algorithm is developed to integrate the trajectories of the patches. To verify if a trajectory satisfies the given constraints, a verification model is developed. The implementation and simulation results show that the developed automated tool planning algorithm can be applied to generate trajectories for different processes in surface manufacturing such that the given constraints are satisfied.

To increase productivity and the quality of manufactured products, it is desirable for industrial robots to run in their optimal conditions subject to some optimization criteria. Optimal tool planning generates a tool trajectory in surface manufacturing using given optimization criteria. Optimal tool planning for industrial robots is challenging. Based on the CAD model of a free-form surface, along with a tool model, constraints and optimization criteria, a general framework for optimal tool planning with constant and non-uniform material distribution has been developed for surface manufacturing. Multi-objective constrained optimization problems are formulated. The implementation and simulation results are consistent with theoretical analysis. The developed optimal tool planning algorithm can be applied to generate tool trajectories in surface manufacturing.

The general framework can also be extended to other applications such as dimensional inspection and nanomanufacturing. A general framework for automated tool planning for nanoassembly in nanomanufacturing is developed to manufacture nanodevices and nanostructures. The algorithm is implemented successfully to manufacture nanostructures using an atomic force microscope (AFM).

For my mother, father, wife and daughter,

their love and support make my dream true.

Foremost

Dr. Xing X

comes from

a fruitful res

experience a

like to thank

Erik Goodm

meetings. T

soundness of

Robotics and

with Dr. Mu

and broaden

Carolyn Ha

my family, e

and contin

the Scientifi

Foundation

ACKNOWLEDGEMENTS

Foremost, I would like to acknowledge all the invaluable help from my advisor, Dr. Ning Xi, without whom this would not have been possible. This dissertation comes from numerous discussions in his office, from his keen insight and guidance in a fruitful research area, and his support. Not only the knowledge, but also the research experience and friendship I gained here will be beneficial for the rest of my life. I would like to thank all my committee members, Dr. Yifan Chen, Dr. Chichia Chiu, Dr. Erik Goodman and Dr. Fathi Salem, who have devoted many hours in the committee meetings. Their insightful comments and suggestions have enhanced the technical soundness of this dissertation. I am grateful to my friends and colleagues from the Robotics and Automation Laboratory and the Ford Motor Company. The discussions with Dr. Muming Song and Dr. Weihua Sheng substantially contributed to my work and broadened my knowledge. I would like to express my great appreciation to Mrs. Carolyn Haines and Mr. Ali Saeed for revising my dissertation. My thanks go to my family, especially my wife and my parents. Without their years of encouragement and continuous support, I would not have reached this point. I would like to thank the Scientific Research Laboratory of the Ford Motor Company and National Science Foundation for providing financial support for this research.

TABLE OF CONTENTS

4.3

LIST OF TABLES

LIST OF FIGURES

5.19 Ve
thi
5.20 Ve
thi
5.21 Th
cas

6.1 A p
6.2 Th
opt
6.3 Th
tim
6.4 Th
opt
6.5 Th
ma
6.6 Th
no
6.7 Th
enc
6.8 Th
pre
6.9 Th
art

7.1 De
doc
7.2 Th
opt
7.3 Th
tim
7.4 Th
op
7.5 Th
ma
7.6 Th
no
7.7 Th
en
7.8 Th
pr
7.9 Th
ar

8.1 A

CHAPTER 1

INTRODUCTION

Surface manufacturing is a process which adds material to or removes material from the surface of parts. Spray painting, spray forming, indirect rapid tooling, spray cleaning and polishing are typical examples of surface manufacturing. Industrial robots are used to implement these processes. The tool planning of these processes is crucial to satisfy some given constraints. Typical teaching methods are complex, time-consuming and the material distribution is dependent on the operator's skill. Automated optimal tool planning process (AOTPP) is desirable for planning trajectories for industrial robots. However, AOTPP for industrial robots in surface manufacturing is a challenging research topic.

This dissertation develops a general framework for automated optimal tool planning based on the CAD model of a free-form surface, a tool model, given constraints and optimization criteria in surface manufacturing. The following section gives the background that related to the research. The remaining sections of this chapter describe the previous work, motivation, objectives, contributions and organization of this dissertation.

1.1 Background

Recent trends have seen new constraints in product manufacturing. Examples of these constrains are a shorter product life, frequent design changes, small lot sizes, and reduced in-process inventory. Automation in manufacturing can satisfy these requirements, while providing flexibility and good quality products at a low cost. Automation has been studied and implemented successfully in many areas. Some examples are machining processes, material handling, inspection, welding, packaging, and surface manufacturing. With a pressing need to upgrade productivity, manufacturing indu

robots yield

Industrial r

have seen r

robots. A t

Produc

entities (fa

sired to pla

planning b

design info

facture pro

example of

planning tr

it greatly a

facturing p

and automa

Manual

neers' expe

processes, a

a work cell

turing industries are turning more and more toward robots. Compared to humans, robots yield more consistent quality, more predictable output and are more reliable. Industrial robots are one of the examples of automation equipment. Recent years have seen rapid developments in the areas of surface manufacturing using industrial robots. A typical production flow [1] is shown in Figure 1.1.

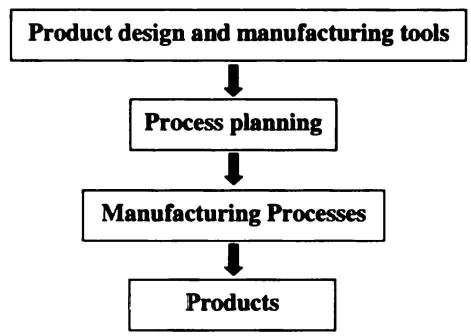

Figure 1.1: A typical production flow.

Product design provides a description of the product in low level simple geometric entities (faces, edges and vertices), while high level description of entities are desired to plan manufacturing processes in the manufacturing environments. Process planning builds a bridge between product design and manufacturing and translates design information into the process instructions to efficiently and effectively manufacture products. Tool planning for industrial robots for surface manufacturing, an example of a process planning, remains a challenging research topic [2, 3]. Since tool planning translates design information into the tool instructions to manufacture parts, it greatly affects the quality of the products and the efficiency of the surface manufacturing processes [4, 5]. Currently, there are two tool planning methods: manual and automated.

Manual tool planning (typical teaching methods) is based on manufacturing engineers' experience and knowledge of production facilities, equipment, their capabilities, processes, and tools. A manufacturing engineer has to carry out extensive tests on a work cell to improve a tool trajectory. This process is complex and very time-

consuming. The results vary based on the manufacturing engineers' skill. It usually requires the engineers to use a trial-and-error approach to find a good path or trajectory for a surface manufacturing tool. The generated path or trajectory is usually operator-dependent and error-prone. It is even harder for engineers to figure out a better path or trajectory when some performance criteria have to be considered. For example, in the Ford Motor Company's Aston Martin plant, it takes an experienced engineer a few weeks to design a trajectory for a car door panel.

Computer aided tool planning (CATP), an automated tool planning process (ATPP), is desirable for surface manufacturing. CATP, which automatically establishes communications between the CAD model of a part and the product manufacturing processes, reduces human labor dramatically and keeps human operators from being exposed to harmful working environments. Currently automated tool planning receives little attention and has always caused a bottleneck for surface manufacturing. Therefore it is essential to develop automated tool planning to replace manual tool planning. This challenging research topic has been receiving more and more attention from academia and industry.

1.2 Previous Work

According to the material distribution constraints, the processes in surface manufacturing can be categorized into two groups: material uniformity and coverage. Material uniformity requires that a surface be covered with material to achieve certain amount of material deposition. Examples are spray painting, spray forming and rapid tooling. Spray forming and rapid tooling can also be categorized as net shape manufacturing processes since no machining process is needed for the manufactured parts. Coverage requires that a surface be covered by material or touched by a tool, such as spray coating, spray cleaning [6] and polishing. There are only a few reports on automated tool planning for surface manufacturing.

1.2.

Spra

as au

robo

Figu
and

T

Too

and

tory

appr

simu

al. [

face

thic

repo

to d

depo

1.2.1 *Spray Painting*

Spray painting is an important process in the manufacturing of many products, such as automobiles, furniture and appliances. Figure 1.2 shows an industrial robot (ABB robot) used for spray painting.

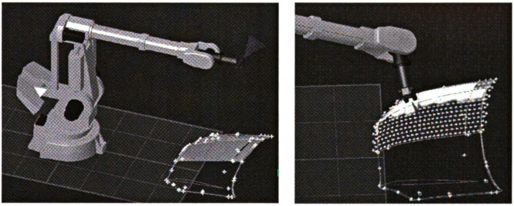

(a) (b)

Figure 1.2: The spray painting process using an industrial robot: (a) an ABB robot and a part; (b) the painting process for a portion of a car hood.

The uniformity of paint thickness on a product can strongly influence its quality. Tool planning for spray painting is critical to achieve uniformity of paint thickness and has been widely studied [7, 8, 9]. Suk *et al.* [9] developed an Automatic Trajectory Planning System(ATPS) for spray painting robots. Their method is based on approximating a free-form surface using a number of individual small planes. Their simulations showed over and under-painted areas on a painted surface. Asakawa *et al.* [7] developed a teachingless path generation method based on the parametric surface to paint a car bumper. The paint thickness was 13 to 28 μm while the average thickness was 17.7 μm. The method to find the spray width and gun velocity was not reported. Antonio *et al.* [10] developed a framework for optimal trajectory planning to deal with the paint thickness problem. However, the paint gun path and paint deposition rate must be specified. In practice, it is very difficult to obtain the paint deposition

as CimStat

trajectories

in an inter

is inefficien

1.2.2 Sp

Spray form

an industria

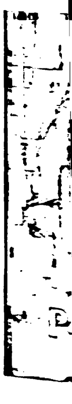

Figure 1.3:
a part; (b)

Glass fil

the preform

the choppe

spray-up is

thickness. A

air is drawn

melted, hot

deposition rate for a free-form surface. Alternatively, some commercial software, such as CimStation [11], IGRIP [12] and $ROBCAD^{TM}$/Paint [13], can generate paint gun trajectories and simulate the painting processes. However, the gun paths are obtained in an interactive way between the users and the software. This tool planning process is inefficient and error-prone.

1.2.2 Spray Forming

Spray forming is used for the glass fiber preforming processes [14]. Figure 1.3 shows an industrial robot (ABB robot) used for spray forming.

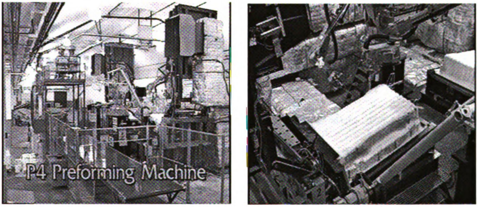

(a) (b)

Figure 1.3: The spray forming process using industrial robots: (a) ABB robots and a part; (b) the forming process for a pickup truck box.

Glass fiber is chopped and applied along with thermoplastic powdered binder to the preform screen using industrial robots. Positive airflow through the screen holds the chopped fiber on the screen surface during the entire spray-up routine. When spray-up is complete, the tool is closed and the preform is compressed to the desired thickness. Ambient temperature airflow through the screen is then stopped, and hot air is drawn through the screen in order to melt the binder. After the binder has been melted, hot airflow is stopped and ambient air is again drawn through the preform, freezing the binder and setting the preform. The tool is opened and the finished preform de-molded. The advantages of the technology are:

- light weight of parts because glass fiber is lighter compared to other materials, such as steel and cement;
- low cost because there are no dies as contrasted to the stamping methods;
- flexibility because robots can be re-programmed to manufacture other parts.

Chavka [14] developed a spray forming system. However, no path planning method was presented. Based on the CAD model of a building facade, Penin *et al.* [15] developed an automatic path planning method to spray glass fiber on a panel with cement. The fabricated panels can achieve better flex-traction strength and are lighter weight than conventional concrete panels. The spray width and tool velocity are determined using some spray rules. The paths are generated by approximating a curved surface with several planes. No material constraints are specified. The tool planning for spray forming must satisfy area density (material weight in a unit area) constraints [14].

1.2.3 Rapid Tooling

Rapid tooling is a type of rapid prototyping, which is a technology to quickly deliver a part by an additive, layer-by-layer process based on the CAD model of a mold. This is a new technology developed to reduce both time and cost. There are different technologies used for rapid prototyping [16], such as stereolithography (SLA), selective laser sintering (SLS), room temperature vulcanized (RTV) molding , and rapid tooling.

Rapid tooling is a process to produce components in a layer-by-layer (additive) process in end-use materials. The rapid tooling process has been attracting more attention lately because it can manufacture tools rapidly at low cost. There are two technologies for rapid tooling: direct and indirect. Direct rapid tooling directly makes hard tooling or metallic molds by depositing material on a surface layer-by-layer (also called layered manufacturing). Indirect rapid tooling makes hard tools or metallic molds using rapid prototyping parts as patterns. In indirect rapid tooling [17], molten metal is sprayed on a ceramic mold layer-by-layer until the desired metal thickness is achieved. Typically indirect rapid tooling is used to make dies or punches to produce parts. Since there is no machining process needed for the manufactured parts using the indirect rapid tooling process, it is a net shape manufacturing process. Figure 1.4 shows an industrial robot (ABB Robot) used for indirect rapid tooling process.

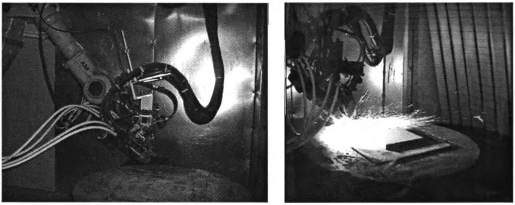

(a) (b)

Figure 1.4: The indirect rapid tooling process using an industrial robot: (a) an ABB robot and a part; (b) the indirect rapid tooling process.

Some work has been done on path planning for the direct rapid tooling process [4, 18, 19]. Luo *et al.* developed software and hardware for a rapid tooling system [18]. The software includes a slicing algorithm which generates 2D flat contours from a faceted 3D model and a tool path generation algorithm. Yang *et al.*[4] studied different scanning strategies for the tool path planning in rapid tooling. An equidistant scanning algorithm was proposed and implemented. Their methods improved manufacturing efficiency and product quality. However, both Luo and Yang's approaches only deal with 2D flat contours and are not sufficient to handle free-form surfaces.

There is little research work in the indirect rapid tooling process. Chalmers [17] demonstrated an indirect rapid tooling process used by the Ford Motor Company. No tool planning algorithm is reported. For indirect rapid tooling, the material sprayed on a mold must satisfy material thickness and temperature constraints. Because the path planning for direct rapid tooling can only deal with 2D contours, it is not suitable for the tool path planning of indirect rapid tooling since most parts are free-form surfaces.

1.2.4 Coverage

Coverage is to cover every point on a surface using a specific tool. Spray coating, spray cleaning, polishing are typical applications for coverage. There are different methods to generate paths for coverage. Sheng *et al.* [20] developed a method to automatically generate a path such that every point on a surface can be covered. Huang [21] presented an optimal path planning method to cover a surface by minimizing the turns. Polishing is necessary to obtain a good surface smoothness as well as to meet the required dimensional tolerances. Mizugaki [22] developed a path planning method for a polish robot. Takeuchi *et al.* [23] discussed polishing path generation using the CAD model of a surface. Even though these path planning methods can guarantee the coverage of a surface, the material distribution constraints are not considered.

1.2.5 Optimal Trajectory Planning

To increase productivity and the quality of manufactured products, it is desirable for industrial robots to run in their optimal conditions subject to given optimization criteria. In industry, minimal time of a manufacturing process means high productivity and low cost. To improve the product quality, the material distribution on a free-form surface has to be optimized. Hyotyniemi [24, 25] developed a locally controlled optimal trajectory planning system for spray painting robots. Paint thickness, surface quality and trajectory smoothness are considered to form a multi-objective optimization problem. However, the method is time-consuming and needs extremely high computing capacity even for simple surfaces. This makes the method infeasible. Moreover, the paint gun velocity is not considered as an optimization parameter. Antonio *et al.* [8, 10] presented an optimal trajectory planning method for spray coating. The variation of paint thickness is minimized. Because the optimization process needs high computing capacity, they developed fast solution techniques [26] to solve the problem. However, the spray gun path has to be given using teaching methods by experienced operators. The parametric representation of a surface and a path is needed for optimization. Although parametric representation is mathematically accurate, its local nature causes difficulties for path planning [20, 27]. Furthermore, these optimal tool planning methods are developed for individual process.

1.3 Motivations and Challenges

In manufacturing, computer aided tool planning (CATP) builds a communication between CAD and CAM [2]. Surface manufacturing, such as spray painting, spray forming, indirect rapid tooling, spray coating and polishing, need to generate trajectories based on the CAD model of a free-form surface such that the task constraints can be satisfied. Although some scattered and problem-specific planning algorithms have been developed, there is no general tool planning method for surface manufacturing. Optimal tool planning is hardly addressed. Also the verification of the generated trajectories is not discussed. Therefore, from a practical point of view, it is desirable to develop a general framework for automated optimal tool planning in surface manufacturing.

Due to different tool models and constraints in different processes, it is challenging to develop a general framework of tool planning for these processes. Since there is no feedback information available to control industrial robots in surface manufacturing, tool planning is crucial to the manufacture of high quality products. For material uniformity, material thickness must satisfy given constraints, but coverage does not have such a requirement. Some processes, such as indirect rapid tooling, need to spray a surface many times. These make the development of a general framework for automated tool planning in surface manufacturing difficult.

Optimal tool planning is even more challenging because:

- There are many optimization criteria: robot motion, optimal time, material distribution deviation and material waste.
- There are many adjustable parameters: the tool velocity, tool standoff, tool orientation and flow rate of material.

1.4 Objectives

Although the processes in surface manufacturing are different, they can be categorized into two groups: material uniformity and coverage. Material uniformity, such as spray painting, spray forming and indirect rapid tooling, requires the material distribution on a surface to satisfy given constraints. Coverage, such as spray coating, spray cleaning and polishing, requires that every point on a surface be covered. However, both material uniformity and coverage have some commonalities: (a) the trajectories are generated based on the CAD models, tool models, constraints and optimization criteria, and (b) the tool trajectory is defined by a six dimensional vector which specifies the position and orientation of a tool. Therefore, the objective of this dissertation is to develop a general framework for automated CAD-guided optimal tool planning in surface manufacturing.

1.5 Contributions of the Dissertation

In this dissertation, a general framework for automated CAD-guided optimal tool planning in surface manufacturing has been developed and implemented successfully. The main contributions of the dissertation are:

- A general framework for automated CAD-guided optimal tool planning in surface manufacturing has been developed based on the CAD-model of a free-form surface, a tool model, constraints and optimization criteria.
- A patch forming algorithm has been developed to satisfy the given constraints.
- Comparison of different material deposition patterns has been performed. The performance of the raster material deposition pattern is better than that of the spiral material deposition pattern for continuous material deposition processes.
- A theorem has been proven about the relationship between the material distribution and tool velocity.
- A tool trajectory generation algorithm has been developed such that the given material thickness constraints can be satisfied. The tool path of a free-form surface is generated using an improved bounding box method. The tool orientation is determined based on the local geometry of a free-form surface.
- A tool trajectory integration algorithm has been developed to integrate the tool trajectories for a surface with multiple patches.
- A tool trajectory verification model has been formulated to verify the generated trajectories.
- An optimal tool planning algorithm has been developed to generate tool trajectories based on the given optimization criteria.

- An optimal tool planning algorithm for non-uniform material distribution on a free-form surface has been developed and implemented.

- The general framework has been extended to other applications, such as the dimensional inspection in manufacturing and nanoassembly in nanomanufacturing.

1.6 Organization of the Dissertation

This dissertation describes a general framework for automated CAD-guided optimal tool planning in surface manufacturing. The tool planning algorithm is developed for various applications. Implementations and simulations are presented to test the general framework and verify the generated trajectories. The dissertation includes the following chapters:

- Chapter 2 describes a general framework for automated CAD-guided optimal tool planning of free-form surfaces in surface manufacturing. The CAD model of a free-form surface, a tool model, task constraints, and optimization criteria are presented.

- Chapter 3 introduces a general framework for an automated CAD-guided tool planning algorithm. The determination of tool trajectory parameters is discussed. The comparison of different material deposition patterns is reported. The patch forming algorithm is presented. The trajectory generation algorithm is developed for a patch. The tool trajectory verification model is presented to compute the material distribution on a free-form surface. A suboptimal velocity algorithm is developed.

- Chapter 4 reports a tool trajectory integration algorithm for a free-form surface with multiple patches. Three cases: parallel-parallel (PA-PA), parallel-perpendicular (PA-PE) and perpendicular-perpendicular (PE-PE), are discussed for a surface with two patches. A trajectory integration algorithm for a surface with multiple patches is also presented.

- Chapter 5 presents the implementation and testing of the automated tool planning algorithm. Tool trajectories for different parts in different processes are generated and verified. The verification of the trajectory integration algorithm is also performed.

- Chapter 6 discusses the general framework for automated CAD-guided optimal tool planning. An optimal tool planning algorithm for constant material distribution is developed and implemented. A preference articulation method is discussed. Implementation of four cases, optimal time, optimal material distribution, no preference articulation and preference articulation, are presented.

- Chapter 7 presents the general framework for automated CAD-guided optimal tool planning with non-uniform material distribution. The developed algorithm is implemented. Implementation of four cases, optimal time, optimal material distribution, no preference articulation and preference articulation, are presented.

- Chapter 8 discusses the extensions of the general framework to other processes, such as dimensional inspection in manufacturing and nanoassembly in nanomanufacturing.

- Chapter 9 summarizes the dissertation by giving conclusions and presenting the extensions of the developed general framework.

CHAPTER 2

A GENERAL FRAMEWORK OF OPTIMAL TOOL PLANNING

In this chapter, a general framework for automated CAD-guided optimal tool planning in surface manufacturing is presented. The CAD model of a free-form surface, a tool model, task constraints and optimization criteria are discussed.

2.1 A General Framework

A general framework for automated CAD-guided optimal tool planning is to generate an optimal tool trajectory based on the CAD model of a free-form surface, a tool model, constraints and optimization criteria. Tool planning, also called trajectory generation, is to plan the tool position, orientation, and velocity for a given process in surface manufacturing. A general framework for automated CAD-guided optimal tool planning in surface manufacturing can be formulated as:

Given the CAD model of a free-form surface M, a tool model G, constraints Ω and optimization criteria Ψ, find a tool trajectory Γ such that the constraints are satisfied, i.e.,

$$F(M, \Omega, G, \Psi) = \Gamma. \tag{2.1}$$

Figure 2.1 illustrates the automated CAD-guided optimal tool planning system. Based on the CAD model of a free-form surface, a tool model, constraints and optimization criteria, the optimal tool trajectory planner generates an optimal tool trajectory automatically for a free-form surface. The optimal tool trajectory is input to a tool trajectory verification model to verify if it satisfies the given constraints. The trajectory is also input to $ROBCAD^{TM}$/Paint [13] to simulate the kinematics constraints and collisions.

Fig

The o

2.2 shows

Based

tool mode

planning a

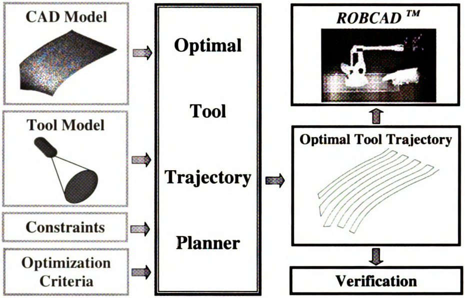

Figure 2.1: The automated CAD-guided optimal tool planning system.

The optimal tool trajectory planner is the core of the general framework. Figure 2.2 shows how the planner works.

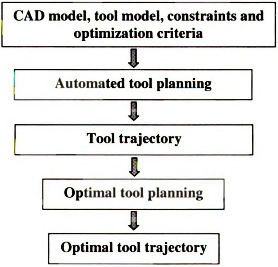

Figure 2.2: The optimal tool trajectory planner.

Based on the given conditions, such as the CAD model of a free-form surface, tool model and constraints, a tool trajectory is generated using the automated tool planning algorithm. Then the optimal tool planning algorithm is applied to generate an optimal tool trajectory for the free-form surface based on the optimization criteria.

2.2 Task Conditions and Requirements

This section describes the CAD model of a free-form surface, a tool model, task constraints and optimization criteria.

2.2.1 CAD Model

The CAD model of a free-form surface contains geometric information of the surface. According to Sheng [28], the representation scheme in 3D modeling can be categorized into parametric and tessellation representations. The parametric representation is popular in CAD modeling. B-Spline, Bezier and NURBS surfaces are some of the common parametric surfaces used in CAD modeling [29, 30]. The parametric representation is mathematically accurate, however, its local nature brings difficulties for tool planning [27]. The global knowledge of a free-form surface, instead of the local knowledge, is important for tool planning [28]. Tessellation representation, which is much simpler, is frequently used to approximate free-form surfaces. With increased computer processing power, tessellation representation can be very refined and accurate. A triangular approximation of a free-form surface, which has global information about a free-form surface, is desirable for tool trajectory planning. The error introduced in rendering a free-form surface into triangles can be decreased by reducing the size of triangles. Therefore, after tessellation, the CAD model of a free-form surface M can be formulated as:

$$M = \{T_i : i = 1, \cdots, N\} \tag{2.2}$$

where T_i is the ith triangle on the free-form surface; N the number of triangles. Figure 2.3 shows the triangular approximation of a free-form surface.

In CAD design, a free-form surface consists of many low curvature parametric

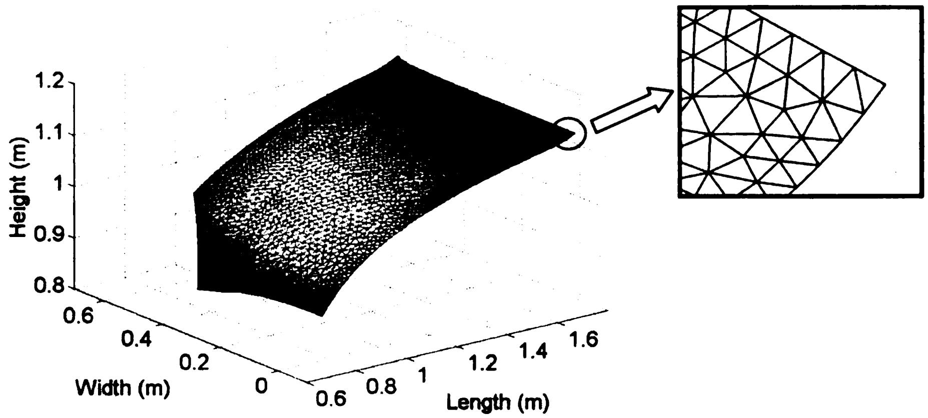

Figure 2.3: The triangular approximation of part of a car hood.

surfaces. The normals of these parametric surfaces may not point to one side of the free-form surface. Therefore, after a free-form surface is rendered into triangles, the normals of the triangles have to be adjusted. Here a method is developed to adjust normals of the triangles.

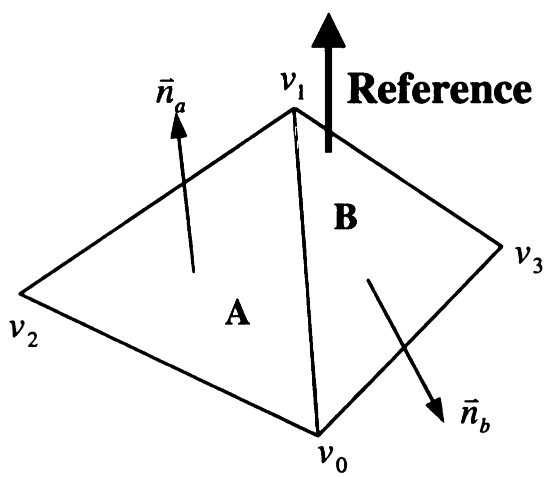

Figure 2.4: The normals of triangles. v_0, v_1, v_2 and v_3 are the vertices of triangles A and B.

Figure 2.4 shows two neighbor triangles A and B. $\overrightarrow{n_a}$ and $\overrightarrow{n_b}$ are normals of triangles A and B. In the data structure, a triangle is represented by its three vertices. Each vertex contains the XYZ coordinates. The normal of the triangle is determined by the sequence of its three vertices. If the sequence of any two vertices in a triangle is reversed, the normal of the triangle is reversed. Suppose triangle A points to the same side as a reference direction, which can be determined by the angle between the normal of triangle A and the normal of the reference. Then triangle A is chosen as the seed triangle. The normal of triangle A is generated using its three vertices v_0, v_1 and v_2. The sequence is:

$$v_0 \longrightarrow v_1 \longrightarrow v_2 \longrightarrow v_0.$$

Triangle B, which has a common edge with triangle A (two common vertices), is found. If the normals of triangles A and B point to one side, the sequences of the two common vertices in the two triangles must be reversed. For example, if the the sequence of v_0 and v_1 in triangle B is

$$v_1 \longrightarrow v_0 \longrightarrow v_3 \longrightarrow v_1,$$

the normals of triangles A and B point to the same side since the sequences of v_0 and v_1 are reversed in the two triangles. There is no need to reverse the sequence of the two vertices. If the sequence of triangle B is:

$$v_1 \longrightarrow v_3 \longrightarrow v_0 \longrightarrow v_1,$$

This sequence of v_0 and v_1 in triangle B is the same as that in triangle A. The sequence of v_0 and v_1 has to be changed to reverse the normal of triangle B. This process continues until all of the triangles with common edges are processed. Then the newly added triangles are used as seed triangles and the process continues until there is no triangle left. Then the normals of the triangles are adjusted.

2.2.2 *Tool Model*

A tool model can be modeled as a spray cone [8, 9, 31, 32, 33] as shown in Figure 2.5.

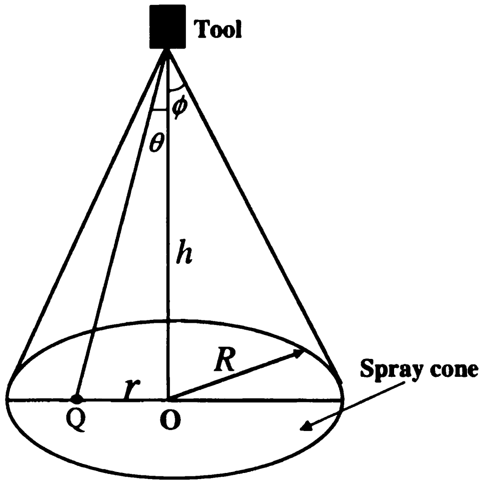

Figure 2.5: A tool model. ϕ is the fan angle; θ the spray angle; h the tool standoff; R the spray radius; r the actual spray distance.

Material particles are emitted from the tool radially within the spray cone with a fan angle ϕ. A spray pattern is formed when the spray cone intersects a plane. The distance from the tool center to the plane is the tool standoff h. The normal of the plane is parallel to the tool spray direction. The radius of the spray pattern is R, which is defined as spray radius. θ is the spray angle and r the actual spray distance.

For material uniformity, the knowledge of the material deposition rate on a spray pattern is needed. The material deposition rate depends on many parameters, such as the tool standoff and the flow rate of material. Here these parameters are assumed to be fixed [9, 10, 31, 32]. There are different profiles of the material deposition rate [8, 9, 31, 32, 33] used in different processes. Some profiles are quite simple [9] and others are quite complex [33]. A typical profile of the material deposition rate can be roughly approximated by parabolic curves [8, 32] as shown in Figure 2.6.

The material deposition rate on a plane can be modeled as:

$$G = f(r, h). \tag{2.3}$$

Goodman it et al. [34] presented a method to measure the material deposition rate

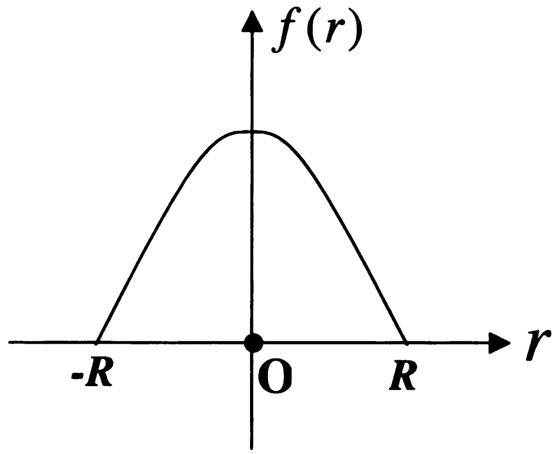

Figure 2.6: A tool profile.

by spraying a plane. The tool model is valid for coverage if the material deposition rate is considered to be a constant. For some processes, such as polishing, the tool model is still valid even though the tool standoff is 0.

2.2.3 Task Constraints

A general constraint Ω can be expressed as follows:

$$\Omega = \{q_d(x, y, z(x, y)), \Delta q_d(x, y, z(x, y)), \omega\} \tag{2.4}$$

where $x, y, z(x, y)$ are the coordinates of a point on a free-form surface; $q_d(x, y, z(x, y))$ is the desired material thickness constraint on the point ; $\Delta q_d(x, y, z(x, y))$ the material thickness deviation from the desired material thickness on the point; ω other constraints, such as material waste, cycle time, reachability, temperature and tool orientation. For example, the temperature on a surface must be kept in a certain range during a rapid tooling process. For some applications, the tool orientation cannot change rapidly.

Spray painting, spray forming and indirect rapid tooling require that the tool trajectory planning satisfy material uniformity constraints, i.e., the material sprayed on a free-form surface must satisfy the desired material thickness and material thickness deviation constraints. Spray cleaning and polishing are examples of coverage. Each point on a free-form surface must be covered by a spray pattern. Coverage is a special case of material uniformity. Therefore the constraints can be expressed using a general formula, i.e.,

$$\begin{array}{ll} \Delta q_d(x, y, z(x, y)) \neq 0 & \text{Material uniformity} \\ q_d(x, y, z(x, y)) = 1, \Delta q_d(x, y, z(x, y)) = 0 & \text{Coverage} \end{array} \tag{2.5}$$

2.2.4 Optimization Criteria

Optimal tool planning is based on the optimization criteria. A general optimization criterion Ψ is expressed as:

$$\Psi = (\Psi_1, \Psi_2, ..., \Psi_K) \tag{2.6}$$

where $\Psi_1, \Psi_2, ..., \Psi_K$ are K optimization criteria, such as minimum time and optimal material distribution etc..

CHAPTER 3

AUTOMATED TOOL PLANNING

This chapter discusses an automated tool planning system. Based on the CAD model of a free-form surface and a tool model, an automated tool planning system is developed such that the given constraints are satisfied. A patch forming algorithm is presented to generate patches. After patches are formed, a trajectory is generated for each patch. A trajectory verification model is developed to verify the generated trajectory. A suboptimal tool velocity algorithm is discussed to minimize the material thickness deviation.

3.1 A General Framework for Automated Tool Planning

An automated tool planning system is to generate a tool trajectory automatically based on the CAD model of a free-form surface, a tool model and constraints in surface manufacturing. The automated CAD-guided tool planning system can be formulated as follows:

Given the CAD model of a free-form surface M, a tool model G and constraints Ω, find a tool trajectory Γ such that the constraints are satisfied, i.e.,

$$F(M, \Omega, G) = \Gamma. \tag{3.1}$$

Figure 3.1 illustrates the automated tool planning system. Based on the CAD model of a free-form surface, a tool model and constraints, the automated tool trajectory planner generates a tool trajectory automatically. Here the desired material thickness is considered to be a constant. The generated trajectory is input to a trajectory verification model to verify if it satisfies the given constraints. The trajectory is also input to $ROBCAD^{TM}$/Paint [13] to simulate the kinematics constraints and collisions.

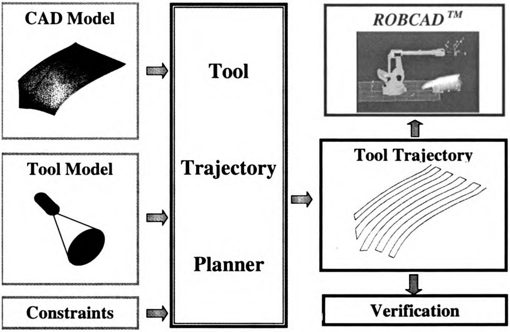

Figure 3.1: The automated tool planning system.

The tool trajectory planner is the core of the automated tool planning system. Figure 3.2 shows how the tool trajectory planner works.

From the given conditions, such as the CAD model of a free-form surface, a tool model and constraints, patches are formed for the free-form surface using the patch forming algorithm. Then, a trajectory is generated for each patch using the tool trajectory planning algorithm. The generated trajectories of the patches are integrated to form a trajectory for the free-form surface. The suboptimal tool velocity algorithm is developed to optimize the material distribution deviation. Finally, the generated trajectory is verified to check if the given constraints are satisfied. This chapter focuses on the tool trajectory generation for one patch. The tool trajectory integration is discussed in the next chapter.

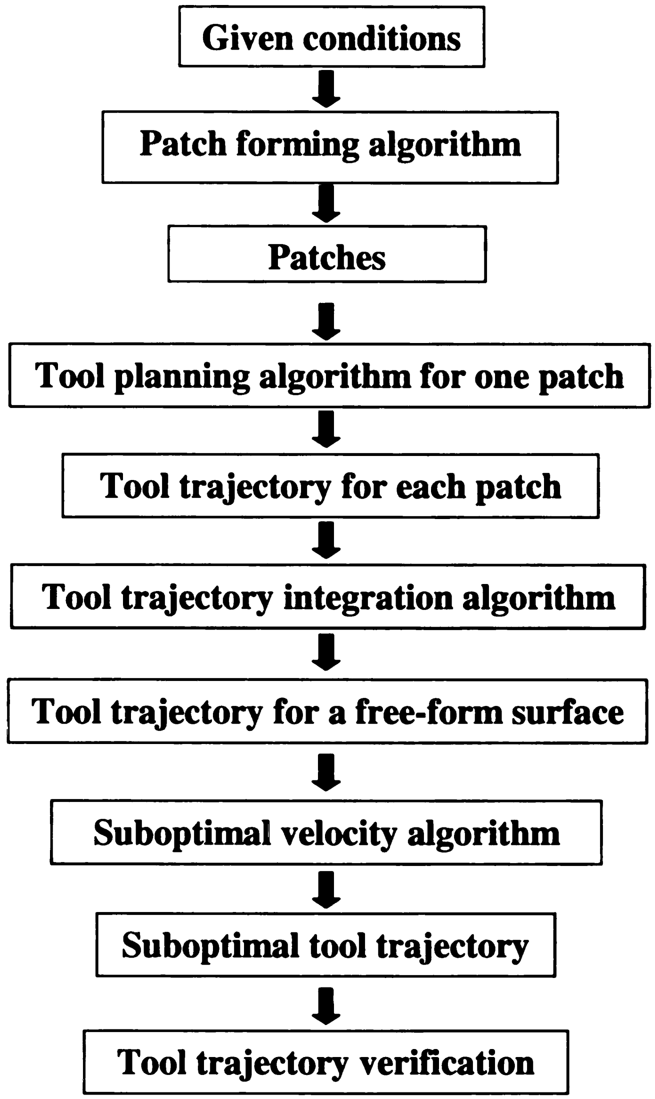

Figure 3.2: The automated tool trajectory planner.

3.2 Determination of Tool Trajectory Parameters

To generate a tool trajectory for a free-form surface, the spray width and the tool velocity have to be determined. The spray width and the tool velocity are computed by optimizing the spraying process on a plane. Figure 3.3 shows material deposition on a plane.

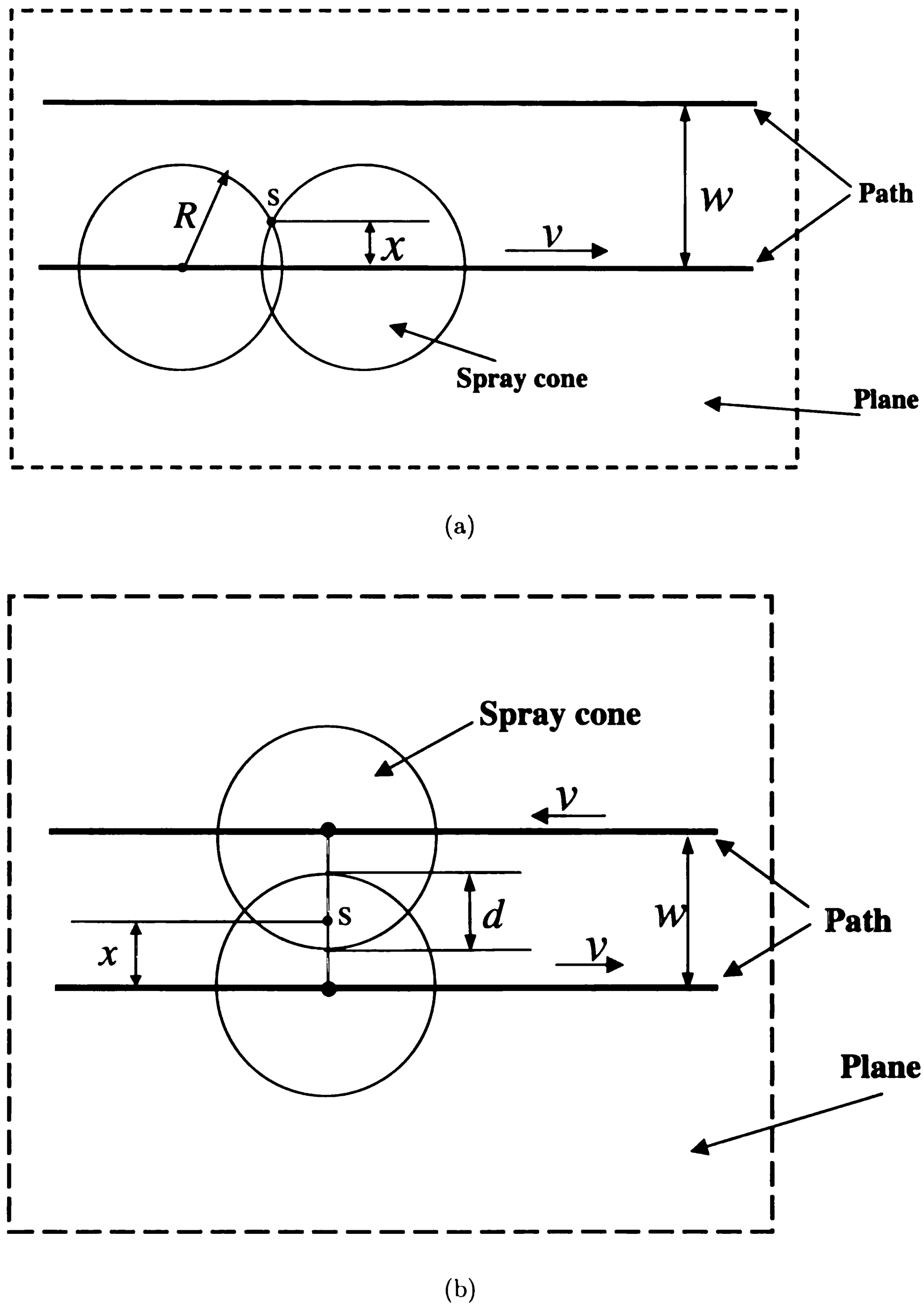

Figure 3.3: Material deposition of a point s on a plane: (a) one path (b) two paths. R is the spray radius; x the distance of the point s to the first path; v the tool velocity; and d the overlapping distance.

The spray width w can be expressed as:

$$w = 2R - d \tag{3.2}$$

where d is the overlapping distance.

Theorem 3.2.1 *Given a tool model, the material thickness on a plane is related to the tool velocity and the overlapping distance. Moreover, the material thickness is inversely proportional to the tool velocity.*

Proof. The material thickness of a point s on a plane can be calculated using the following equation,

$$q_s = \int_0^T f(r(t))dt \tag{3.3}$$

where $q(s)$ is the material thickness of point s; T the total spray time for point s; and $r(t)$ the distance from point s to the center of the spray cone.

For each point on the plane, there are at most two neighboring paths which contribute to the material thickness of the point. The material thickness $\bar{q}(x,d,v)$ of the point due to the two paths can be expressed as:

$$\bar{q}(x,d,v) = \begin{cases} \bar{q}_1(x,v) & 0 \le x \le R-d \\ \bar{q}_1(x,v) + \bar{q}_2(x,d,v) & R-d < x \le R \\ \bar{q}_2(x,d,v) & R < x \le 2R-d \end{cases} \tag{3.4}$$

where x is the distance of the point to the first path; v the tool velocity; $\bar{q}_1(x,v)$ and $\bar{q}_2(x,d,v)$ are the material thickness due to the first and second paths respectively. They can be calculated using equation (3.3),

$$\begin{aligned} \bar{q}_1(x,v) &= 2\int_0^{t_1} f(r_1)dt \qquad 0 \le x \le R \\ \bar{q}_2(x,d,v) &= 2\int_0^{t_2} f(r_2)dt \qquad R-d \le x \le 2R-d \end{aligned} \tag{3.5}$$

where t_1 and t_2 are the parameters related to the spray time on point s for the first and second paths respectively; r_1 and r_2 the distances of the point to the tool centers respectively. t_1, t_2, r_1 and r_2 are:

$$
\begin{aligned}
t_1 &= \frac{\sqrt{R^2 - x^2}}{v}, \qquad & t_2 &= \frac{\sqrt{R^2 - (2R - d - x)^2}}{v} \\
r_1 &= \sqrt{(vt)^2 + x^2}, \qquad & r_2 &= \sqrt{(vt)^2 + (2R - d - x)^2}.
\end{aligned} \tag{3.6}
$$

In equation (3.5), let

$$t = \frac{y}{v}, \tag{3.7}$$

then it can be written as:

$$
\begin{aligned}
\bar{q}_1(x, v) &= \frac{2}{v} \int_0^{t_1'} f(r_1')dy \qquad & 0 \leq x \leq R \\
\bar{q}_2(x, d, v) &= \frac{2}{v} \int_0^{t_2'} f(r_2')dy \qquad & R - d \leq x \leq 2R - d
\end{aligned} \tag{3.8}
$$

where

$$
\begin{aligned}
t_1' &= \sqrt{R^2 - x^2}, \qquad & t_2' &= \sqrt{R^2 - (2R - d - x)^2} \\
r_1' &= \sqrt{y^2 + x^2}, \qquad & r_2' &= \sqrt{y^2 + (2R - d - x)^2}.
\end{aligned} \tag{3.9}
$$

Therefore, $\bar{q}_1(x, v)$ and $\bar{q}_2(x, d, v)$ are inversely proportional to the tool velocity. From equations (3.4) and (3.8), we obtain that the material thickness on a plane is inversely proportional to the tool velocity and also related to the overlapping distance. $\triangleleft$

To find an optimal velocity v and an overlapping distance d, the mean square error of the material thickness deviation from the required material thickness q_d must be minimized, i.e.,

$$\min_{d \in [0, R], v} \left\{ E_1(d, v) = \int_0^{2R-d} (q_d - \bar{q}(x, d, v))^2 dx \right\}. \tag{3.10}$$

The maximum and minimal material thickness deviations from the average material thickness have to be minimized because they determine the material thickness deviation from the average material thickness.

$$\min_{d\in[0,R],v} \left\{E_2(d,v) = (\bar{q}_{max} - q_d)^2 + (q_d - \bar{q}_{min})^2\right\}. \tag{3.11}$$

From equations (3.10) and (3.11), a multi-objective error function is formulated:

$$E(d,v) = (E_1(d,v), E_2(d,v))^T. \tag{3.12}$$

The no preference articulation method in Appendix A is adopted to solve the multi-objective optimization problem. From equation (A.4), equation (3.12) can be transferred to,

$$\min_{d\in[0,R],v} \left\{E(d,v) = \lambda_1 E_1(d,v) + \lambda_2 E_2(d,v)\right\}. \tag{3.13}$$

Lemma 3.2.1 *$E(d,v)$ can be minimized by properly choosing the overlapping distance d.*

Proof. From Theorem (3.2.1), $\bar{q}(x,d,v)$ is inversely proportional to the tool velocity v. Let:

$$\bar{q}(x,d,v) = \frac{1}{v}\rho(x,d). \tag{3.14}$$

Then the maximum and the minimum material thicknesses can be expressed as:

$$\bar{q}_{max} = \frac{1}{v}\rho_{max}(d), \qquad \bar{q}_{min} = \frac{1}{v}\rho_{min}(d). \tag{3.15}$$

To find minimal $E(d,v)$, first compute

$$\frac{\partial E(d,v)}{\partial v} = 0. \tag{3.16}$$

From equations (3.12), (3.14), (3.15) and (3.16), the following equation is obtained:

$$v = \frac{\lambda_1 \int_0^{2R-d} \rho^2(x,d)dx + \lambda_2 \rho_{max}^2(d) + \lambda_2 \rho_{min}^2(d)}{q_d[\lambda_1 \int_0^{2R-d} \rho(x,d)dx + \lambda_2 \rho_{max}(d) + \lambda_2 \rho_{min}(d)]}. \tag{3.17}$$

The tool velocity can be expressed as a function of the overlapping distance d. Therefore, the minimization of $E(d, v)$ is only related to the overlapping distance d. $\triangleleft$

A golden section method [35] is adopted here to calculate the overlapping distance d and the tool velocity v by iteration.

3.3 Comparison of Material Deposition Patterns

Material deposition on a free-form surface in manufacturing has many applications, such as surface manufacturing and rapid prototyping (3D printing and layered manufacturing) [4, 19, 36]. These applications can be categorized into two groups, continuous and discontinuous material deposition. The continuous material deposition is to deposit material on a free-form surface continuously, such as surface manufacturing. For the discontinuous material deposition, the tools can be turned on and off to deposit material on a surface. Tool path planning for these two processes has been widely studied and different material deposition patterns have been used. There are two main material deposition patterns, raster and spiral, as shown in Figures 3.4(a) and 3.4(b) respectively.

Both the raster and the spiral patterns are implemented in continuous and discontinuous material deposition [7, 9, 18, 19, 36, 37]. Kao *et al.* [36] claims that the spiral material deposition pattern is preferred for layered manufacturing. However, they do not report any explanation. Although the two patterns are used in different applications, there is no comparison to show the performance of the two patterns. Therefore, to achieve better material distribution, it is desirable to compare the performance of the two patterns in different applications. Here the comparison of the

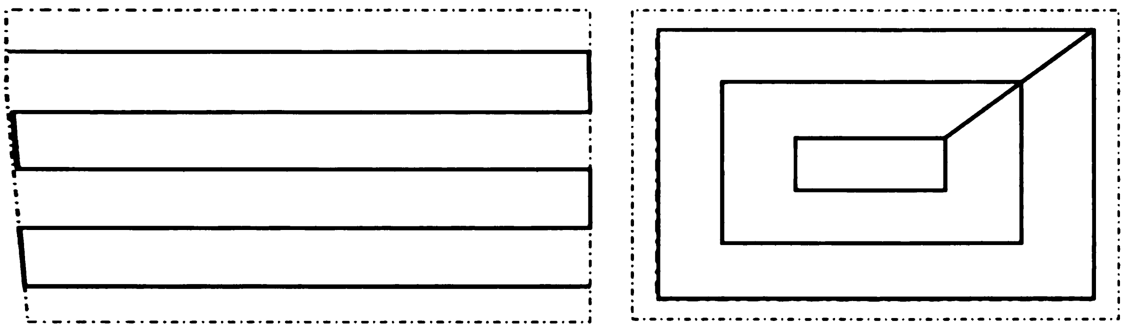

(a) (b)

Figure 3.4: The material deposition patterns: (a) raster; (b) spiral.

two material deposition patterns for continuous material deposition is performed.

The uniformity of material distribution on a product can strongly influence the quality of the product. Hence, the uniformity of the material distribution is used as a criterion to justify the two material deposition patterns. Since optimal tool planning may affect the uniformity of the material distribution, the optimal tool planning algorithm (Chapter 6) is used to generate optimal tool trajectories to obtain optimal material distribution for the two material deposition patterns. Based on the CAD model of a surface and a tool model, two trajectories are generated for the two material deposition patterns. The trajectories are then optimized to obtain the optimal material distribution to justify the two material deposition patterns.

A plane, which was rendered into triangles as shown in Figure 3.5, is used to test the two material deposition patterns. If the material distribution of a material deposition pattern on a plane is better than that of the other, the same result can be obtained on a free-form surface.

The parameters used to compute the material distribution are the same as those in Section 5.1.1. Using the spray width in equation (5.2), the trajectories for the two material deposition patterns are generated and shown in Figures 3.6(a) and 3.6(b) respectively.

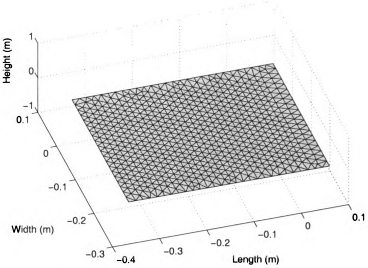

Figure 3.5: The triangular approximation of a plane.

The material thicknesses for the two paths are calculated based on the constant velocity in equation (5.2) using the trajectory verification model (3.34). The results are shown in Figures 3.7(a) and 3.7(b) respectively. The big jump in Figures 3.7(a) and 3.7(b) is due to the transition of the path as shown in Figures 3.6(a) and 3.6(b).

Then the paths are divided into segments and each segment is divided into 10 small pieces. The optimal tool planning algorithm (Chapter 6) is applied to optimize the velocities to obtain optimal material distribution. The material thicknesses for the two material deposition patterns are computed and shown in Figures 3.8(a) and 3.8(b) respectively.

For the raster material deposition pattern, the maximum and minimum material thicknesses occur at the boundary of the part (Figures 3.7(a) and 3.8(a)) for both optimal and non-optimal trajectories. This can be compensated by extending the path outside the part (Section 3.5) or by the neighboring path (Chapter 4) . Therefore, better results can be achieved for the raster pattern (Section 5.1.2). However, the maximum and the minimum material thicknesses for the spiral pattern occur at the corners of the paths (middle of a part), which cannot be compensated.

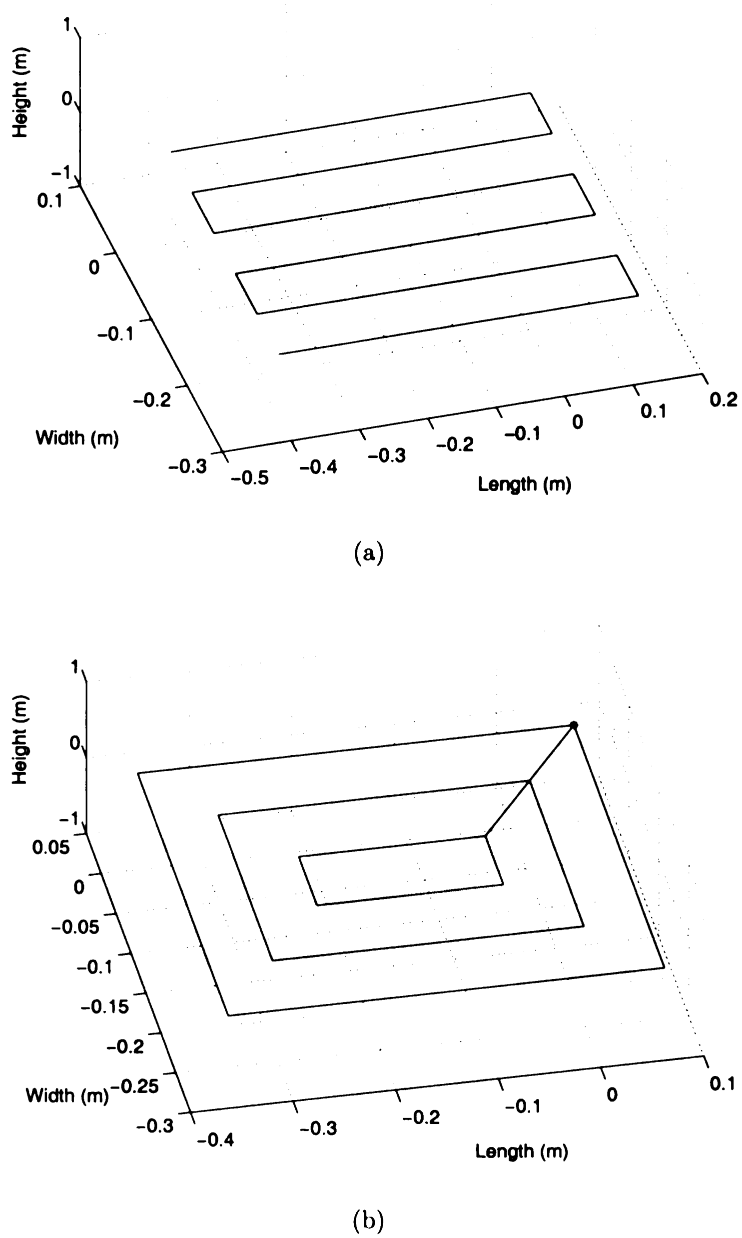

Figure 3.6: The generated paths for the two material deposition patterns: (a) raster; (b) spiral.

The results of the material distribution for the two material deposition patterns are summarized in Table 3.1.

The maximum material thickness for the spiral pattern is larger than that of

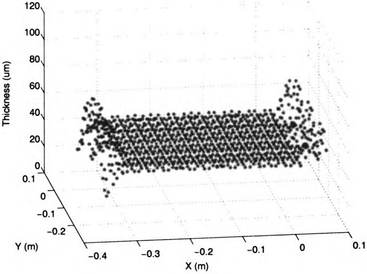

(a)

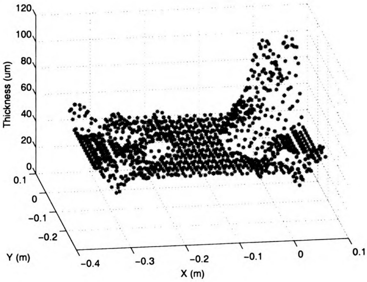

(b)

Figure 3.7: The material thicknesses for the two material deposition patterns with constant velocity: (a) raster; (b) spiral.

the raster pattern. The minimum material thickness is smaller. This means the deviation of the material distribution of the spiral pattern is bigger than that of the raster pattern. The path length of the spiral pattern is also longer than that of the

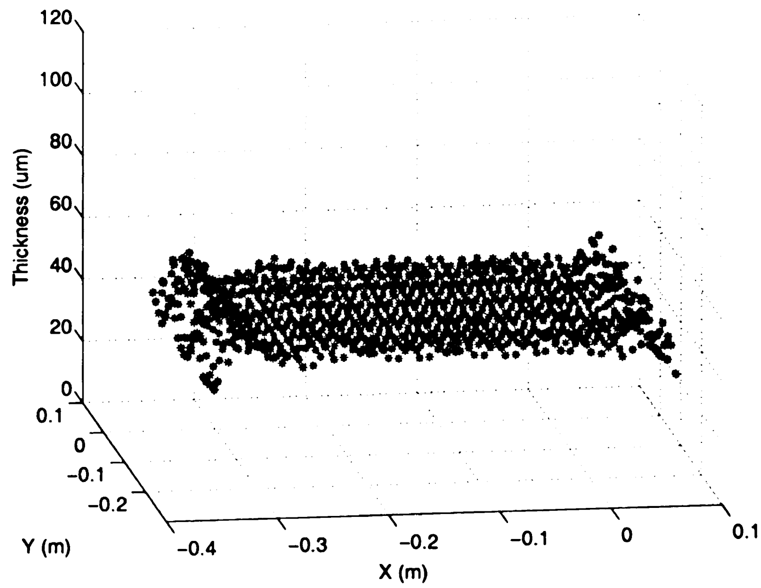

(a)

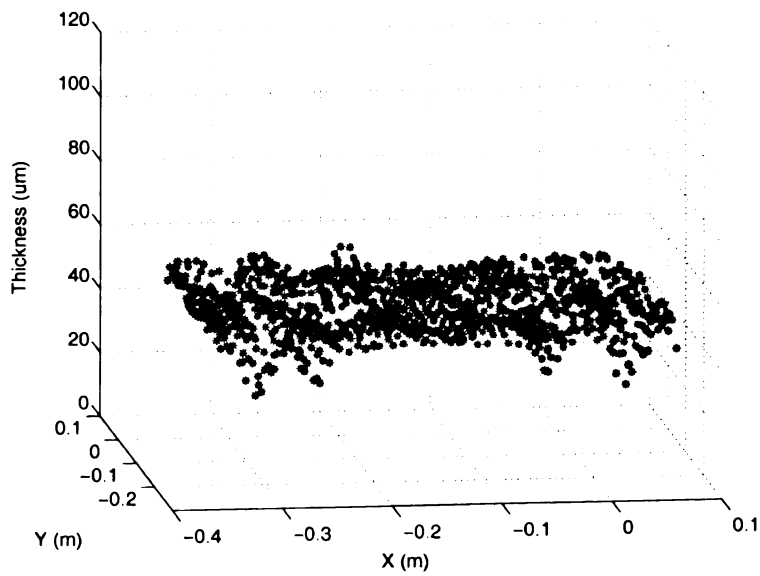

(b)

Figure 3.8: The optimal material thicknesses for the two material deposition patterns: (a) raster; (b) spiral.

raster pattern. So is the process time. Therefore, it is better to use the raster pattern in continuous material deposition processes. This is consistent with the fact that the

Table 3.1: The implementation results for the two material deposition patterns

—	Optimal		Non-optimal	
—	Raster	Spiral	Raster	Spiral
Average (μm)	49.9	49.6	51.3	54.1
Maximum (μm)	61.6	68.8	77.1	116.5
Minimum (μm)	37.8	29.5	27.5	30.9
Process time (s)	8.39	8.77	8.84	9.56
Path length (m)	2.8566	3.0894	2.8566	3.0894

raster pattern is widely used in automotive manufacturing.

3.4 Patch Forming Algorithm

The process for patch forming is shown in Figure 3.9.

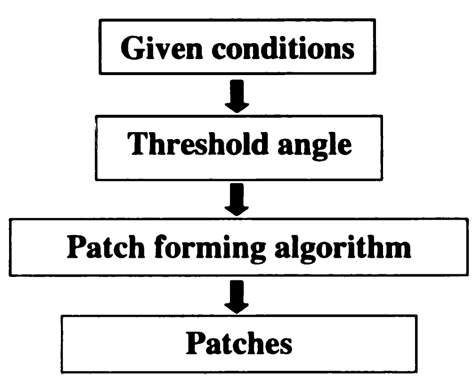

Figure 3.9: Patch forming algorithm.

Based on a tool model and constraints, the maximum and minimum material thicknesses on a plane are calculated. A threshold angle is obtained. Patches are formed using the patch forming algorithm.

3.4.1 Threshold Angle Determination

After the material thickness on a plane is optimized, the average, maximum and minimum material thicknesses are q_d, $\bar{q}_{max}$ and $\bar{q}_{min}$ respectively. Assume that the total material on the plane is projected to a free-form surface and the maximum deviation angle of the free-form surface is β_{th}. The maximum deviation angle is the maximum angle between the normal of every point on the free-form surface and the normal of the plane. Figure 3.10 shows the material on a plane projected to a free-form surface.

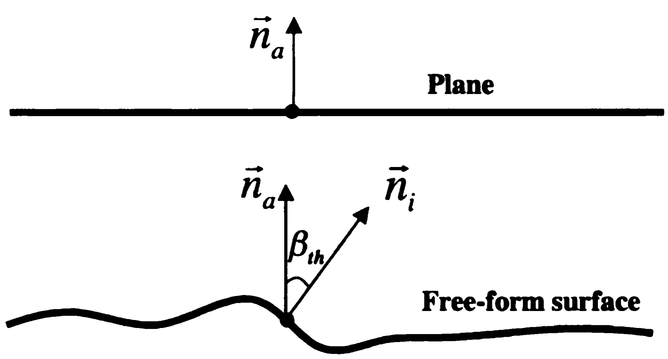

Figure 3.10: The material on a plane is projected to a free-form surface. β_{th} is the maximum deviation angle of the free-form surface; $\vec{n}_a$ the normal of the plane; and $\vec{n}_i$ the normal of a point s on the free-form surface.

Assume the total material is projected to the free-form surface along the normal of the plane. Without considering the tool standoff variation, the material thickness at point s can be expressed as:

$$q_s = \bar{q}cos(\beta_{th}) \tag{3.18}$$

where $\bar{q}$ is the material thickness on the plane. The material thickness q_s on the free-from surface must satisfy the following inequality:

$$\bar{q}_{min}cos(\beta_{th}) \leq q_s \leq \bar{q}_{max}. \tag{3.19}$$

If the material thickness q_s on the free-form surface satisfies the task constraints, i.e.,

$$|q_s - q_d| \leq \Delta q_d, \tag{3.20}$$

then

$$\bar{q}_{max} - q_d \leq \Delta q_d \tag{3.21}$$

$$q_d - \bar{q}_{min} cos(\beta_{th}) \leq \Delta q_d. \tag{3.22}$$

If equation (3.21) is always satisfied, the threshold angle β_{th} can be calculated using equation (3.22),

$$\beta_{th} = acos\frac{q_d - \Delta q_d}{\bar{q}_{min}}. \tag{3.23}$$

This means, for any free-form surface, if the maximum deviation angle β_{max} satisfies:

$$\beta_{max} \leq \beta_{th}, \tag{3.24}$$

the material thickness on the free-form surface can satisfy the material thickness constraints.

In coverage, the threshold angle β_{th} can be chosen as any value less than 90^o according to equation (3.34).

3.4.2 Patch Generation

After the threshold angle β_{th} is obtained, patches are generated. A patch is expressed as:

$$PT_i = \{T_j | cos^{-1}(\vec{n}_j \bullet \vec{n}_k) < \beta_{th}, D(T_j, T_k) \leq R, T_j \in M, T_k \in M\} \tag{3.25}$$

where PT_i is the ith patch; $\vec{n}_j$ and $\vec{n}_k$ are the normals of the jth and kth triangles, respectively; $D(T_j, T_k)$ is the distance between the centers of the jth and kth triangles. The patch generation process of a patch is shown in Figure 3.11.

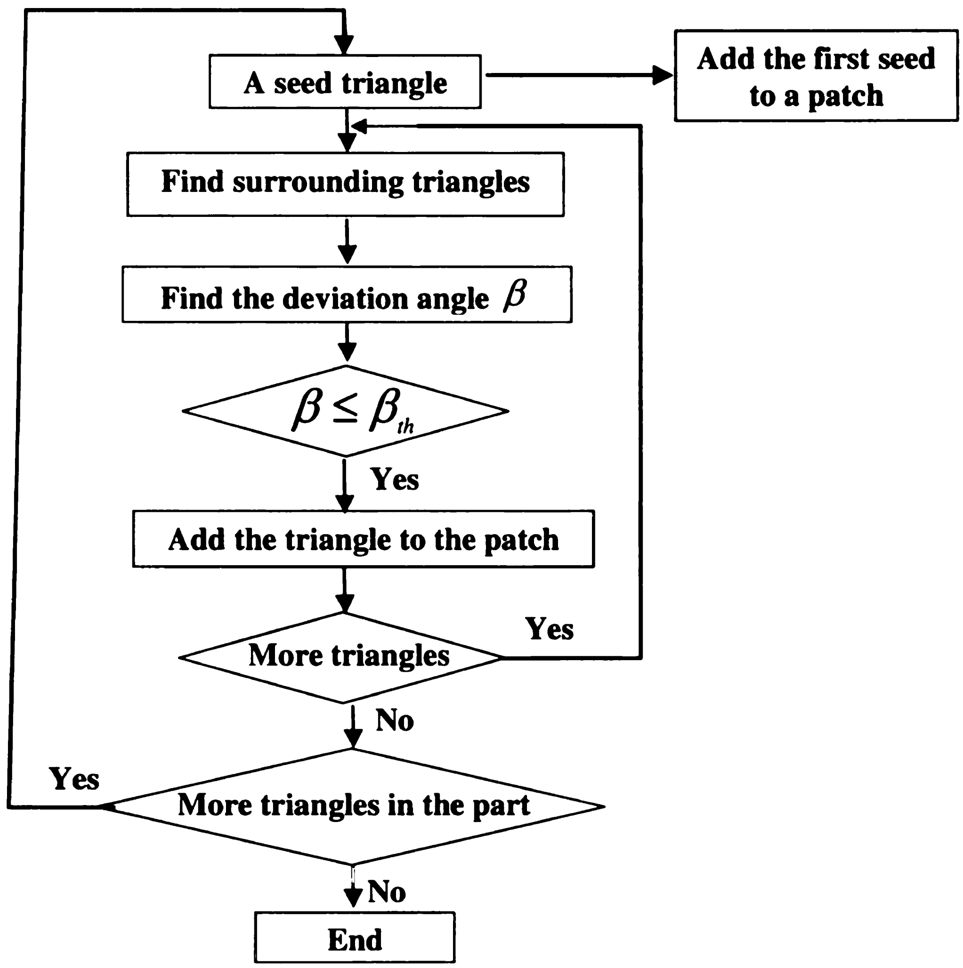

Figure 3.11: The patch forming process.

The steps for the patch generation are:

Step 1: Arbitrarily choose a seed triangle as the first triangle of a patch.

Step 2: Find surrounding triangles. The distance between each surrounding triangle and the seed triangle is less than the spray radius.

Step 3: Calculate the angle between the normal of the seed triangle and the normal of each surrounding triangle.

Step 4: Compare the angle with the threshold angle. If it is less than the threshold angle β_{th}, the triangle is added to the patch.

Step 5: After all of the surrounding triangles are checked, use each of the newly added triangles as a seed triangle.

Step 6: Continue the process until no more triangles can be added to the patch.

Step 7: If there are remaining triangles, choose a seed triangle from the remaining triangles.

Step 8: Repeat steps 2-7 to form a patch.

Step 9: If there are triangles left, repeat steps 2-8 for patch generation until there is no triangle left.

After the process is performed, the free-form surface is divided into one patch or several patches.

3.5 Trajectory Generation for a Patch

A tool trajectory includes the tool position, orientation, and velocity. The tool position is determined by the spray width. After the spray width and the tool velocity are found, a tool trajectory generation algorithm is developed to generate a tool trajectory for a free-form surface.

3.5.1 Tool Path Generation

After patches are formed, a tool trajectory can be generated for each patch using the spray width and the tool velocity. Sheng *et al.* [20] developed a bounding box method to generate a path for a patch. A bounding box of a patch is a box which contains the whole patch exactly. Figure 3.12 shows a patch and its bounding box.

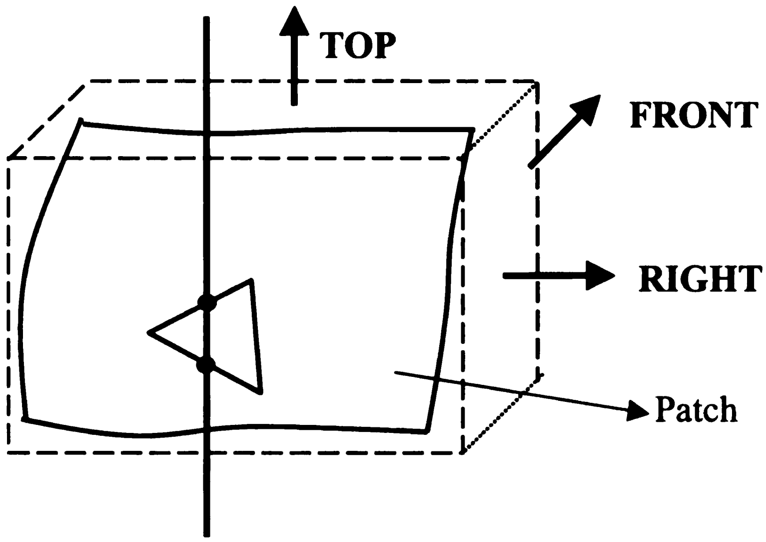

Figure 3.12: A patch and its bounding box: TOP, FRONT and RIGHT are the directions of the bounding box.

The FRONT direction of the bounding box is the opposite direction of the area-weighted average normal of a patch., The average normal direction of a patch with N triangles is defined as:

$$\vec{n}_a = \frac{\sum_{i=1}^{N} s_i \vec{n}_i}{\| \sum_{i=1}^{N} s_i \vec{n}_i \|} \tag{3.26}$$

where $\vec{n}_a$ is the average normal of the surface; $\vec{n}_i$ and s_i are the normal and the area of the ith triangle ($i = 1, ..., N$), respectively. All vertices on a patch are then projected to a plane whose normal is the FRONT direction. The TOP and RIGHT directions are determined by finding the smallest rectangle which can cover all of the projected points on the plane.

Since the bounding box method cannot generate a trajectory to follow the contour of a patch, an improved bounding box method is proposed here to generate a tool path for a patch. Figure 3.13 is an illustration of the path generation algorithm using the improved bounding box method.

The steps for the path generation of a patch are:

Step 1: The patch is cut using a series of top cutting planes, whose normals are the TOP

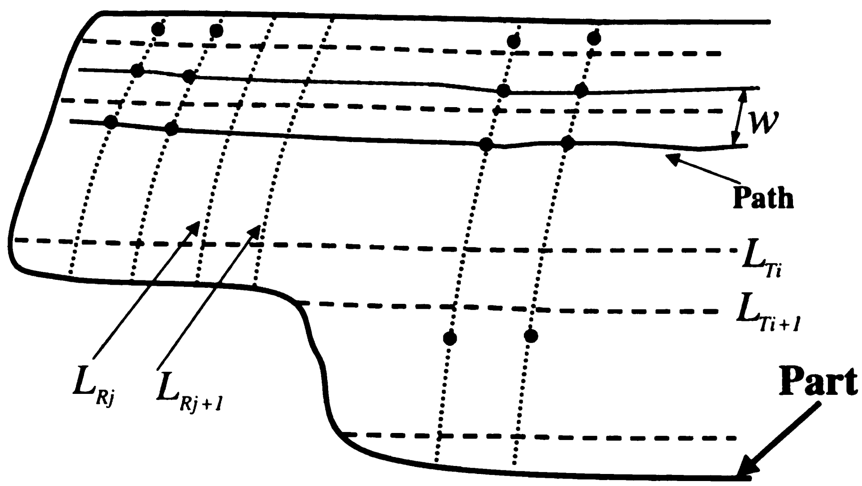

Figure 3.13: The improved bounding box method to generate a path for a patch.

direction. The distance between the neighboring planes is the spray width. A series of top intersecting lines L_{Ti} are obtained, as shown in Figure 3.13.

Step 2: The patch is cut using a series of right cutting planes, whose normals are the RIGHT direction. A series of right intersecting lines L_{Rj} are obtained, as shown in Figure 3.13.

Step 3: For each right intersecting line L_{Rj}, find the number p_i of intersecting points with all of the top intersecting lines. The number p_i is the path number for the right intersecting line L_{Rj}. The procedure is repeated until all of the right intersecting lines are processed.

Step 4: Each right intersecting line is divided into p_i segments. A series of points are obtained. The procedure is repeated until all of the right intersecting lines are divided.

Step 5: Connect the points along the RIGHT direction to form a path.

One of the advantages of the improved bounding box method is that the tool path can follow the contour of a free-form surface.

3.5.2 Tool Orientation Generation

The tool orientation is determined based on the local geometry of a patch. Figure 3.14 shows the tool orientation generation.

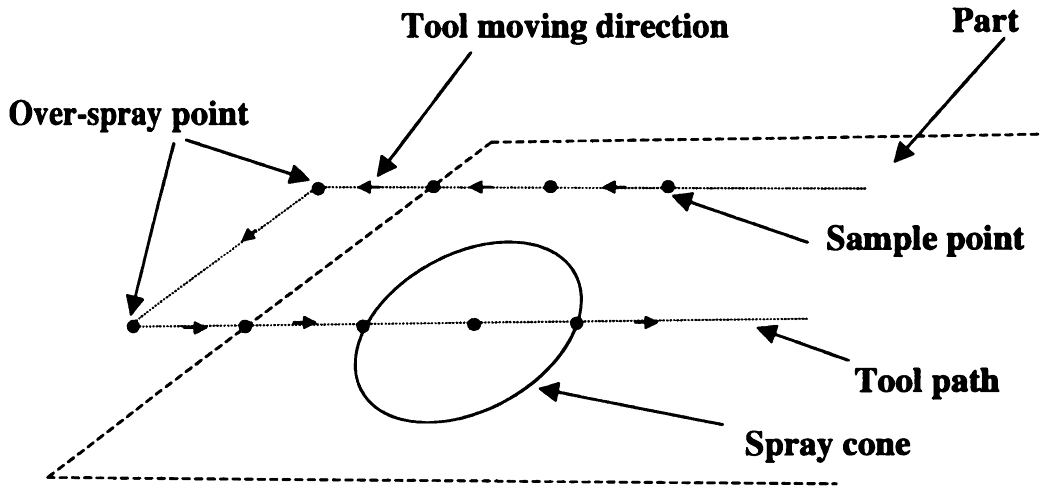

Figure 3.14: Part of a tool path and a series sample points.

At each sample point, triangles whose distance to the sample point is less than the spray radius are found as shown in Figure 3.15.

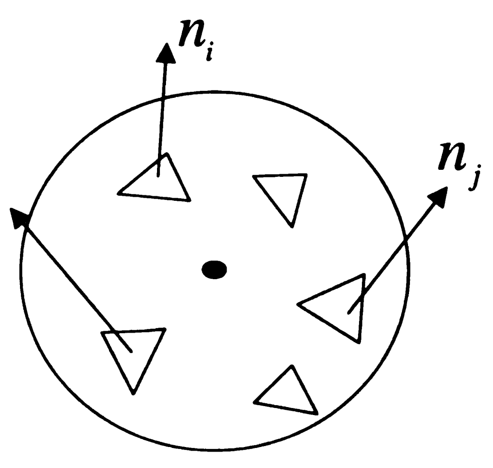

Figure 3.15: Tool orientation generation.

The average normal of these triangles is calculated using equation (3.26). After finding the average normal, the tool orientation is the reverse direction of the average normal. Thus the tool orientation is determined by the local geometry of a free-form surface.

3.5.3 Tool Trajectory Generation

The generated tool trajectory is on a free-form surface. In surface manufacturing, the tool trajectory has to be offset a distance of the tool standoff along the opposite tool direction to form a tool trajectory. Figure 3.16 is an illustration of the process.

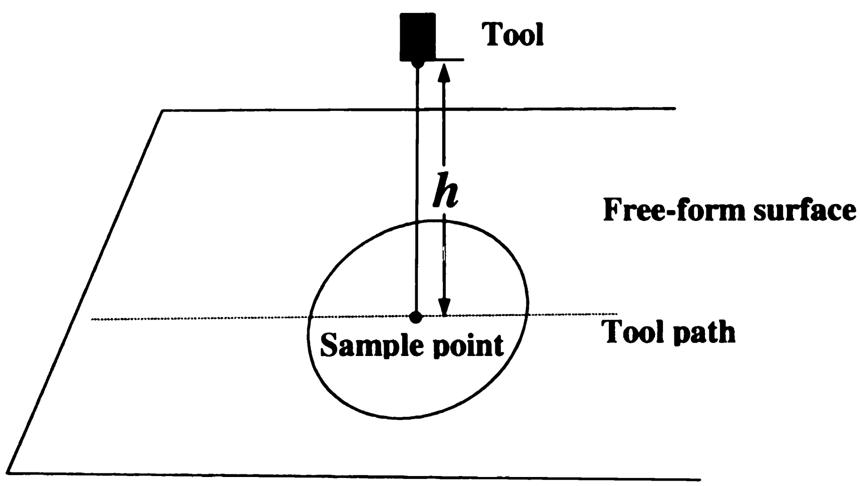

Figure 3.16: A tool trajectory on a free-form surface is projected to form an offset tool trajectory.

After all points on the tool trajectory are offset, an offset tool trajectory is generated.

3.6 Trajectory Verification Model

Trajectory verification is an important process because it checks if the generated trajectories satisfy the given constraints. A trajectory verification model is developed to compute the material thickness on a free-form surface using the generated trajectories. A typical tool model [8, 9, 38, 39] is adopted here to calculate the material thickness of a point on a free-form surface. Figure 3.17 shows the material deposition on a free-form surface. The plane is generated using the tool direction and the desired

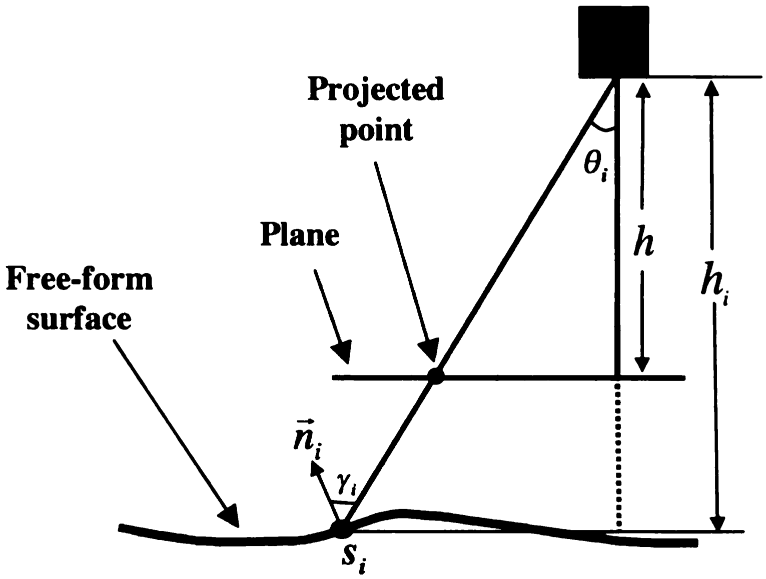

Figure 3.17: Material deposition on a free-form surface. $\vec{n}_i$ is the normal of a triangle; γ_i the deviation angle from the gun direction; h the desired tool standoff; h_i the actual tool standoff.

tool standoff.

The development of the trajectory verification model is based on an assumption that the amount of material from the tool is the same as that sprayed on a free-form surface, which is independent of the geometry of the free-form surface and the distance between the tool and the free-form surface [8, 32, 39, 40]. Suppose the material sprayed on a small area C_1 is projected to the area C_2, as shown in Figure 3.18. The relationship between the two areas is:

$$S_{C_2} = (\frac{h_i}{h})^2 S_{C_1} \tag{3.27}$$

where S_{C_1} and S_{C_2} are the areas of C_1 and C_2 respectively.

Suppose the material on C_1 is projected to C_2. Based on the assumption, the material thickness on C_2 can be expressed as:

$$q_2 = \bar{q}(\frac{h}{h_i})^2 \tag{3.28}$$

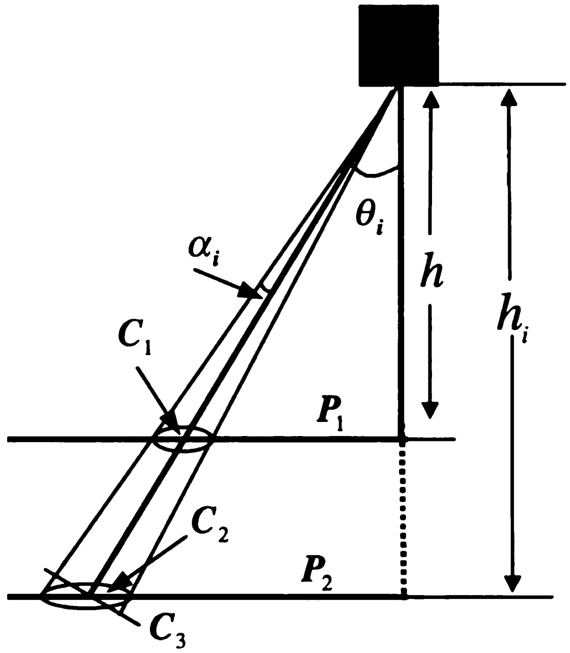

Figure 3.18: The trajectory verification model: material projection.

where $\bar{q}$ and q_2 are the material thicknesses on the planes C_1 and C_2, respectively.

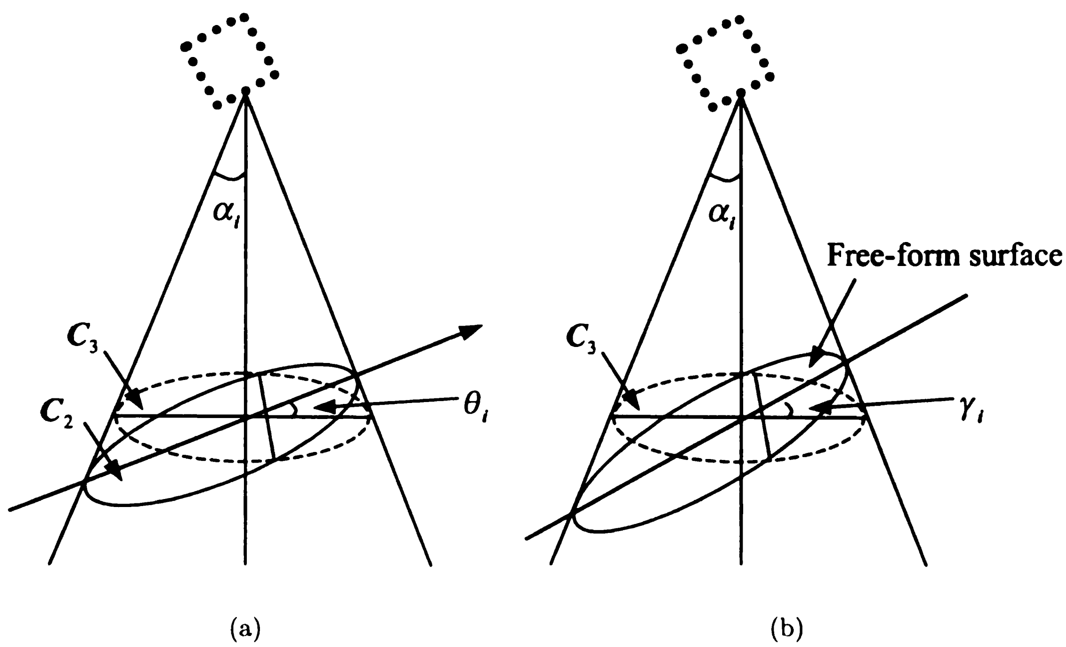

Figure 3.19: Material projection: (a) from C_2 to C_3; (b) from C_3 to a small area on a free-form surface.

Figure 3.19(a) shows a circle C_3, which is perpendicular to the material emission direction. The material thickness on C_3 can be expressed as:

$$q_3 = \frac{q_2}{cos\theta_i}. \tag{3.29}$$

The material on C_3 is projected to the free-form surface with a deviation angle γ_i, as shown in Figure 3.19(b). The material thickness on the free-form surface is:

$$q_s = q_3 cos\gamma_i. \tag{3.30}$$

Therefore, based on equations (3.28), (3.29) and (3.30), the material thickness on the free-form surface can be obtained:

$$q_s = \bar{q}\left(\frac{h}{h_i}\right)^2 \frac{cos\gamma_i}{cos\theta_i}. \tag{3.31}$$

If the distance from the tool to the point s is l_i, then

$$h_i = l_i cos\theta_i. \tag{3.32}$$

Then equation (3.31) can be expressed as:

$$q_s = \bar{q}\left(\frac{h}{l_i}\right)^2 \frac{cos\gamma_i}{cos^3\theta_i}. \tag{3.33}$$

When the deviation angle $\gamma_i > 90^o$, there is no material sprayed on a surface. Hence, the material thickness on a free-form surface can be modeled as:

$$q_s = \begin{cases} \bar{q}\left(\frac{h}{l_i}\right)^2 \frac{cos\gamma_i}{cos^3\theta_i} & \gamma_i \leq 90^o \\ 0 & \gamma_i > 90^o \end{cases}. \tag{3.34}$$

Using this trajectory verification model, the material thickness on a free-form surface can be calculated.

3.7 Suboptimal Tool Velocity

To obtain an optimal tool trajectory for a free-form surface, an optimal tool planning algorithm has to be developed. Optimal tool planning may make the computational load high. To reduce the computational load, a suboptimal tool velocity planning algorithm is developed. The lower and upper bounds of the material distribution are defined as:

$$\Delta q_{max} = q_{max} - q_d \tag{3.35}$$
$$\Delta q_{min} = q_d - q_{min}$$

where q_{max} and q_{min} are the maximum and the minimum material thicknesses on a free-form surface, respectively; Δq_{max} and Δq_{min} the upper and lower bounds, respectively. According to equation (3.19), the upper bound of the material thickness is dependent on the maximum material thickness on a plane. However, the lower bound is dependent on both the minimum material thickness on a plane and the maximum deviation angle of a free-form surface. A larger the maximum deviation angle gives a bigger material thickness deviation. This means the lower bound is larger than the upper bound. To minimize the material thickness deviation from the desired material thickness, the lower bound has to be decreased. A method is developed here to decrease the lower bound by approximately optimizing the tool velocity. Figure 3.20 shows the material thickness projected from a plane to a free-form surface. Because the material of an area S on a plane is projected to an area S' on a free-form surface, the material thickness on the free-form surface is decreased. According to Theorem (3.2.1), the material thickness is inversely proportional to the tool velocity. Therefore, the tool velocity can be modified to increase the material

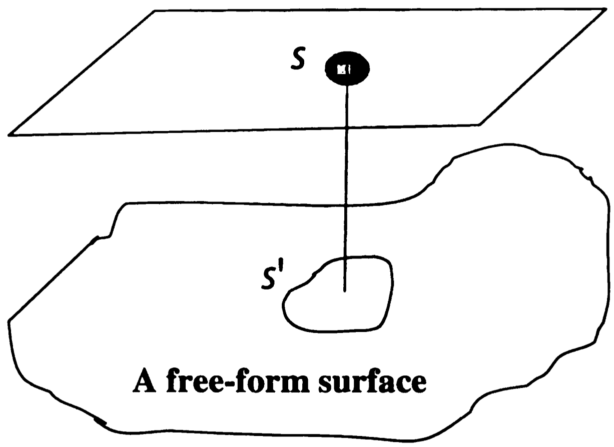

Figure 3.20: The material thickness projected from a plane to a free-form surface.

thickness on the free-form surface, i.e.,

$$v' = v\frac{S}{S'} \tag{3.36}$$

where v' is the approximately optimized tool velocity. Thus, we have,

$$q_{s'} = q_s \tag{3.37}$$

Hence, the material thickness deviation from the desired material thickness is decreased using the suboptimal velocity algorithm.

CHAPTER 4

TOOL TRAJECTORY INTEGRATION

A free-form surface may consist of several patches. After the trajectory for each patch is generated, the trajectories of the patches have to be integrated to obtain a trajectory for the free-form surface. In this chapter, a trajectory integration algorithm for a surface with multiple patches is developed.

4.1 Material Distribution in the Intersecting Area of Two Patches

The material thickness optimization of a surface with two patches is much more complex than that of a surface with one patch. The overlapping distance and the tool velocity should be kept the same as those of a surface with one patch except at the intersecting areas among patches. In the intersecting area, the path in one patch contributes to the material thickness on the other. Figure 4.1 shows two patches with an angle α.

In Figure 4.1, O is the spray tool center; O_1, O_2, O_3, s_1 and s_2 are points on the two patches; h_1 is the distance from O_1 to O_3; h_2 the distance from O_2 to O_3; l_i the distance from O to s_2; x the distance from O_1 to s_1; y the distance from s_2 to O_2. The distance l from O_3 to s_2 can be expressed as:

$$\begin{aligned} l &= \frac{(x - h_1)cos\theta}{cos(\theta + \alpha)} \\ l &= h_2 - y. \end{aligned} \tag{4.1}$$

Using the trajectory verification model (3.33), the material thickness on Patch 2

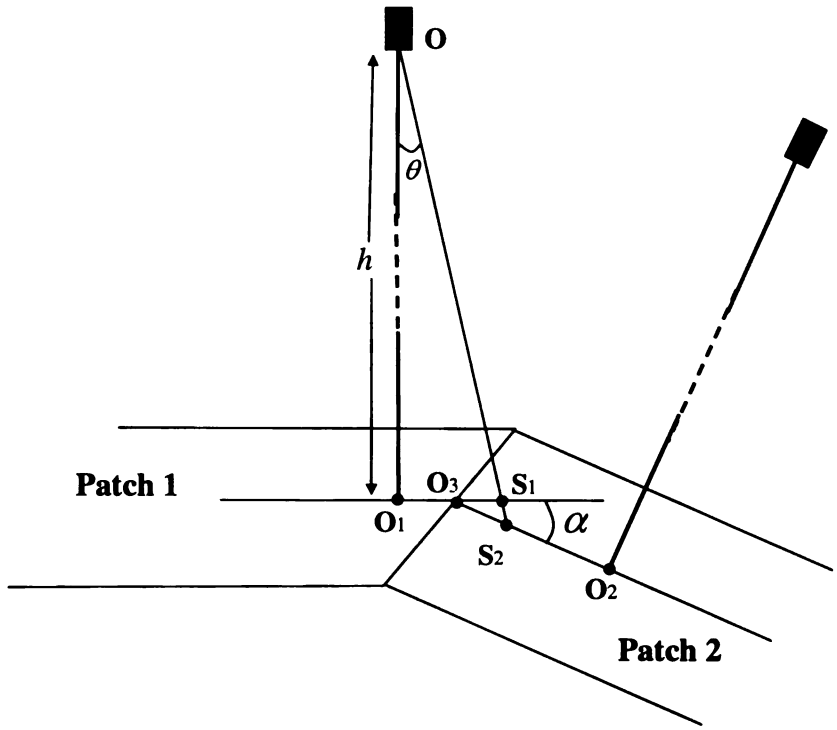

Figure 4.1: The material distribution on the intersecting area of two patches.

can be expressed as:

$$q_{s_2}(x, y) = q_2(y) + q_1(x)\frac{h^2 cos(\theta + \alpha)}{l_i^2 cos^3\theta}. \tag{4.2}$$

Equations (4.1) and (4.2) lead to:

$$q_{s_2}(x) = q_2(y) + q_1(h_1 + \frac{(h_2 - y)cos(\theta + \alpha)}{cos\theta})\frac{h^2 cos(\theta + \alpha)}{l_i^2 cos^3\theta}. \tag{4.3}$$

Equation (4.3) is quite complicated if it is used to calculate the material thickness at the intersecting area of two patches. Since the tool standoff h is much larger than the spray radius, i.e.,

$$R \ll h. \tag{4.4}$$

Therefore, the angle θ is a small angle. Then the following approximations are valid:

$$tan\theta \approx 0, \qquad h \approx l_i cos\theta. \tag{4.5}$$

Equation (4.3) can be simplified as:

$$q_{s_2}(y) = q_2(y) + q_1(h_1 + (h_2 - y)cos\alpha)cos\alpha. \tag{4.6}$$

$\alpha > 90^o$ is not considered here because the material thickness on one patch is not affected when spraying the other patch.

Similarly, the material thickness on Patch 1 is computed:

$$q_{s_1}(x) = q_1(x) + q_2(h_2 + (h_1 - x)cos\alpha)cos\alpha. \tag{4.7}$$

4.2 Optimization Process for a Surface with Two Patches

According to the criteria that the main part of a tool path is parallel or perpendicular to the intersecting line, different cases are studied: parallel-parallel (PA-PA) case; parallel-perpendicular (PA-PE) case; perpendicular-perpendicular (PE-PE) case. Figure 4.2 shows the three cases.

4.2.1 Case 1: Parallel-parallel (PA-PA) Case

Figure 4.3 shows the PA-PA case.

In this case, we need to optimize the distance h between the two paths. Because the two paths are symmetric, the distances of the two paths to the intersecting line are the same. Since the material distribution on any line which is parallel to the intersecting line is the same, we only need to consider the material thickness on OA as shown in Figure 4.3. Suppose the angle between the two patches is α. The material

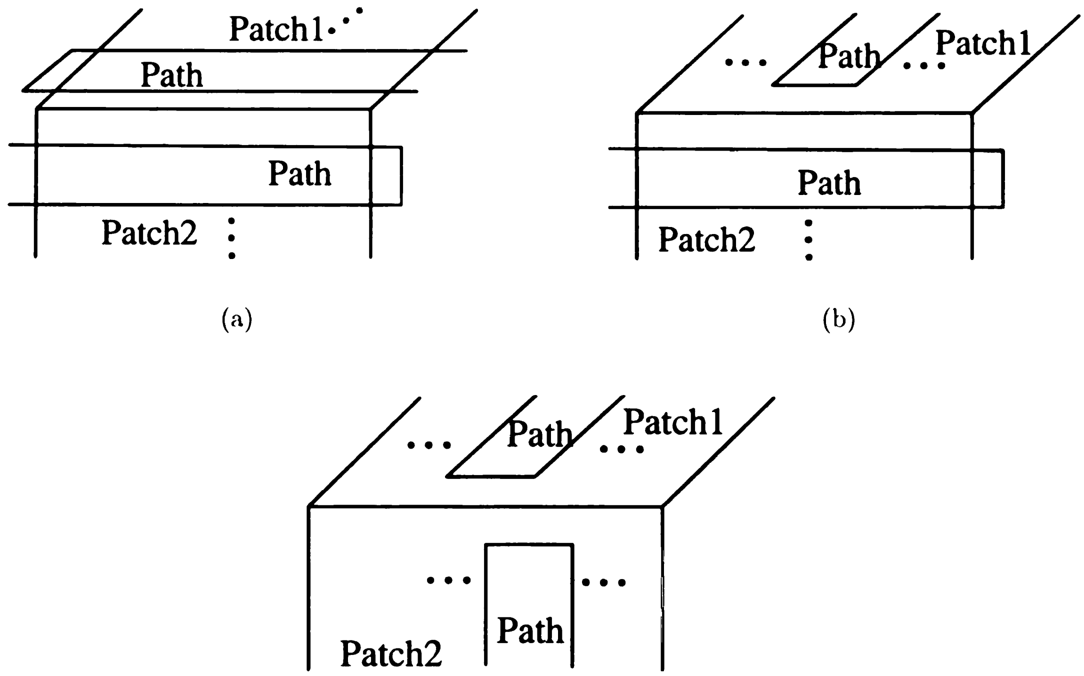

(a) (b) (c)

Figure 4.2: (a) Case 1: parallel-parallel case; (b) Case 2: parallel-perpendicular case; (c) Case 3: perpendicular-perpendicular case.

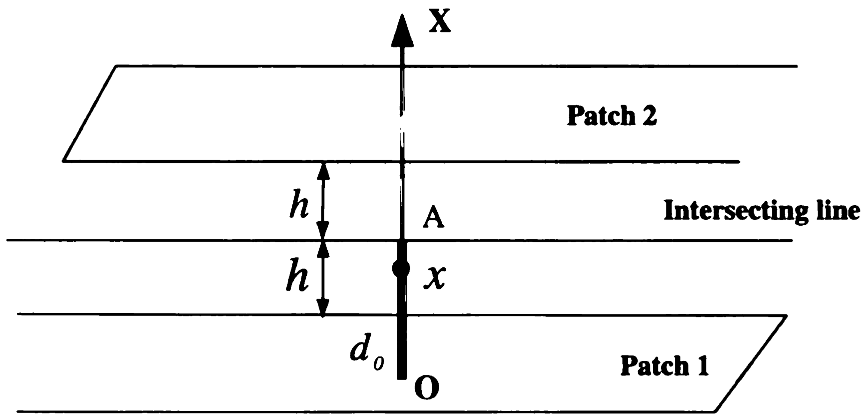

Figure 4.3: Parallel-parallel (PA-PA) case.

thickness on OA can be expressed as:

$$q(x) = q_1(|x - d_0|) + q_2(h + (d_0 + h - x)cos\alpha)cos\alpha \tag{4.8}$$

where $q_1(x)$ and $q_2(x)$ are the material thicknesses due to the paths in Patch 1 and Patch 2, respectively, which can be expressed as:

$$q_1(y) = 2\int_0^{\frac{\sqrt{R^2-y^2}}{v}} f(\sqrt{(vt)^2+y^2})dt$$
$$q_2(y) = 2\int_0^{\frac{\sqrt{R^2-y^2}}{v}} f(\sqrt{(vt)^2+y^2})dt. \tag{4.9}$$

Then, the error function can be formulated as:

$$E_1(h) = \int_0^{h+d_0} (q_d - q(x))^2 dx. \tag{4.10}$$

Since the maximum and the minimum material thicknesses determine the maximum material thickness deviation from the average material thickness, they have to be minimized, i.e.,

$$E_2(h) = (q_{max} - q_d)^2 + (q_d - q_{min})^2 \tag{4.11}$$

where q_{max} and q_{min} are the maximum and the minimum material thicknesses, respectively.

Finally, a multi-objective optimization problem is formulated using equations (4.10) and (4.11),

$$\min_h \left\{E = (E_1, E_2)^T\right\}. \tag{4.12}$$

The optimization problem can be solved using the method in Appendix A.

4.2.2 Case 2: Parallel-perpendicular (PA-PE) Case

Figure 4.4 shows the PA-PE case.

The highlighted area can represent the intersecting area due to the symmetry of the material distribution in the intersecting area. To obtain the optimal material distribution, the paths are divided into small segments to optimize the tool velocity.

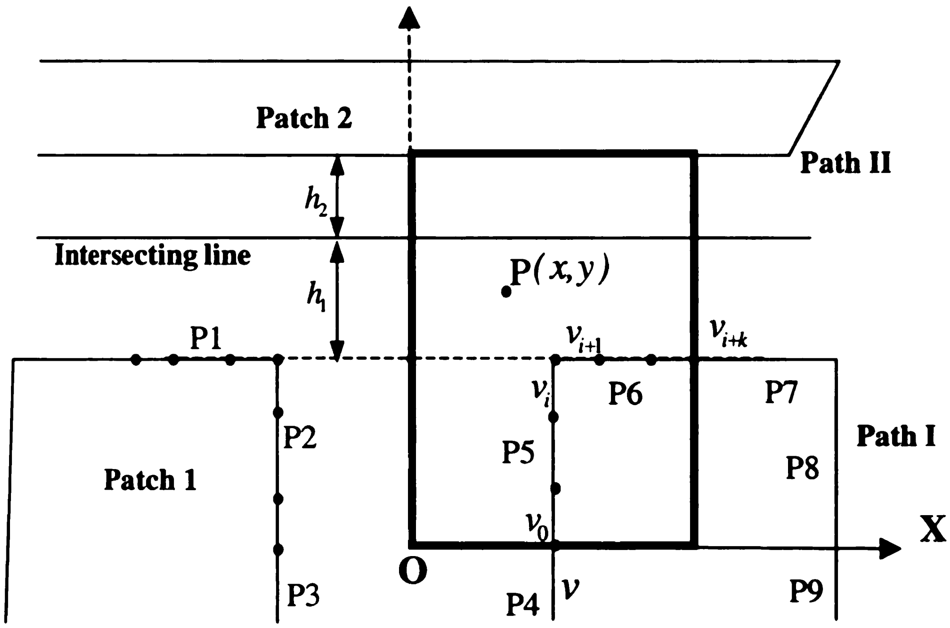

Figure 4.4: Parallel-perpendicular(PA-PE) case.

The material thickness on point P in the highlighted area due to Path I can be calculated using the path segments P_i $(i = 1, \ldots, 9)$ shown in Figure 4.4.

P1, P6 and P7:

$$q_{P1,6,7}(x, y, j) = \frac{1}{v_j} \int_{\frac{2R-d}{2k}(j-i-1)}^{\frac{2R-d}{2k}(j-i)} f(\gamma) dz,$$

$$\gamma = \sqrt{(z + z_0)^2 + (d_0 - y)^2},$$

$$\text{P1}, \quad z_0 = \frac{2R - d}{2} + x,$$

$$\text{P6}, \quad z_0 = \frac{2R - d}{2} - x,$$

$$\text{P7}, \quad z_0 = x - \frac{3(2R - d)}{2}.$$

P2, P5 and P8:

$$
\begin{aligned}
q_{p_{2,5,8}}(x,y,j) &= \frac{1}{v_j}\int_{\frac{j}{i+1}d_0}^{\frac{j+1}{i+1}d_0} f(\gamma)dz,\\
\gamma &= \sqrt{(x+x_0)^2+(z-y)^2},\\
\text{P2},\quad x_0 &= \frac{2R-d}{2},\\
\text{P5},\quad x_0 &= -\frac{2R-d}{2},\\
\text{P8},\quad x_0 &= -\frac{3(2R-d)}{2}.
\end{aligned}
$$

P3, P4 and P9:

$$
\begin{aligned}
q_{p_{3,4,9}}(x,y) &= \frac{1}{v}\int_0^R f(\gamma)dz,\\
\gamma &= \sqrt{(x+x_0)^2+(z-y-R)^2},\\
\text{P3},\quad x_0 &= \frac{2R-d}{2},\\
\text{P4},\quad x_0 &= -\frac{2R-d}{2},\\
\text{P9},\quad x_0 &= -\frac{3(2R-d)}{2}.
\end{aligned}
\tag{4.13}
$$

where $q_{p_{.,.,.}}$ represents the material thickness due to the path segments. Then the material thickness q_I on point P due to the path in Patch 1 is:

$$
q_I(x,y) = \sum_{j=0}^{i} q_{p_{1,6,7}}(x,y,j) + \sum_{j=i+1}^{i+k} q_{p_{2,5,8}}(x,y,j) + q_{p_{3,4,9}}(x,y). \tag{4.14}
$$

Since the path in Patch 2 is parallel to the intersecting line, the material thickness q_{II} on point P due to the path in Patch 2 is:

$$
q_{II}(y_1) = \tfrac{2}{v}\int_0^{\sqrt{R^2-y_1^2}} f(\sqrt{z^2+y_1^2})dz \tag{4.15}
$$

where y_1 is the distance from a point to the path in Patch 2. Then the material thickness on point P can be calculated using equations (4.6) and (4.7):

$$
q(x,y) = \begin{cases} q_I(x,y) + q_{II}(h_2 + (h_1 + d_0 - y)cos\alpha)cos\alpha & 0 \leq y \leq (h_1 + d_0) \\ q_I(x, h_1 + d_0 + (y - h_1 - d_0)cos\alpha)cos\alpha + & \\ \quad q_{II}(h_2 + y - h_1 - d_0) & h_1 + d_0 < x \leq h_1 + h_2 + d_0 \end{cases} \quad . \tag{4.16}
$$

Then an error function can be formulated:

$$
E_1 = \int_0^{2R-d} \int_0^{d_0+h_1+h_2} (q_d - q(x,y))^2 dydx. \tag{4.17}
$$

Similar to the PA-PA case, the maximum and minimal material thickness deviations from the average material thickness have to be minimized, i.e.,

$$
E_2 = (q_{max} - q_d)^2 + (q_d - q_{min})^2 \tag{4.18}
$$

where q_{max} and q_{min} are the maximum and the minimum material thicknesses, respectively.

Finally, a multi-objective optimization problem is formulated using equations (4.17) and (4.18),

$$
\min_{h_1,h_2,v} \left\{ E = (E_1, E_2)^T \right\}. \tag{4.19}
$$

This problem can be solved using the method in Appendix A.

4.2.3 Case 3: Perpendicular-perpendicular (PE-PE) Case

Figure 4.5 shows the PE-PE case.

The highlighted area can represent the intersecting area due to the symmetry of the material distribution in the intersecting area. The material thickness on point P in the highlighted area due to the path in Patch 1 is the same as that in PA-PE case, which can be calculated using equation (4.14). The material thickness due to

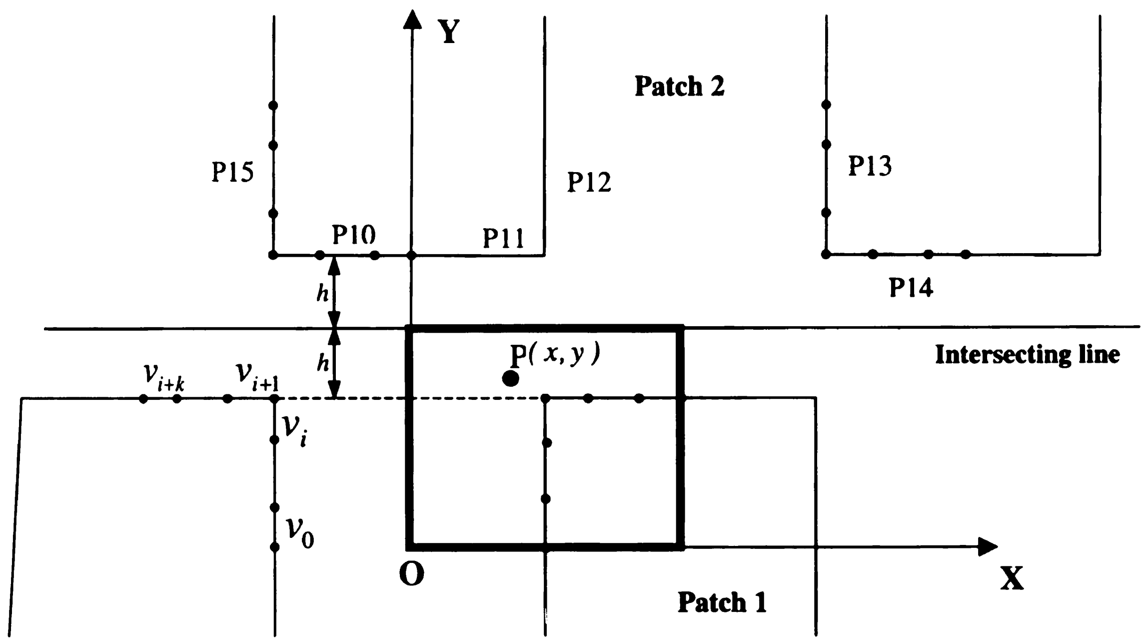

Figure 4.5: Perpendicular-perpendicular (PE-PE) case.

the path segments P_i ($i = 10, ...15$) in Patch 2 can be formulated as:

$$
\begin{aligned}
&\text{P10, P11 and P14:}\\
&q_{p_{10,11,14}}(x,y,j) = \frac{1}{v_j}\int_{\frac{2R-d}{2k}(j-i-1)}^{\frac{2R-d}{2k}(j-i)} f(\gamma)dz,\\
&\gamma = \sqrt{(z+z_0)^2 + (h + (d_0 + h - y)cos\alpha)^2},\\
&\quad \text{P10,} \quad z_0 = -\frac{2R-d}{2} - x,\\
&\quad \text{P11,} \quad z_0 = -\frac{2R-d}{2} + x,\\
&\quad \text{P14,} \quad z_0 = \frac{3(2R-d)}{2} - x.\\
&\text{P12, P13 and P15:}\\
&q_{p_{12,13,15}}(x,y,j) = \frac{1}{v_j}\int_{\frac{j}{i+1}d_0}^{\frac{j+1}{i+1}d_0} f(\gamma)dz,\\
&\gamma = \sqrt{(x+x_0)^2 + (d_0 + h + (d_0 + h - y)cos\alpha - z)^2},\\
&\quad \text{P2,} \quad x_0 = -\frac{2R-d}{2},\\
&\quad \text{P5,} \quad x_0 = -\frac{3(2R-d)}{2},\\
&\quad \text{P8,} \quad x_0 = \frac{2R-d}{2}.
\end{aligned} \tag{4.20}
$$

Then the material thickness on the point P can be calculated:

$$q(x,y) = q_I(x,y) + q_{II}(x,y)cos\alpha \tag{4.21}$$

where

$$q_{II}(x,y) = \sum_{j=0}^{i} q_{P12,13,15}(x,y,j) + \sum_{j=i+1}^{i+k} q_{P10,11,14}(x,y,j). \tag{4.22}$$

Then an error function can be formulated:

$$E_1 = \int_0^{2R-d} \int_0^{d_0+h} (q_d - q(x,y))^2 dydx. \tag{4.23}$$

Similar to the PA-PA case, the maximum and minimal material thickness deviations from the average material thickness have to be minimized, i.e.,

$$E_2 = (q_{max} - q_d)^2 + (q_d - q_{min})^2 \tag{4.24}$$

where q_{max} and q_{min} are the maximum and the minimum material thicknesses, respectively.

Finally, a multi-objective optimization problem is formulated using equations (4.23) and (4.24),

$$\min \left\{ E = (E_1, E_2)^T \right\}. \tag{4.25}$$

This problem can be solved using the method in Appendix A.

4.3 Optimization Process for a Surface with Multiple Patches

According to the types of intersecting areas, a surface with multiple patches can be categorized into two cases: Point and Line. If the patches intersect in a point, it is called Point case. If the patches intersect in lines, it is called Line case. The two cases are discussed individually. Some surfaces may have both cases.

4.3.1 Point Case of a Surface with Multiple Patches

Figure 4.6 shows the Point case of a surface with three patches.

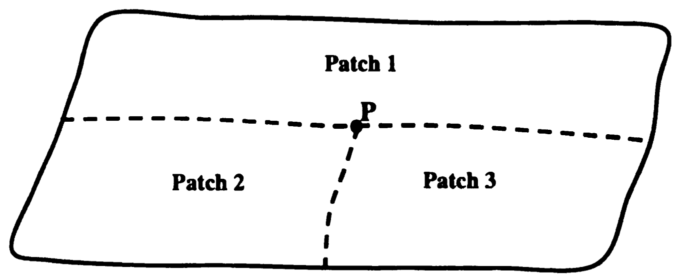

Figure 4.6: The Point case.

The material distribution between Patch 1 and Patch 2, Patch 2 and Patch 3, Patch 1 and Patch 3 is optimized. The only part we need to consider is the thickness on the area around the intersecting point P. Since the material thickness between Patch 2 and Patch 3 is optimized, we can merge them into one patch: Patch I. The material thickness on Patch I is optimized. Since the material thickness between Patch 1 and Patch 3, Patch 1 and Patch 2 is optimized, the material thickness between Patch I and Patch 1 is optimized too. Hence, the material thickness on the area around the intersecting point P is optimized.

This method can be applied to a surface with more than three patches which intersect at one point. Therefore, if the material thickness between any two patches is optimized, the material thickness on a surface that consists of multiple patches must be optimized.

4.3.2 Line Case of a Surface with Multiple Patches

If one patch is between the other two patches, as shown in Figure 4.7, there are different cases depending on the patterns of the paths.

In Figure 4.7(a), because the path in Patch 2 is perpendicular to the intersecting lines, the PA-PE or PE-PE cases can be applied to determine the parameters. How-

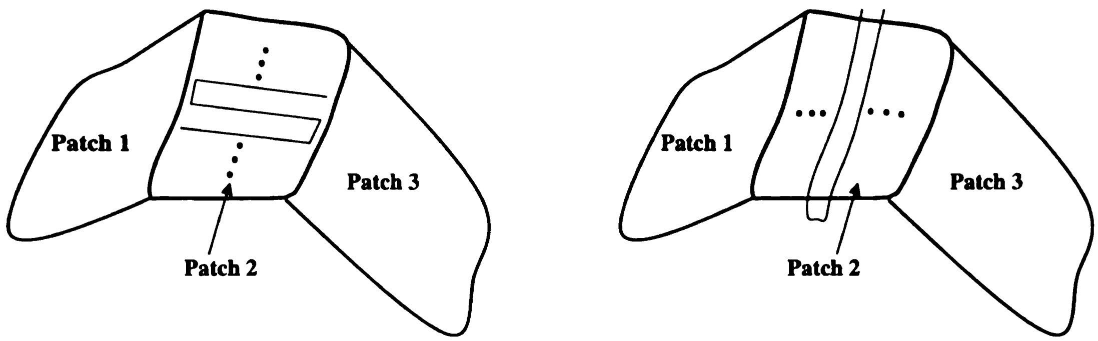

(a) (b)

Figure 4.7: A surface with three patches: (a) perpendicular path for patch 2; (b) parallel path for patch 2.

ever, for the case in Figure 4.7(b), the path in Patch 2 is parallel to the intersecting lines. If the optimal h is applied, the actual spray width for the rest area of Patch 2 may not be the optimal spray width. Since the material distribution in the intersecting area is more sensitive to h, the spray width has to be modified. Here two methods are developed to change the spray width for Patch 2.

Method 1:

The spray width can be changed in a certain range without affecting the maximum and minimum material distribution too much. Table 4.1 shows the relationship between the spray width, the maximum and the minimum material thicknesses. The velocity is obtained by optimizing a spray process on a plane when the spray width is given. Spray painting is used as an example. The conditions are the average material thickness $q_d = 50\ \mu m$, the spray radius $R = 50\ mm$ and the paint deposition rate $f(r) = \frac{1}{10}(R^2 - r^2)\ \mu m/s$.

When the spray width is increased/decreased about 5 mm, the maximum material thickness deviation from the average increases about 5 μm. Figure 4.8(a) shows the relationship between the spray width and the tool velocity. The relationship between the spray width and the maximum and the minimum material thicknesses is shown

Table 4.1: The relationship between the spray width and the maximum and the minimum material thicknesses

Spray Width (mm)	Velocity (mm/s)	q_{max} (μm)	q_{min} (μm)
66.0	310.0	54.1	45.0
65.0	312.9	53.6	45.7
64.0	315.9	53.1	46.3
62.0	320.9	52.3	47.4
60.8	323.3	52.0	48.0
59.5	333.4	52.3	47.5
58.0	344.0	52.8	46.8
55.0	363.5	53.8	45.5

in Figure 4.8(b).

Method 2:

From Method 1, the spray width cannot be changed too much since the maximum material thickness deviation increases as the the spray width deviation from the desired spray width increases. The tool height can also be adjusted to change the spray width. Figure 4.9 shows the tool height is increased from the desired tool height.

In Figure 4.9,

$$\alpha_i = \gamma_i. \tag{4.26}$$

Therefore, equation (3.31) can be written as:

$$q_s = \bar{q}\left(\frac{h}{h_i}\right)^2 \tag{4.27}$$

where q_s is the material thickness on point S. From Theorem (3.2.1), the material

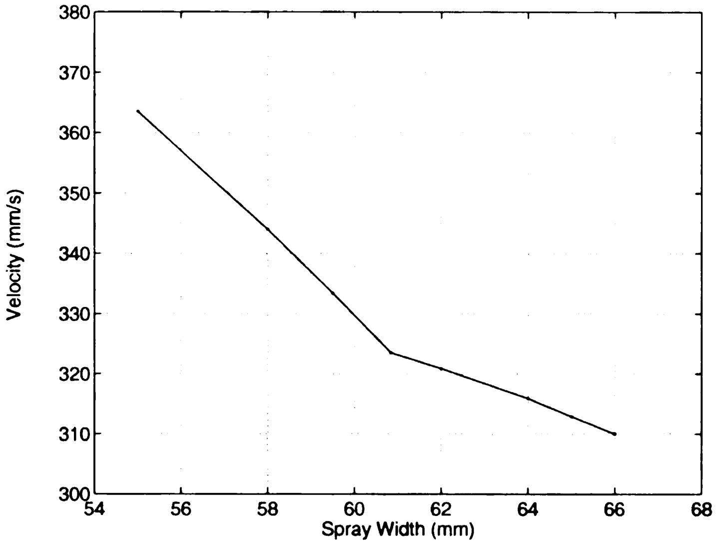

(a)

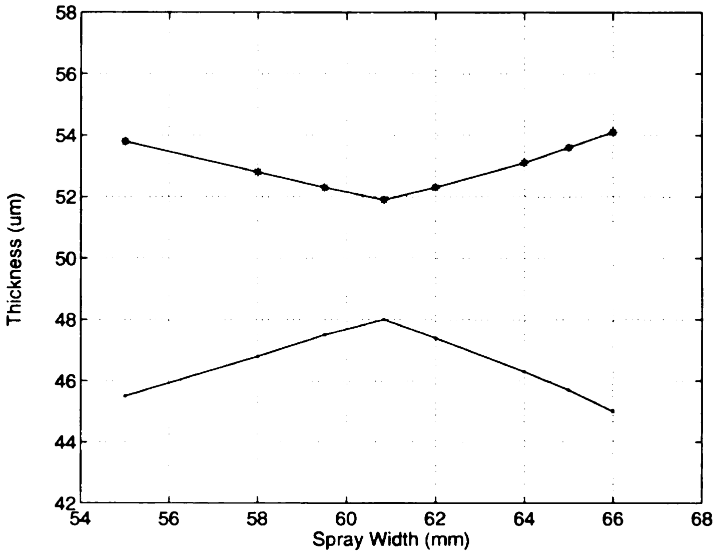

(b)

Figure 4.8: The relationship between the spray width and (a) velocity; (b) the maximum and minimum material thicknesses.

thickness is inversely proportional to the tool velocity. Thus, the material thickness on point S can be increased. If

$$q_s = \bar{q}, \tag{4.28}$$

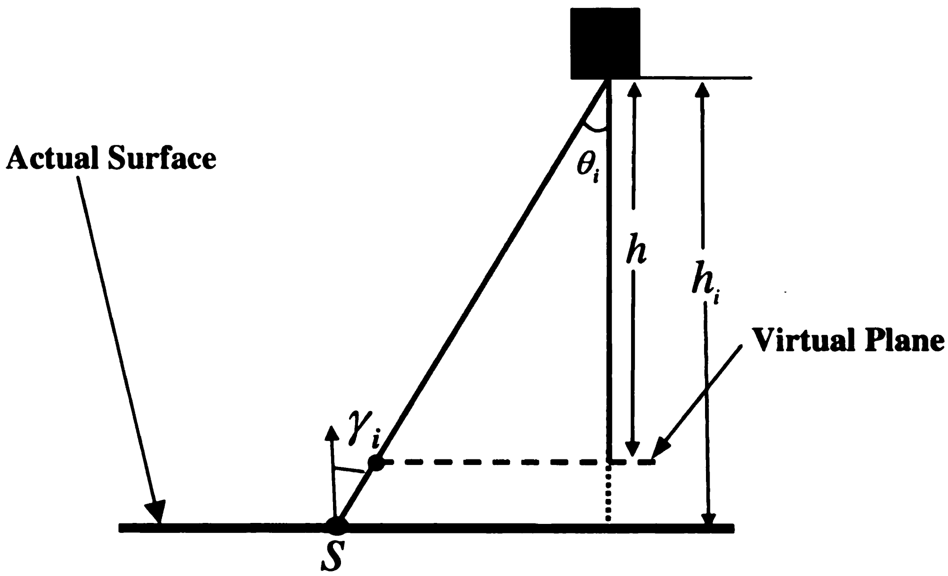

Figure 4.9: The tool height is increased from the desired tool standoff.

then

$$v' = v\left(\frac{h}{h_i}\right)^2 \tag{4.29}$$

where v' is the modified velocity. This means the maximum material thickness deviation is the same as before. However, since the tool height is changed, the spray radius becomes

$$R' = R\frac{h_i}{h} \tag{4.30}$$

where R' is the modified spray radius. The spray width is also changed,

$$w' = w\frac{h_i}{h}. \tag{4.31}$$

From equations (4.28) and (4.31), the spray width can be modified without sacrificing the maximum material thickness deviation. However, since the spray radius is changed, the optimization process for the intersecting area has to be performed again to obtain the optimal distance(s). This makes the integration problem more complicated.

CHAPTER 5

IMPLEMENTATION OF AUTOMATED TOOL PLANNING

In this chapter, the automated tool planning is implemented to generate trajectories for different processes, such as spray painting, spray forming and indirect rapid tooling. The generated trajectories are also verified using the trajectory verification model. The trajectory integration algorithm is also implemented. Since coverage is a special case of material uniformity, implementation for coverage is not discussed here. The algorithm was implemented in C++. The triangular approximation was exported from GID (http://gid.cimne.upc.es/) with an error tolerance of 2 mm.

5.1 Optimization Process

The material thickness optimization process is performed for spray painting because the optimization for other applications is similar.

5.1.1 Determination of Tool Trajectory Parameters

Suppose the desired paint thickness is $q_d = 50\ \mu m$, the required paint thickness deviation $15 \mu m$ and the spray radius $R = 50\ mm$. The paint deposition rate is:

$$f(r) = \frac{1}{10}(R^2 - r^2)\ \mu m/s. \tag{5.1}$$

The paint gun velocity and overlapping distance are calculated by optimizing equation (3.12):

$$v = 323.3\ mm/s, \qquad d = 39.2\ mm. \tag{5.2}$$

The maximum and minimum thicknesses are:

$$\bar{q}_{max} = 52.02 \ \mu m, \qquad \bar{q}_{min} = 48.05 \ \mu m. \tag{5.3}$$

The optimized paint thickness on a plane is shown in Figure 5.1.

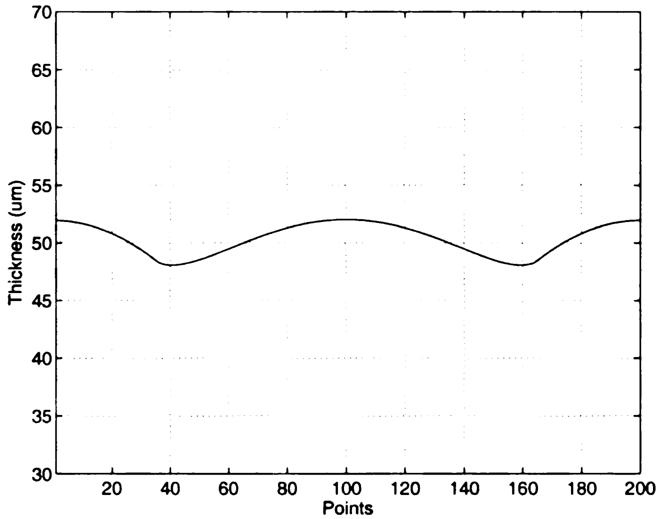

Figure 5.1: The optimized paint thickness on a plane.

Using the maximum and minimum thicknesses and equation (3.22), the threshold angle is calculated:

$$\beta_{th} = 43.2^o. \tag{5.4}$$

5.1.2 Paint Thickness Optimization for a Surface with Two Patches

Case 1: Parallel-parallel (PA-PA) Case

In this case, $d_0 = R$. After performing the optimization process using equation (4.12), the optimized paint thickness for $\alpha = 30^o$ is shown in Figure 5.2.

Case 2: Parallel-perpendicular (PA-PE) Case

For this case, $i = 3$, $d_0 = 2R$ and $k = 4$ are chosen. The optimization process is performed using equation (4.19). The optimized paint gun velocities when $\alpha = 30^o$

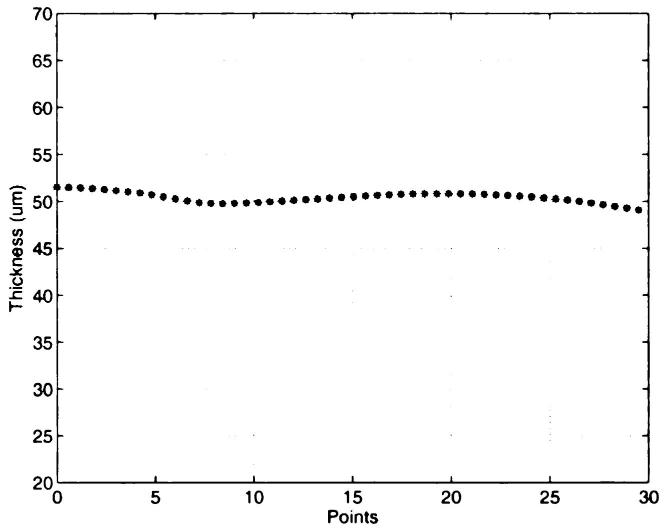

Figure 5.2: The optimized paint thickness for the PA-PA case when $\alpha = 30^o$.

are:

$$v_0 = 272.2mm/s, \quad v_1 = 333.1mm/s, \quad v_2 = 459.2mm/s, \quad v_3 = 336.4mm/s,$$

$$v_4 = 226.7mm/s, \quad v_5 = 355.3mm/s, \quad v_6 = 547.2mm/s, \quad v_7 = 690.8mm/s.$$

The optimized paint thickness for $\alpha = 30^o$ is shown in Figure 5.3.

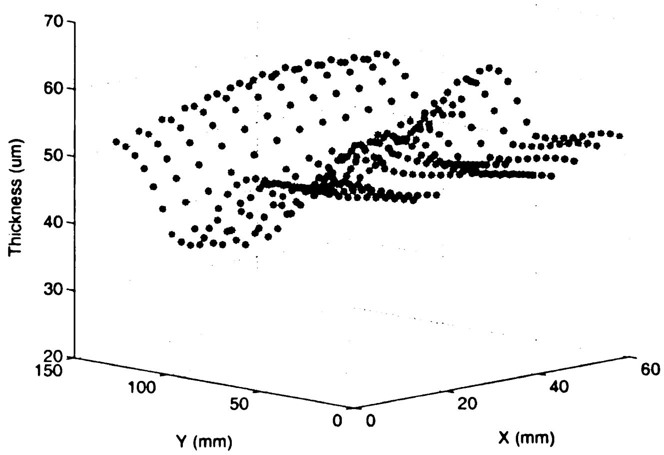

Figure 5.3: The optimized paint thickness for the PA-PE case when $\alpha = 30^o$.

Case 3: Perpendicular-perpendicular (PE-PE) Case

For this case, $i = 3$, $d_0 = 2R$ and $k = 4$ are chosen. The optimization process is performed using equation (4.25). The optimized paint gun velocities when $\alpha = 30^o$ are:

$$v_0 = 252.0mm/s, \quad v_1 = 308.4.1mm/s, \quad v_2 = 425.2, \quad v_3 = 311.5mm/s, mm/s$$

$$v_4 = 209.9mm/s, \quad v_5 = 329.0mm/s, \quad v_6 = 506.7mm/s, \quad v_7 = 639.6mm/s.$$

The optimized paint thickness for $\alpha = 30^o$ is shown in Figure 5.4.

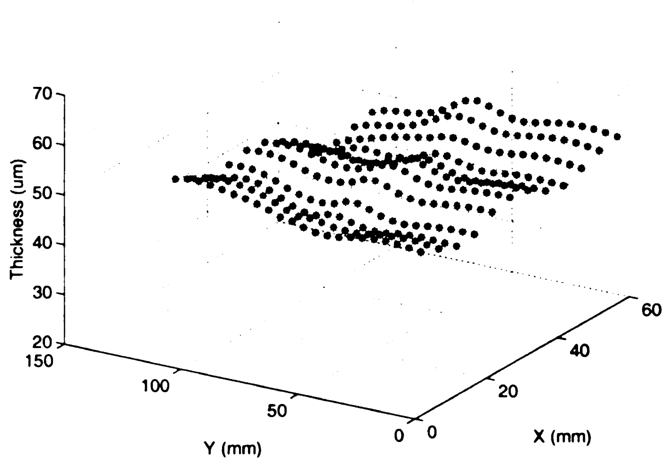

Figure 5.4: The optimized paint thickness for the PE-PE case when $\alpha = 30^o$.

The maximum and the minimum thicknesses for the three cases with $\alpha = 30^o$ are summarized and shown in Table 5.1.

The results in Table 5.1 show that the PA-PA case achieves satisfactory results. The paint thickness deviation is about $1.5\mu m$. The paint thickness deviation for the PE-PE case is about $5.4\mu m$. However, for the PA-PE case, the paint thickness deviation is about $10\mu m$. Therefore, the PA-PE case should be avoided in tool trajectory planning.

Table 5.1: The maximum and minimum thicknesses for the three cases when $\alpha = 30^o$

Thickness	q_{min} (μm)	q_{max} (μm)
PA-PA	48.8	51.5
PA-PE	40.7	59.4
PE-PE	44.6	55.8

5.2 Spray Painting

5.2.1 Trajectory Generation and Verification

Three parts, portion of a car hood, fender and door, shown in Figures 2.3, 5.5(a) and 5.5(b), respectively, are used to test the algorithm. The car hood, fender, and door have 3320 , 9355 and 4853 triangles, respectively.

Using the patch forming method, the car hood, fender and door form only one patch each.

The tool paths are generated using the improved bounding box method in Section 3.5.1. The generated tool paths are shown in Figures 5.6(a), 5.6(b) and 5.6(c) for the car hood, fender and door, respectively.

The gun direction is computed for each sample point and the maximum deviation angle is calculated for each part, respectively. The number of triangles and the maximum deviation angle for each part are shown in Table 5.2.

The maximum deviation angles β in Table 5.2 are less than the threshold angle β_{th} for the three parts. This means the generated gun trajectories can satisfy the thickness requirements.

When simulating the paint thickness on a free-form surface, the paint thickness of randomly chosen points on the car hood, fender and door are computed and shown in Figures 5.7(a), 5.7(b) and 5.7(c), respectively. The average, maximum, and minimum

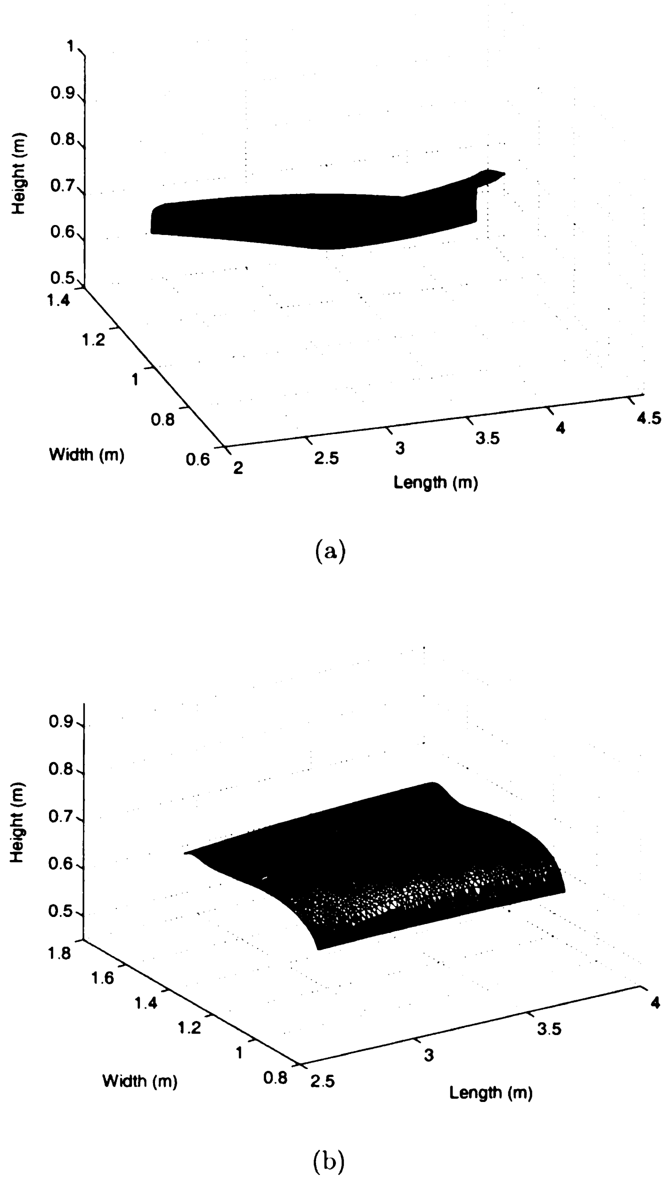

Figure 5.5: The triangular approximation of (a) a car fender; (b) a car door.

paint thicknesses are calculated and summarized in Table 5.3. The simulation results show that the average, maximum and minimum thicknesses for the car hood, fender and door satisfy the thickness requirements. The trajectories generated using the automated tool planning algorithm can achieve required paint thickness. The big jump in Figure 5.7(c) is due to the curvature of the car door.

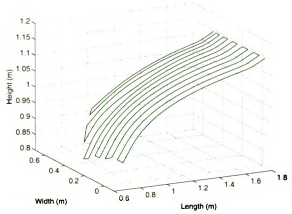

(a)

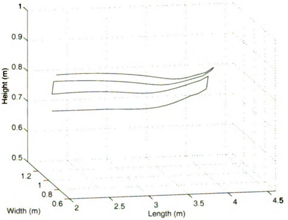

(b)

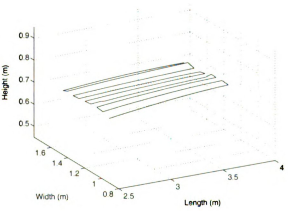

(c)

Figure 5.6: The generated paths for (a) a car hood; (b) a car fender; (c) a car door.

Table 5.2: The calculated parameters

Part	Triangles	β
hood	3320	13.1^o
fender	9355	29.7^o
door	4853	42.6^o

Table 5.3: The simulation results

Part	Average thickness $\bar{q}$ (μm)	Maximum thickness q_{max} (μm)	Minimum thickness q_{min} (μm)
hood	50.1	54.8	46.0
fender	49.1	55.0	42.6
door	49.1	55.0	35.1

The generated spray gun trajectories are also exported to $ROBCAD^{TM}$/Paint to simulate the painting process. An ABB irb6K30-75 robot is used. The work-cell setup is shown in Figure 5.8 for painting a car hood. A part of the gun path is shown in Figure 5.9. A part after painting is shown in Figure 5.10. The simulation results show that the generated trajectories can be applied to paint free-form surfaces.

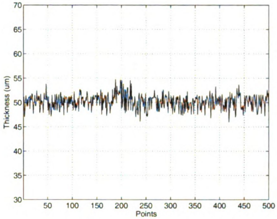

(a)

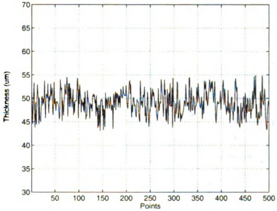

(b)

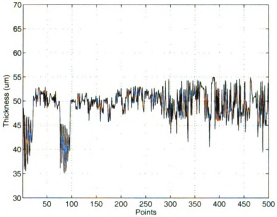

(c)

Figure 5.7: The simulation result of paint thickness for (a) a car hood; (b) a car fender; (c) a car door.

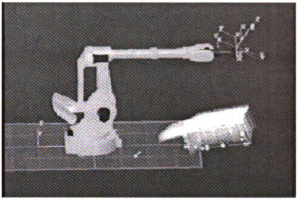

Figure 5.8: The ROBCAD simulation system.

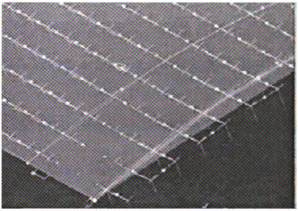

Figure 5.9: A part of a gun path.

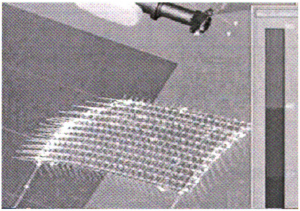

Figure 5.10: A painted part (part of a car hood).

5.2.2 Suboptimal Velocity Verification

After the trajectories are generated, the suboptimal velocity algorithm developed in Section 3.7 is applied to optimize the paint thickness. Simulations are performed only for the car fender and door since the upper and lower bounds of the car hood are quite close. Figures 5.11(a) and 5.11(b) show the simulation results for the car fender and door, respectively. Table 5.4 shows the maximum, minimum and average thicknesses for the three parts using the suboptimal velocity method. The results show that the lower bounds of the suboptimal velocity method are decreased for the car fender and door. The lower bound of the car door is $10\mu m$, instead of $15\mu m$ for the original method. That of the car fender is $4.9\mu m$, instead of $7.6\mu m$ for the original method. The thickness deviation is decreased from 30% to 20% for the car door, and 15% to 10% for the car fender, respectively. Therefore, the developed suboptimal velocity method can improve the paint thickness deviation from the required paint thickness.

Table 5.4: The simulation results using the suboptimal velocity method

Part	Average thickness $\bar{q}$ (μm)	Maximum thickness q_{max} (μm)	Minimum thickness q_{min} (μm)
fender	50.8	56.0	45.1
door	51.5	59.4	40.1

5.2.3 Comparison with Other Methods

Simulations with fixed gun direction (Case 2) are also performed to show the advantages of the developed gun direction generation method in Section 3.5.2 (Case 1). The fixed gun direction is determined using the average normals for the car hood, fender and door, respectively. The results are shown in Table 5.5.

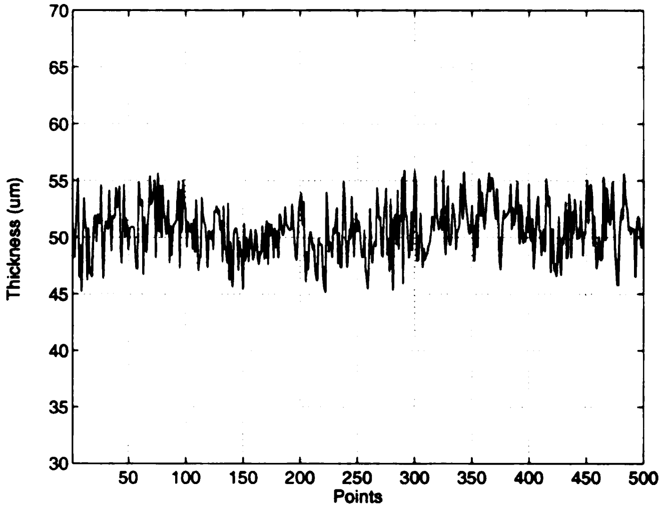

(a)

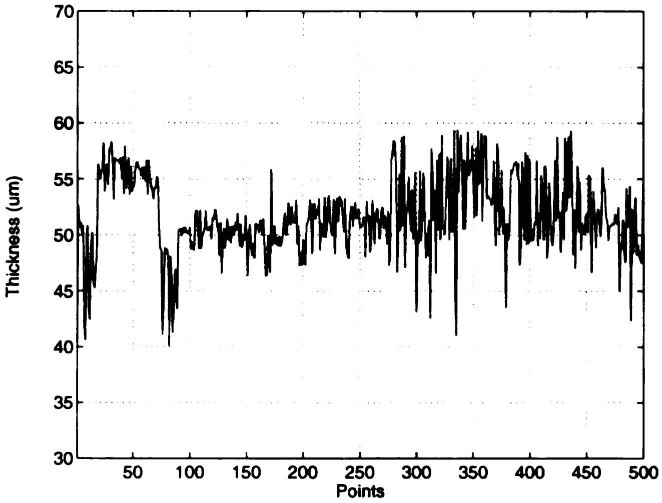

(b)

Figure 5.11: The simulation results of paint thickness using the suboptimal velocity method for (a) a car fender; (b) a car door.

The maximum deviation angle for each part in Case 1 is much smaller than that in Case 2. The deviations of the average thicknesses to the required thickness are 0.o, 0.9 and 0.6 μm for the car hood, fender and door, respectively in Case 1. However, they are 1.1, 1.8 and 2.4 μm in Case 2. The minimum thicknesses are 46.0, 42.6 and 35.6 μm for the car hood, fender and door respectively in Case 1, while 40.3,

Table 5.5: The simulation results for fixed gun directions

Part	Average thickness $\bar{q}'$ (μm)	Maximum thickness q'_{max} (μm)	Minimum thickness q'_{min} (μm)	β'
hood	48.9	54.3	40.3	32.8°
fender	48.2	54.6	35.5	42.0°
door	47.6	54.6	24.3	64.2°

35.5 and 24.3 μm for the car hood, fender and door, respectively in Case 2. As you can see, by using the suboptimal velocity method, much better results are achieved. The results show that the developed gun direction generation method achieves better paint distribution.

The thickness deviation percentage presented by Asakawa et al. [7] is more than 58%. For our results, the thickness deviation percentage is less than 20% using the suboptimal velocity method. For the car hood, much better result (8%) is achieved. Although the result presented by Suk *et al.* [41] is 20%, the over and under-painted areas are not included. Also the paint deposition rate is a constant instead of a parabolic curve.

5.3 Spray Forming

5.3.1 Trajectory Generation and Verification

Because glass fiber is sprayed on a surface in the spray forming process, area density [14] is considered instead of thickness in spray painting process. The area density is defined as the material weight on a unit area (g/m^2). If the glass fiber deposition rate is the same as the paint deposition rate in equation (5.1) with exception to the unit used, the optimized parameters are the same with exception to the unit used.

Part of a car frame is used to test the algorithm. Figure 5.12(a) shows the part; Figure 5.12(b) the generated path and Figure 5.13(a) the area density. The average, maximum and minimum area densities are 40.8, 44.5 and 36.0 g/m^2, respectively. The average area density is smaller than the required density due to the surface curvature.

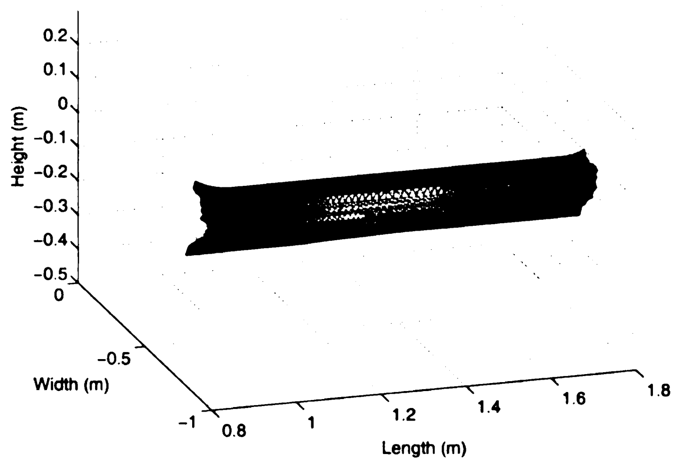

(a)

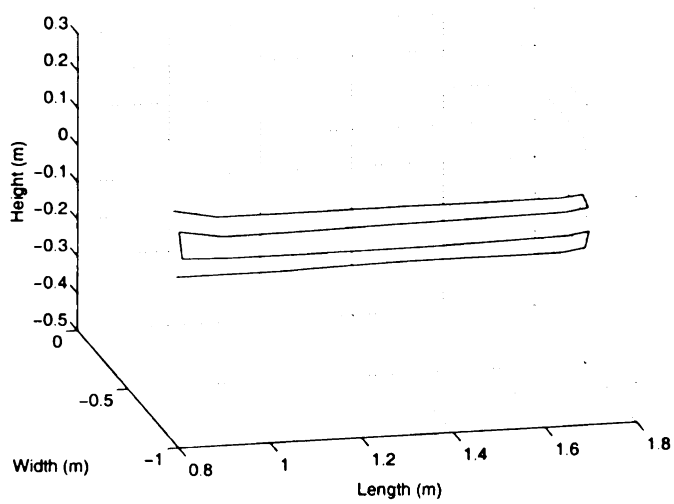

(b)

Figure 5.12: A car frame (a) CAD model; (b) The generated path.

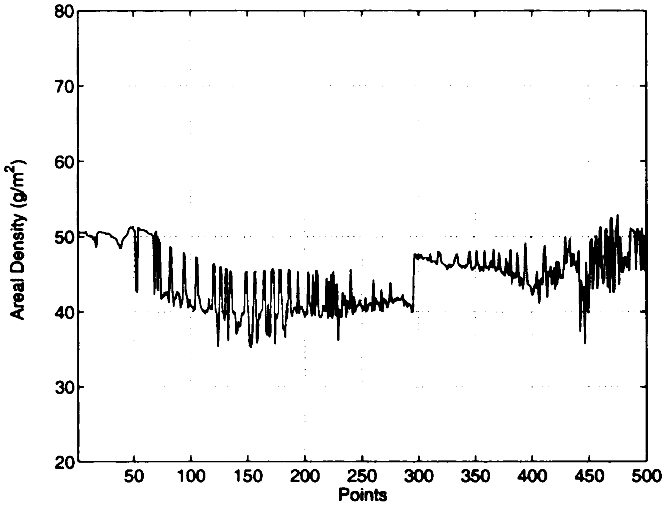

(a)

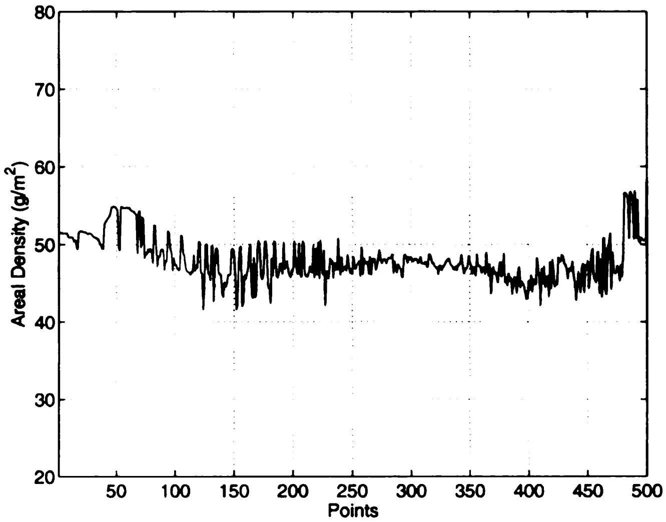

(b)

Figure 5.13: The calculated thickness of a car frame (a) without velocity optimization; (b) with suboptimal velocity.

5.3.2 Suboptimal Velocity Verification

Due to the high curvature of the surface, the average area density is smaller than the required area density. Velocity has to be optimized to increase the area density. The spray gun velocity is optimized using equation (3.36). Figure 5.13(b) shows the areal density after applying the suboptimal velocity method.

For the spray forming process using the suboptimal velocity algorithm, the average, maximum and minimum area densities are 49.9, 60.3 and 41.6 g/m^2, respectively. The average area density is 49.9 g/m^2 instead of 45.4 g/m^2 without the velocity optimization. The area density deviation decreases from 14.9 g/m^2 to 10.3 g/m^2. The results show that the suboptimal velocity algorithm indeed improves the area density deviation.

5.4 Rapid Tooling

5.4.1 Trajectory Generation and Verification

In indirect rapid tooling, a part is sprayed many times using the same trajectories. Typically, two perpendicular trajectories are used and repeated to spray a mold. Because two trajectories are used, suppose the desired metal thickness is 100 mm and the thickness deviation 30 mm. Figure 5.14 shows a mold rendered into triangles. Figures 5.15(a) and 5.15(b) show two perpendicular paths.

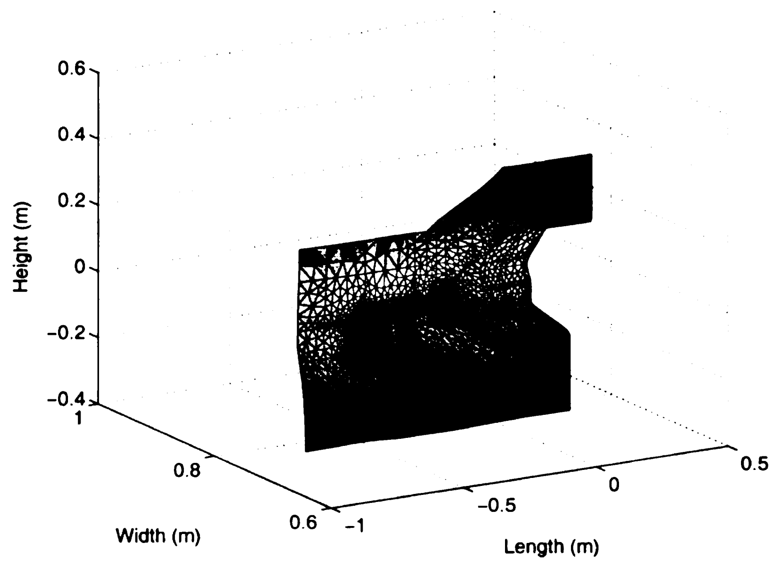

Figure 5.14: The mold for indirect rapid tooling.

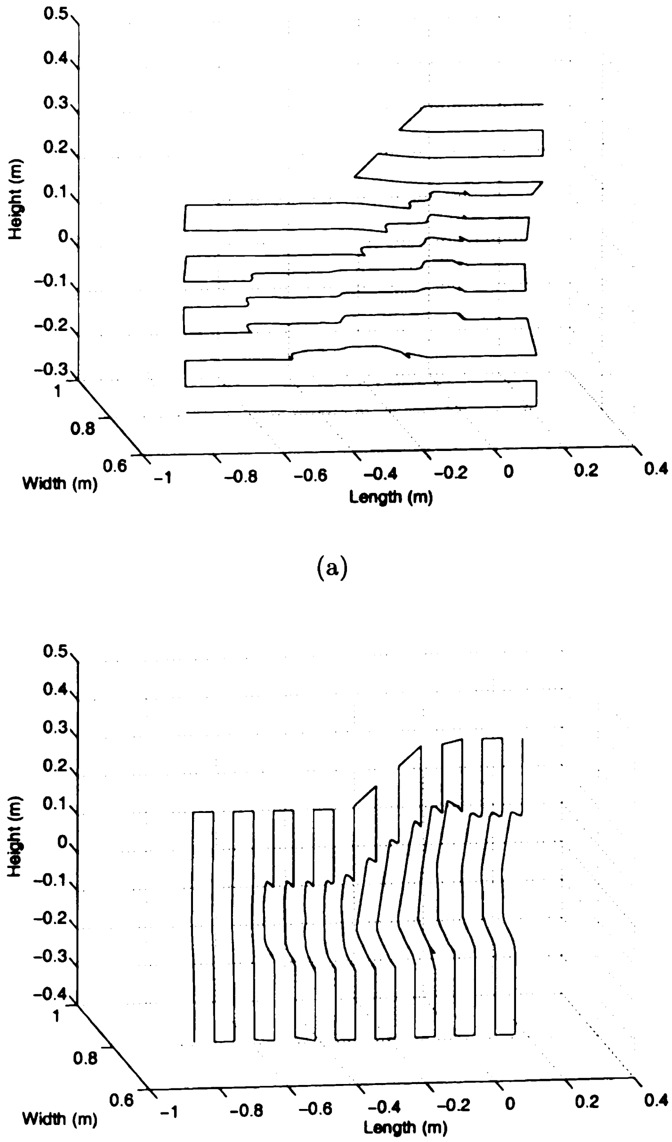

(a)

(b)

Figure 5.15: The two perpendicular paths of a mold for indirect rapid tooling.

Simulations are performed to calculate the metal distribution. The parameters used are the same as those used in spray painting with exception to the unit used. Figure 5.16(a) shows the metal thickness on the mold. The average, maximum, and minimum metal thicknesses are 93.4, 114.3 and 70.2 mm. The average metal thickness is smaller than the required metal thickness (100 mm) due to the curvature of the mold.

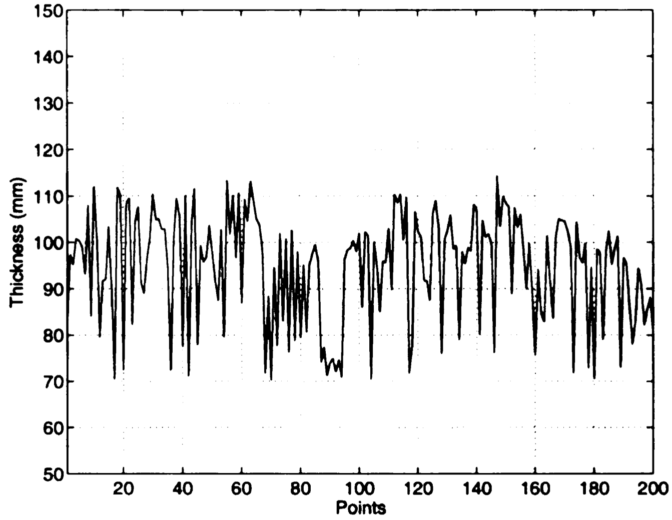

(a)

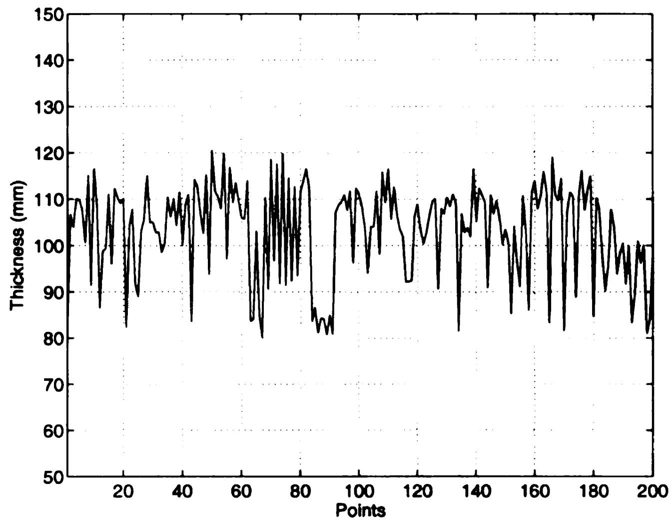

(b)

Figure 5.16: The calculated thickness for indirect rapid tooling (a) without velocity optimization; (b) with velocity optimization.

5.4.2 Suboptimal Velocity Verification

To increase the average metal thickness and decrease the metal thickness deviation, the spray gun velocity is optimized using equation (3.36). Simulations are performed using the optimized spray gun velocity. Figure 5.16(b) shows the simulation results for the indirect rapid tooling process. The average, the maximum and minimum metal thicknesses are 102.7, 80.1 and 120.4 mm, respectively. The average metal thickness is increased from 93.4 mm to 102.7 mm, which is closer to the required metal thickness (100 mm). The deviation of the metal thickness is decreased from 30% to 20%. The simulation results show the suboptimal velocity algorithm improves the material distribution on a surface for the indirect rapid tooling process.

5.5 Verification of Tool Trajectory Integration

5.5.1 Spray Painting

A part with two flat patches is generated and rendered into triangles. The angle between the two patches is 30^o. The part rendered into triangles is shown in Figure 5.17.

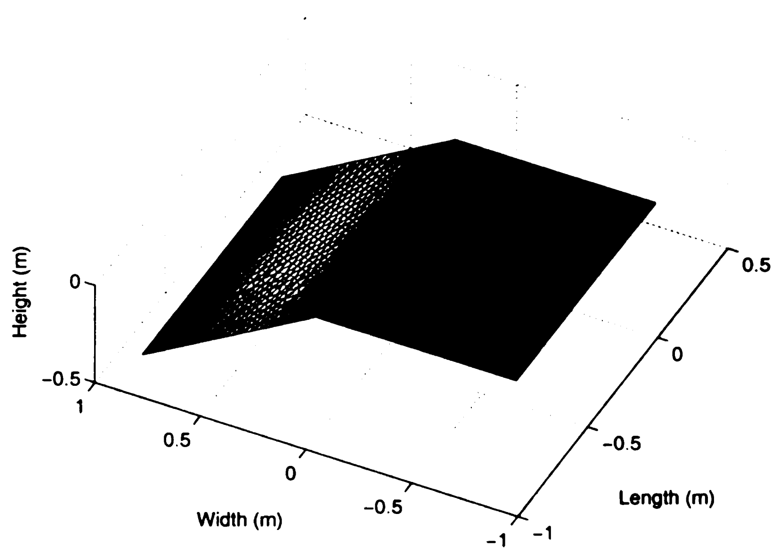

Figure 5.17: The part with two flat patches when $\alpha = 30^o$.

The paths of the part are generated for the PA-PA, PA-PE and PE-PE cases. The optimized parameters are applied to calculate the paint thickness using equation (3.34). Figure 5.18 shows the path and paint thickness for the PA-PA case; Figure

5.19 for the PA-PE case; and Figure 5.20 for the PE-PE case.

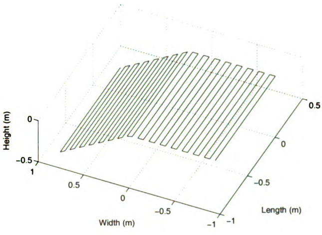

(a)

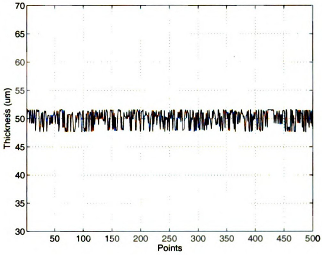

(b)

Figure 5.18: Verification results for the PA-PA case: (a) the path; (b) the paint thickness.

The maximum and minimum paint thicknesses for the three cases when $\alpha = 30^o$ are shown in Table 5.6.

The results shown in Tables 5.1 and 5.6 are quite close. This means the developed trajectory integration algorithm can optimize the paint thicknesses. The optimization

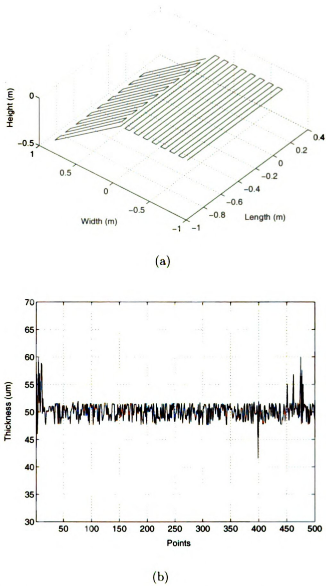

Figure 5.19: Verification results for the PA-PE case: (a) the path; (b) the paint thickness.

and verification results show that the optimized paint thickness for the PA-PA case is quite uniform; the paint thickness for the PE-PE case is uniform too. The paint thickness deviation from the required thickness is about $5\mu m$. However, the paint thickness for the PA-PE case is about $10\mu m$. Thus, the PA-PE case should be avoided in the tool trajectory planning.

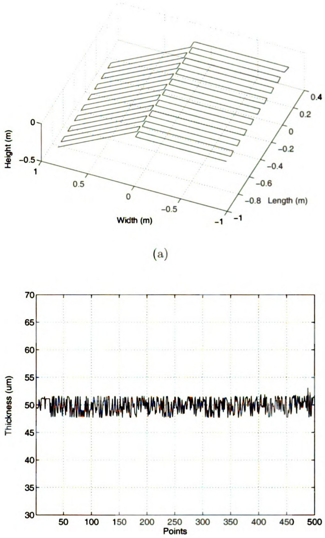

(a)

(b)

Figure 5.20: Verification results for the PE-PE case: (a) the path; (b) the paint thickness.

5.5.2 *Spray Forming*

Since area density, instead of paint thickness, is considered for spray forming, the area densities for the three paths shown in Figures 5.18, 5.19 and 5.20 are computed and shown in Figures 5.21(a), 5.21(b) and 5.21(c), respectively. The maximum, minimum and average densities are shown in Table 5.7. The area density deviations from the

Table 5.6: The simulation results

Case	Minimum thickness (μm)	Maximum thickness (μm)
PA-PA	47.6	51.6
PA-PE	41,6	59.5
PE-PE	47.5	53.0

required area density are quite small for the three cases. This means the three cases can be used in the trajectory generation for spray forming without big difference.

Table 5.7: The simulation results

Case	Average area density (g/m^2)	Minimum area density (g/m^2)	Maximum area density (g/m^2)
PA-PA	50.0	49.6	50.7
PA-PE	49.9	48.5	50.9
PE-PE	50.1	49.7	50.8

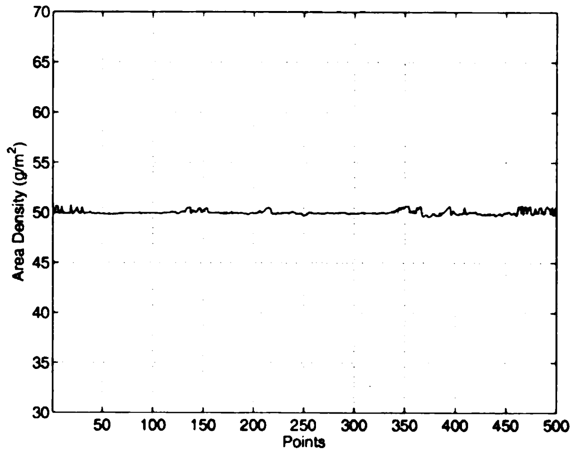

(a)

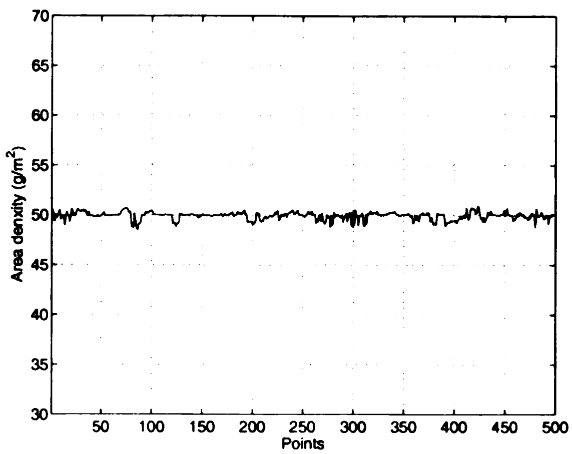

(b)

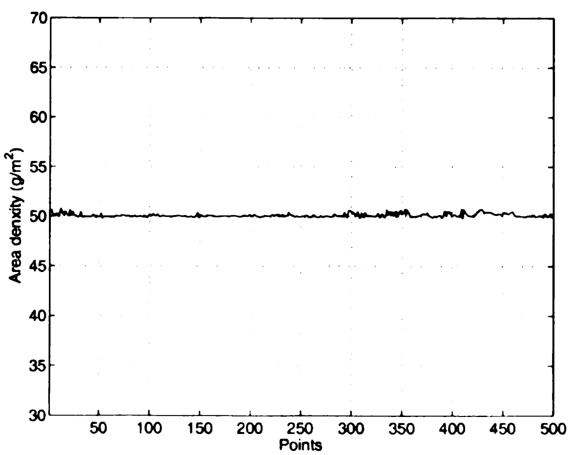

(c)

Figure 5.21: The computed area densities for (a) the PA-PA case; (b) the PA-PE case; (c) the PE-PE case.

CHAPTER 6

OPTIMAL TOOL PLANNING AND IMPLEMENTATION

This chapter discusses the optimal tool planning for constant material distribution. The algorithm for optimal tool planning is developed. A preference articulation method is discussed to control the preference of the objective functions. Simulations are performed. The simulation results of four cases are presented: optimal time, optimal material distribution, no preference articulation and preference articulation.

6.1 Optimal Tool Planning

The proposed technique for solving the optimal tool planning problem is based on approximating the optimization parameters as piecewise constants. The tool trajectories are divided into segments. Figure 6.1 shows a path with P segments. Each segment is further divided into smaller segments. It is assumed that the parameters in the smaller segments are nearly constants.

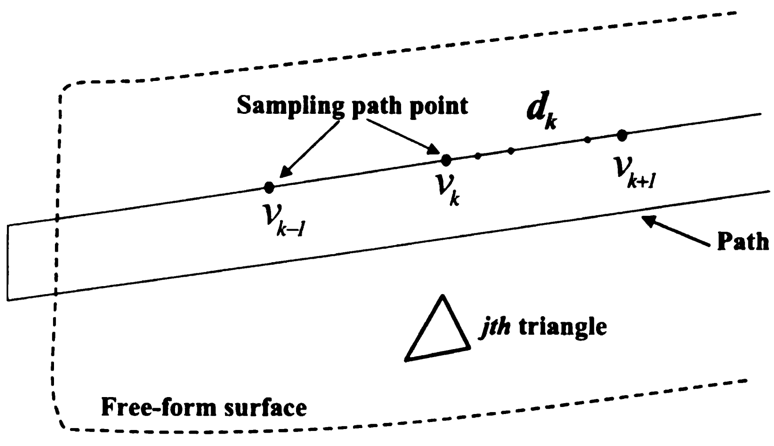

Figure 6.1: A path is divided into segments.

In the derivative of equation(3.34),

$$\frac{dq_s}{dt} = \frac{d\bar{q}}{dt}\left(\frac{h}{l_i}\right)^2 \frac{cos\gamma_i}{cos^3\theta_i} = f(r_i)\left(\frac{h}{l_i}\right)^2 \frac{cos\gamma_i}{cos^3\theta_i} \tag{6.1}$$

with

$$r_i = htan\theta_i. \tag{6.2}$$

Suppose for each smaller segment, the spray angle θ_i and deviation angle γ_i are nearly constants. Then for the jth triangle on a free-form surface, its material thickness due to the kth segment, which is divided into M_k smaller segments, can be written as:

$$q_{jk} = \sum_{i=1}^{M_k} f(htan\theta_i) \left(\frac{h}{l_i}\right)^2 \frac{cos\gamma_i}{cos^3\theta_i} \Delta t_k. \tag{6.3}$$

Therefore, the material thickness for the jth triangle is:

$$q_j = \sum_{k=1}^{P} \sum_{i=1}^{M_k} f(htan\theta_i) \left(\frac{h}{l_i}\right)^2 \frac{cos\gamma_i}{cos^3\theta_i} \frac{t_k}{M_k}. \tag{6.4}$$

This equation can be written as:

$$q_j = \sum_{k=1}^{P} \frac{d_k}{M_k v_k} \sum_{i=1}^{M_k} f(htan\theta_i) \left(\frac{h}{l_i}\right)^2 \frac{cos\gamma_i}{cos^3\theta_i}. \tag{6.5}$$

The total time to spray the free-form surface is:

$$T = \sum_{k=1}^{P} t_k = \sum_{k=1}^{P} \frac{d_k}{v_k}. \tag{6.6}$$

Then the optimal time and material thickness tool planning is formulated as:

Given the CAD model of a free-form surface and a tool model, find the minimum time to spray the surface such that the given constraints are satisfied, material thickness deviation from the desired material thickness is minimized and the maximum *material thickness deviation is minimized, i.e.,*

$$\begin{aligned}
&minJ = (J_1, J_2, J_3) \\
&subject\ to\text{: } |q_j - q_d| \leq \Delta q_d \\
&with\ q_j = \sum_{k=1}^{P} \frac{d_k}{M_k v_k} \sum_{i=1}^{M_k} f(htan\theta_i) \left(\frac{h}{l_i}\right)^2 \frac{cos\gamma_i}{cos^3\theta_i}
\end{aligned} \tag{6.7}$$

where

$$\begin{aligned}
J_1 &= \sum_{k=1}^{P} \frac{d_k}{v_k} \\
J_2 &= \sum_{j=1}^{N} (q_j - q_d)^2 \\
J_3 &= (q_{max} - q_d)^2 + (q_d - q_{min})^2
\end{aligned} \tag{6.8}$$

where N is the number of triangles in a part. This is a constrained multi-objective optimization problem. The objective functions J_1, J_2 and J_3 are conflicting with each other. According to Appendix A, $e_i(\boldsymbol{x})$ can be formulated using the given constraints, i.e.,

$$e_i(\boldsymbol{x}) = \Delta q_d - |q_j - q_d| \tag{6.9}$$

where $\boldsymbol{x}=(v_1, v_2, ..., v_P)^T$ since the velocities are the optimization parameters. Then the method in Appendix A can be applied to solve the problem.

6.2 Preference Articulation

The method to solve the optimization problem in Appendix A is a no preference articulation method. The no preference articulation method does not use any preference information. It is based on minimization of the relative distance from a candidate solution to the utopian solution. Therefore, there is no control to the preference of the objective functions. To control the preference of the objective functions, preference articulation should be used. From equation (A.3), the preference articulation is developed,

$$minF(\boldsymbol{x}) = \left[\sum_{j=1}^{k} w_j \left(\frac{f_j(\boldsymbol{x}) - f_j^*}{f_j^*}\right)^p\right]^{\frac{1}{p}}$$

subject to: $\boldsymbol{e(x)} = (e_1(\boldsymbol{x}), e_2(\boldsymbol{x}), ..., e_m(\boldsymbol{x}))^T$ with $e_i(\boldsymbol{x}) \geq 0, \ i = 1, ..., m$

$$\boldsymbol{x} = (x_1, x_2, ..., x_n)^T \tag{6.10}$$

where w_j is the weight,

$$\sum_{j=1}^{k} w_j = 1 \tag{6.11}$$

6.3 Implementation and Results

Two parts, part of a car hood and a car door, shown in Figures 2.3 and 5.5(b), respectively, are used to test the algorithm. The gun paths are shown in Figures 5.6(a) and 5.6(c) for the car hood and door, respectively. The generated tool paths have 270 and 293 sampling points for the car hood and door, respectively. Thus, there are 270 and 293 segments, respectively. Suppose the velocity in each segment is a constant, there are 270 parameters (velocities) to be optimized for the hood and 293 parameters for the door. Each segment is further divided into 10 smaller segments. The optimization processes are performed to generate optimal tool trajectories. In the implementation, the maximum velocity is set to 800 mm/s.

6.3.1 Optimal Tool Planning with Optimal Time

The optimal tool planning with optimal time is formulated as,

$$\begin{aligned}
&\min J = J_1 \\
&\text{subject to: } |q_j - q_d| \leq \Delta q_d \\
&\text{with } q_j = \sum_{k=1}^{P} \frac{d_k}{M_k v_k} \sum_{i=1}^{M_k} f(htan\theta_i) \left(\frac{h}{l_i}\right)^2 \frac{cos\gamma_i}{cos^3\theta_i}
\end{aligned} \tag{6.12}$$

The optimization for the optimal tool planning with optimal time is performed. Using the trajectory verification model (equation (3.34)), the material thicknesses on the two parts are computed and shown in Figures 6.2(a) and 6.2(b), respectively. The optimized velocities are shown in Figures 6.3(a) and 6.3(b), respectively for the two parts. The simulation results are summarized in Table 6.1. The maximum thickness errors are within the given constraints.

Table 6.1: The results for optimal tool planning with optimal time

Part	Average thickness (μm)	Minimum thickness (μm)	Maximum thickness (μm)	Spray time (s)
Hood	42.0	40.0	55.4	36.0
Door	42.1	40.0	50.1	42.1

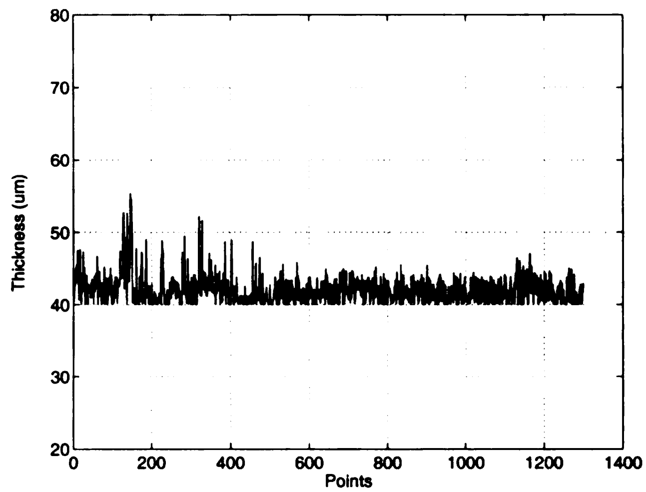

(a)

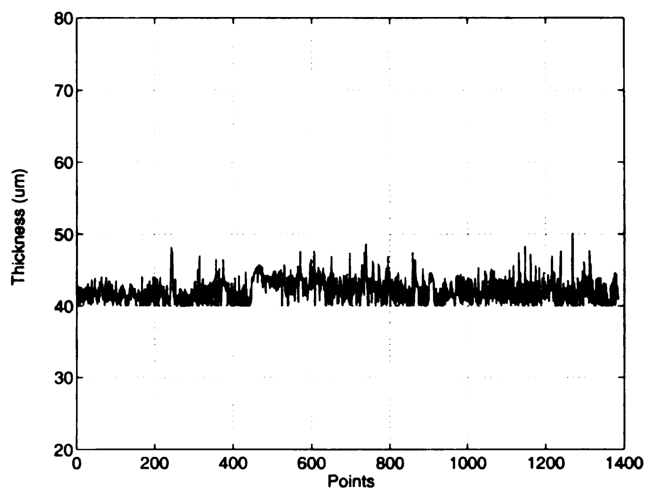

(b)

Figure 6.2: The optimized material thicknesses for the optimal tool planning with optimal time: (a) the car hood; (b) the car door.

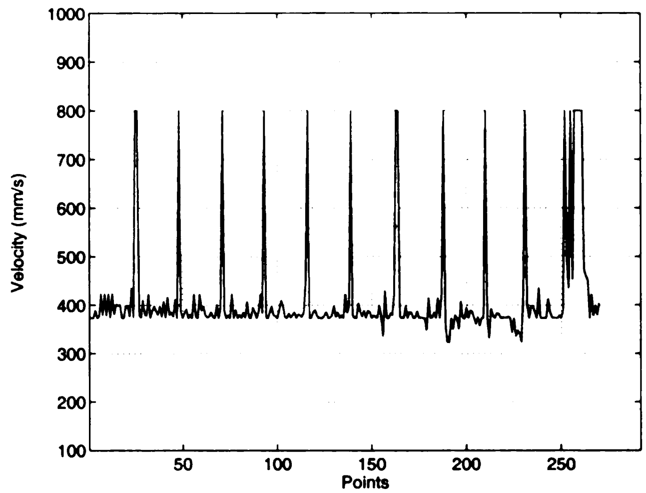

(a)

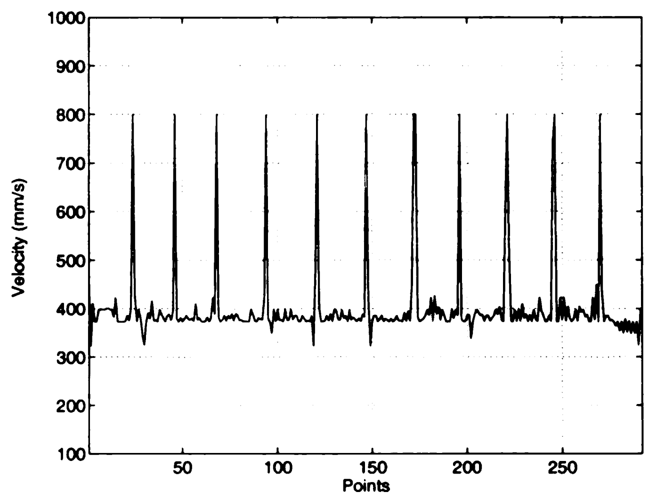

(b)

Figure 6.3: The optimized velocities for the optimal tool planning with optimal time: (a) the car hood; (b) the car door.

6.3.2 Optimal Tool Planning with Optimal Material Distribution

The optimal tool planning with optimal material distribution is formulated as,

$$\begin{aligned}
&\min J = (J_2, J_3) \\
&\text{subject to: } |q_j - q_d| \leq \Delta q_d \\
&\text{with } q_j = \sum_{k=1}^{P} \frac{d_k}{M_k v_k} \sum_{i=1}^{M_k} f(h tan\theta_i) \left(\frac{h}{l_i}\right)^2 \frac{cos\gamma_i}{cos^3\theta_i}
\end{aligned} \tag{6.13}$$

The optimization for the optimal tool planning with optimal material distribution is performed. Using the trajectory verification model (equation (3.34)), the material thicknesses on the two parts are computed and shown in Figures 6.4(a) and 6.4(b), respectively. The optimized velocities are shown in Figures 6.5(a) and 6.5(b), respectively for the two parts. The simulation results are summarized in Table 6.2. The maximum thickness errors are within the given constraints.

Table 6.2: The results for the optimal tool planning with optimal material distribution

Part	Average thickness (μm)	Minimum thickness (μm)	Maximum thickness (μm)	Spray time (s)
Hood	50.0	41.7	57.9	45.9
Door	50.0	46.3	55.4	48.4

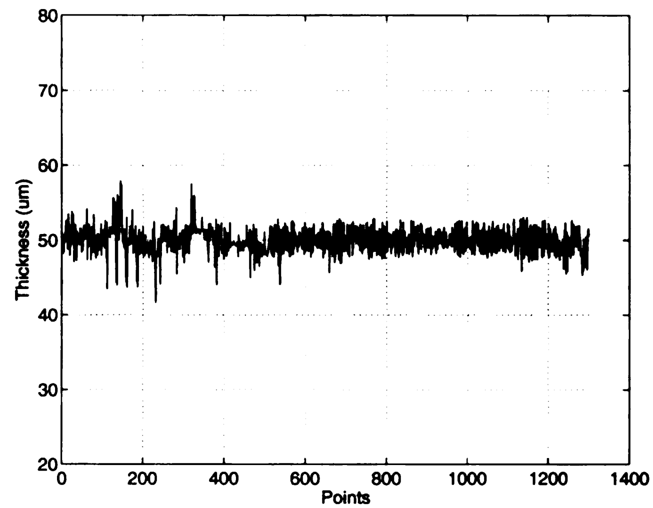

(a)

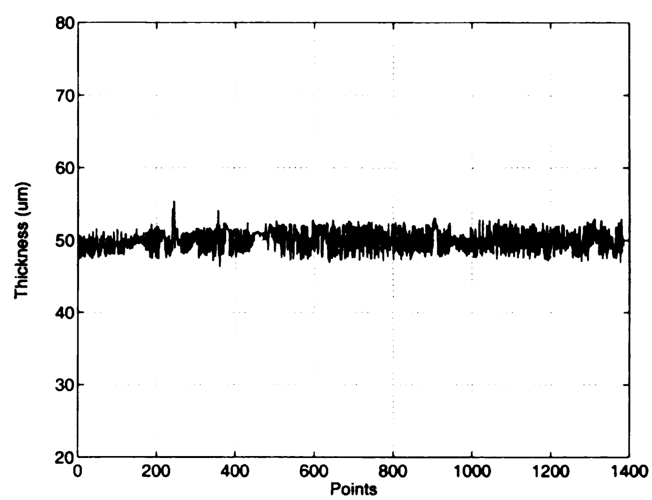

(b)

Figure 6.4: The optimized material thicknesses for the optimal tool planning with optimal material distribution: (a) the car hood; (b) the car door.

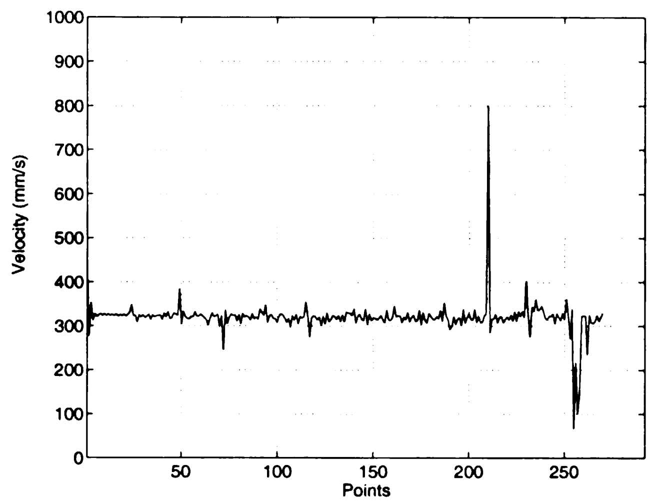

(a)

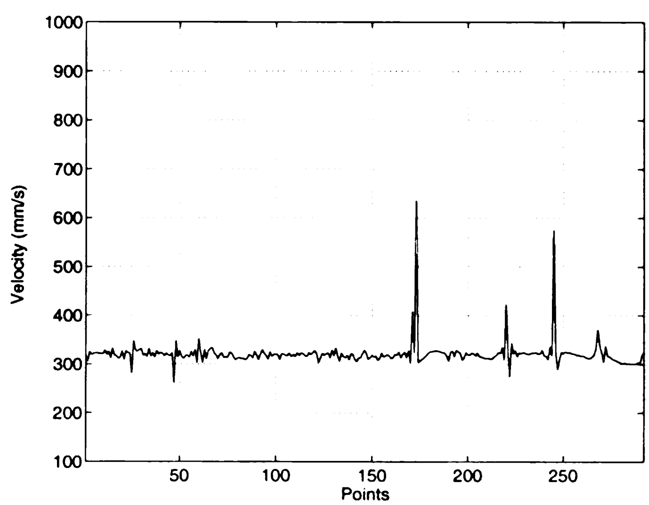

(b)

Figure 6.5: The optimized velocities for the optimal tool planning with optimal material distribution: (a) the car hood; (b) the car door.

6.3.3 Optimal Tool Planning with No Preference Articulation

The no preference articulation of optimal tool planning can be formulated using equations (6.7) and (A.4). The optimization for the optimal tool planning with no preference articulate is performed. Using the trajectory verification model (equation (3.34)), the material thicknesses on the two parts are computed and shown in Figures 6.6(a) and 6.6(b), respectively. The optimized velocities are shown in Figures 6.7(a) and 6.7(b), respectively for the two parts. The simulation results are summarized in Table 6.3. The maximum thickness errors are within the given constraints.

Table 6.3: The results for optimal tool planning with no preference articulation

Part	Average thickness (μm)	Minimum thickness (μm)	Maximum thickness (μm)	Spray time (s)
Hood	49.8	41.5	58.1	41.0
Door	49.8	45.8	55.3	46.4

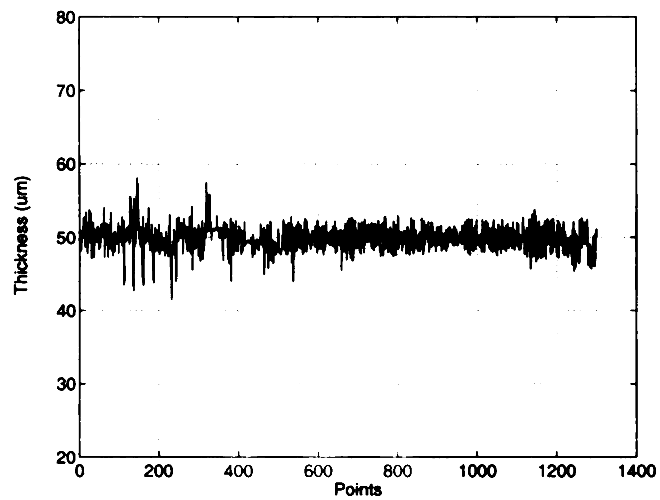

(a)

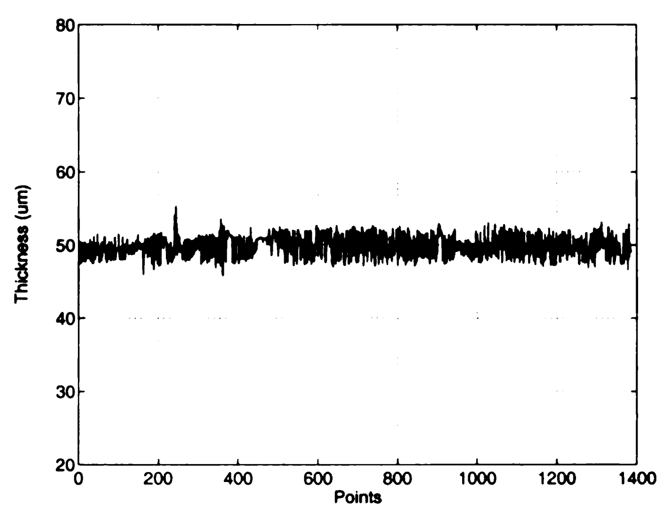

(b)

Figure 6.6: The optimized material thicknesses for the optimal tool planning with no preference articulation: (a) the car hood; (b) the car door.

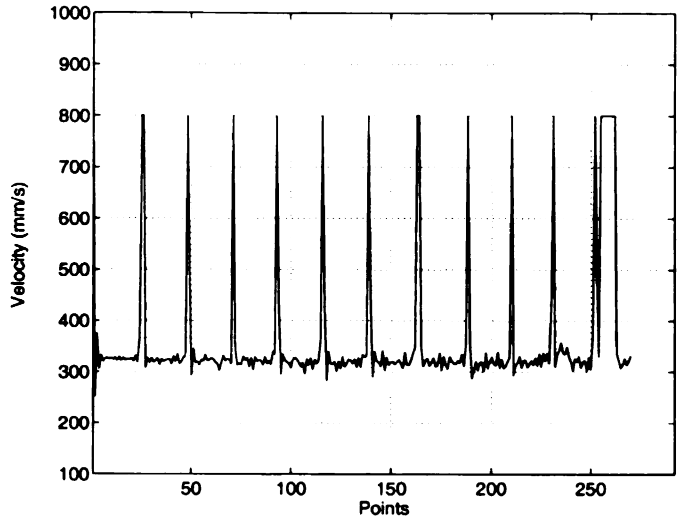

(a)

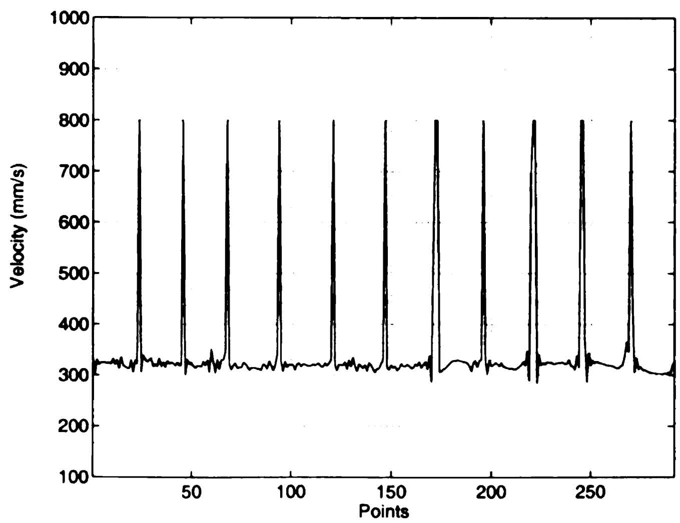

(b)

Figure 6.7: The optimized velocities for the optimal tool planning with no preference articulation: (a) the car hood; (b) the car door.

6.3.4 Optimal Tool Planning with Preference Articulation

The preference articulation of optimal tool planning can be formulated using equations (6.7) and (6.10). The optimization for the optimal tool planning with preference articulate is performed. The weights are set to:

$$w_1 = 0.8, \qquad w_2 = 0.1, \qquad w_3 = 0.1 \tag{6.14}$$

Using the trajectory verification model (equation (3.34)), the material thicknesses on the two free-form surfaces are computed and shown in Figures 6.8(a) and 6.8(b), respectively. The optimized velocities are shown in Figures 6.9(a) and 6.9(b), respectively. The simulation results are summarized in Table 6.4. The maximum thickness errors are within the given constraints.

Table 6.4: The results for optimal tool planning with preference articulation

Part	Average thickness (μm)	Minimum thickness (μm)	Maximum thickness (μm)	Spray time (s)
Hood	49.2	40.0	58.4	40.1
Door	49.3	41.1	55.4	44.9

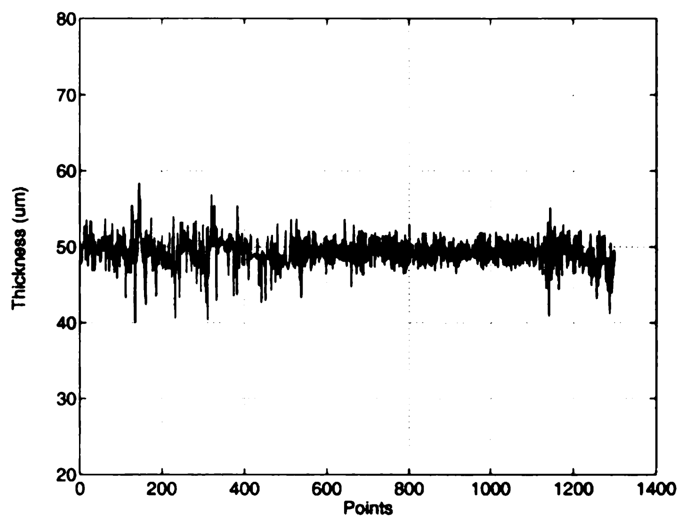

(a)

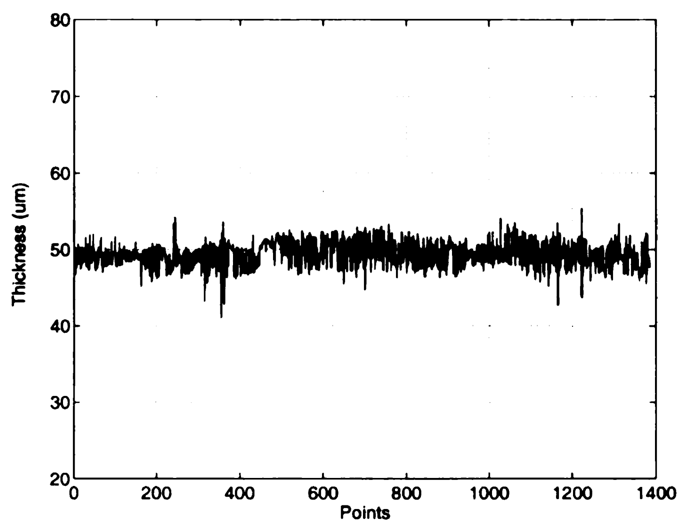

(b)

Figure 6.8: The optimized material thicknesses for the optimal tool planning with preference articulation: (a) the car hood; (b) the car door.

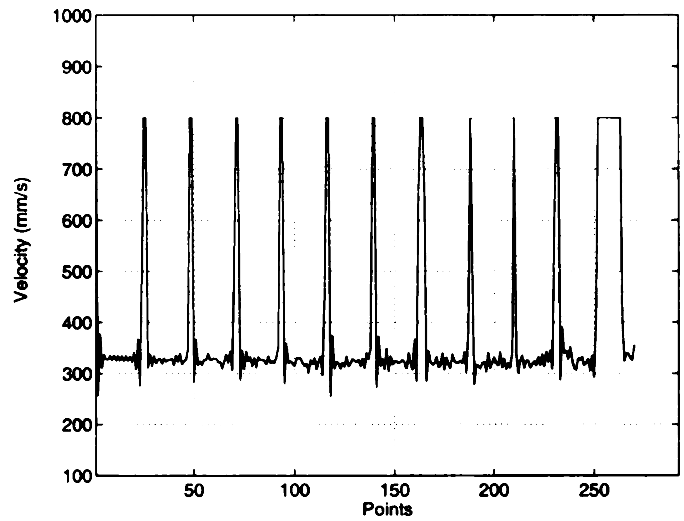

(a)

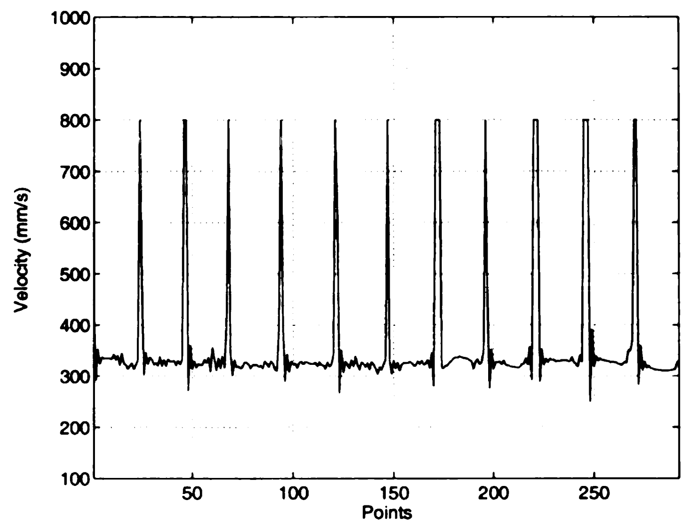

(b)

Figure 6.9: The optimized velocities for the optimal tool planning with preference articulation: (a) the car hood; (b) the car door.

6.3.5 Comparison among the Methods

The implementation results summarized in Tables 6.1, 6.2, 6.3 and 6.4 show that the maximum material thickness deviation is less than or equal to $10\mu m$ for both parts. The material distribution constraints are satisfied. The optimal tool planning with optimal time takes less time to spray a part, 36 s and 42.1 s for the car hood and door, respectively. However, the maximum material thickness deviation is about 10 μm. The optimal tool planning with optimal material distribution has the smallest material thickness deviation. However, it takes the longest time to spray the parts, 45.9 s and 48.4 s for the car hood and door respectively. For the optimal tool planning with no preference articulation and preference articulation, the average material thickness is quite close to the desired material thickness and also takes less time to spray the parts compared to the optimal tool planning with optimal material thickness and has better material distribution compared to the optimal tool planning with optimal time. With the preference set to time, the optimal tool planning with preference articulation takes less time to spray the parts compared to the optimal tool planning with no preference articulation. Therefore, the weight can be set to adjust the preference in the optimal tool planning. These results are consistent with theoretical analysis.

CHAPTER 7

OPTIMAL TOOL PLANNING FOR NON-UNIFORM MATERIAL DISTRIBUTION

This chapter discusses the optimal tool planning with non-uniform material distribution. The algorithm for optimal tool planning with non-uniform material distribution is developed. Simulations are presented. The results of optimal tool planning for four cases are presented and compared: optimal time, optimal material distribution, no preference articulation and preference articulation.

7.1 Optimal Tool Planning for Non-uniform Material Distribution

To generate a tool path for a free-form surface, the spray width has to be determined. For a non-uniform material distribution, it is challenging to obtain the spray width. Since the desired non-uniform material thickness is given, the average material thickness on a surface can be calculated:

$$\bar{q}_d = \frac{\sum_{j=1}^{N} q_{dj}(x_j, y_j, z_j(x_j, y_j))}{N}, \tag{7.1}$$

or the area-weighted average material thickness can be computed:

$$\bar{q}_d = \frac{\sum_{j=1}^{N} q_{dj}(x_j, y_j, z_j(x_j, y_j))s_j}{\sum_{j=1}^{N} s_j} \tag{7.2}$$

where $q_{dj}(x_j, y_j, z_j(x_j, y_j))$ is the material thickness at a point $(x_j, y_j, z_j(x_j, y_j))$ on a free-form surface and s_j is the area with the material thickness.

Once the average material thickness or area-weighted average material thickness is obtained, an optimization process for spraying a plane in Section 3.2 is applied to determine the spray width. After the spray width is found, an improved bounding box method in Section 3.5.1 is applied to generate a tool path for a free-form surface.

Similar to the algorithm in Chapter 6, the optimal time and material distribution deviation tool planning with non-uniform material distribution can be formulated as:

Given the CAD model of a free-form surface, a tool model, find the minimum time to spray the surface such that the given constraints are satisfied, material deviation from the desired material thickness is minimized and the maximum material thickness deviation is minimized, i.e.,

$$\begin{aligned}
&minJ = (J_1, J_2, J_3) \\
&\textit{subject to: } |q_j - q_d(x,y,z(x,y))| \leq \Delta q_d(x,y,z(x,y)) \\
&\textit{with } q_j = \sum_{k=1}^{P} \frac{d_k}{M_k v_k} \sum_{i=1}^{M_k} f(htan\theta_i) \left(\frac{h}{l_i}\right)^2 \frac{cos\gamma_i}{cos^3\theta_i}
\end{aligned} \tag{7.3}$$

where

$$\begin{aligned}
J_1 &= \sum_{k=1}^{P} \frac{d_k}{v_k}, \\
J_2 &= \sum_{j=1}^{N} (q_j - q_d(x,y,z(x,y)))^2, \\
J_3 &= (\Delta q_{max})^2.
\end{aligned} \tag{7.4}$$

Δq_{max} is the maximum material deviation.

This is a constrained multi-objective optimization problem. The objective functions J_1, J_2 and J_3 are conflicting with each other. According to Appendix A, $e_i(\boldsymbol{x})$ can be formulated using the given constraints, i.e.

$$e_i(\boldsymbol{x}) = \Delta q_d(x,y,z(x,y)) - |q_j - q_d(x,y,z(x,y))| \tag{7.5}$$

where $\boldsymbol{x}==(v_1, v_2, ..., v_P)^T$ since the velocities are the optimization parameters. Then the method in Appendix A can be applied to solve the problem.

7.2 Implementation and Results

Two parts, part of a car hood and a car door, shown in Figures 2.3 and 5.5(b), respectively, are used to test the algorithm. The gun paths are shown in Figures 5.6(a) and 5.6(c) for the car hood and door, respectively. The generated tool paths have 270 and 293 sampling points for the car hood and door, respectively. Therefore, there are 270 and 293 segments, respectively. Suppose the velocity in each segment is a constant, there are 270 parameters (velocities) to be optimized for the hood and 293 parameters for the door. Each segment is further divided into 10 smaller segments. Then the optimization processes are performed to generate optimal tool trajectories.

The desired material thickness could be any values on a free-form surface. To implement the developed algorithm, a desired material thickness is computed based on the bounding box of a part. The points on the part are projected to the bottom plane of the bounding box in Figure 3.12. The center point P_c is found. Then a non-uniform material distribution is formulated:

$$q_d(d) = 10(1 - l^2) + q_{d0} \tag{7.6}$$

where l is the distance of the projected points to P_c and q_{d0} a constant. Here, q_{d0} is set to 41.5 μm for the car hood and 42.5 μm for the door to get the average material thickness 50 μm. Figure 7.1 shows the material thicknesses on the X-Y plane for the car door and hood, respectively.

Once the desired non-uniform material thickness is determined, the average material thickness can be calculated using equation (7.1) or (7.2). Here equation (7.1) is used. The parameters used in the implementation are the same as those in Section 5.1.1. In the implementation, the maximum velocity is set to 800 mm/s.

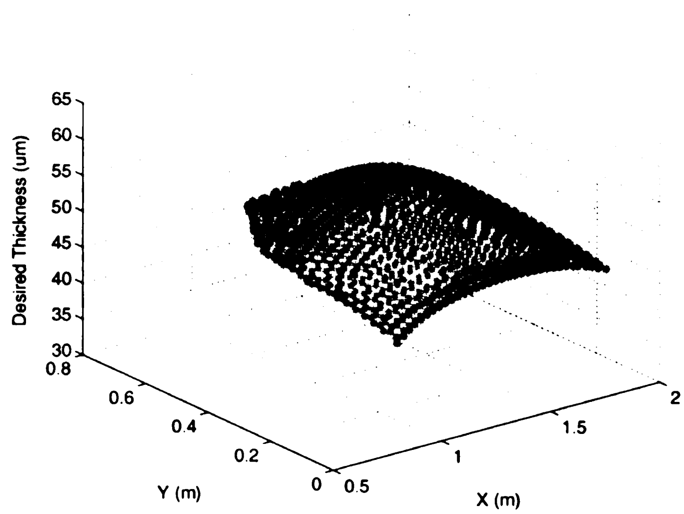

(a)

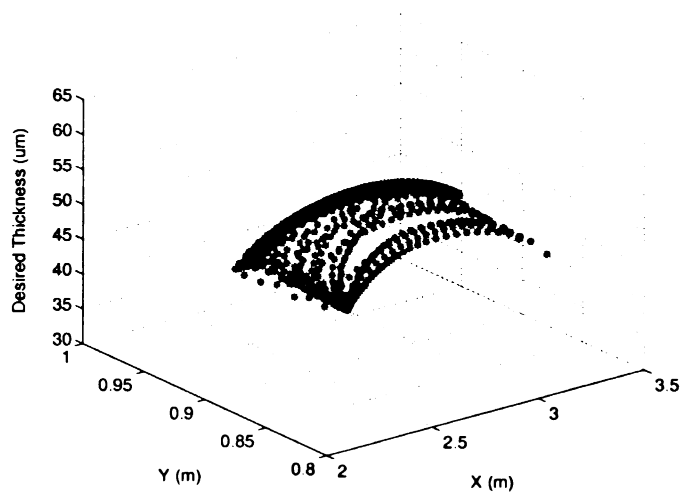

(b)

Figure 7.1: Desired non-uniform material thicknesses for: (a) a car hood; (b) a car door.

7.2.1 Optimal Tool Planning with Optimal Time

The optimal tool planning with optimal time is formulated as,

$$\begin{aligned}
&\min J = J_1 \\
&\text{subject to: } |q_j - q_d(x,y,z(x,y))| \leq \Delta q_d(x,y,z(x,y)) \\
&\text{with } q_j = \sum_{k=1}^{P} \frac{d_k}{M_k v_k} \sum_{i=1}^{M_k} f(htan\theta_i) \left(\frac{h}{l_i}\right)^2 \frac{cos\gamma_i}{cos^3\theta_i}.
\end{aligned} \tag{7.7}$$

The optimization for the optimal tool planning with optimal time is performed. Using the trajectory verification model (equation (3.34)), the material thickness on the two free-form surfaces are computed and shown in Figures 7.2(a) and 7.2(b), respectively. The optimized velocities are shown in Figures 7.3(a) and 7.3(b), respectively. The simulation results are summarized in Table 7.1. The maximum thickness errors are within the given constraints.

Table 7.1: The results for optimal tool planning with optimal time

Part	Average thickness (μm)	Maximum thickness error (μm)	Spray time (s)
Hood	42.3	10.0	35.8
Door	42.1	10.0	39.5

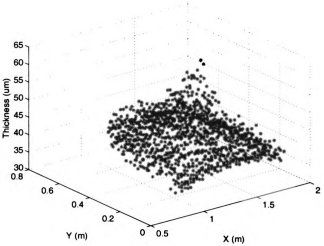

(a)

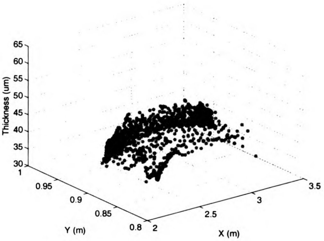

(b)

Figure 7.2: The optimized material thicknesses for the optimal tool planning with optimal time: (a) the car hood; (b) the car door.

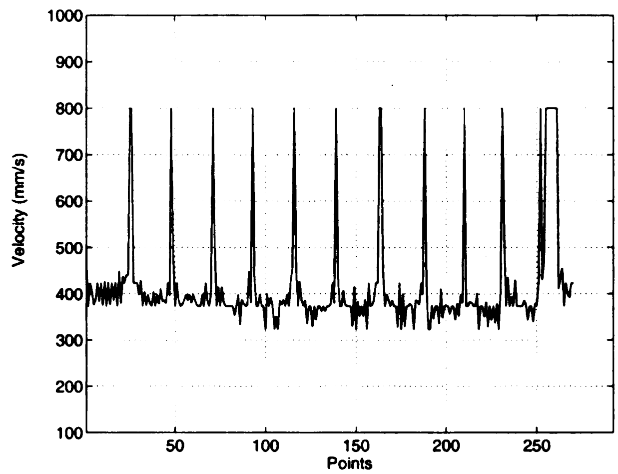

(a)

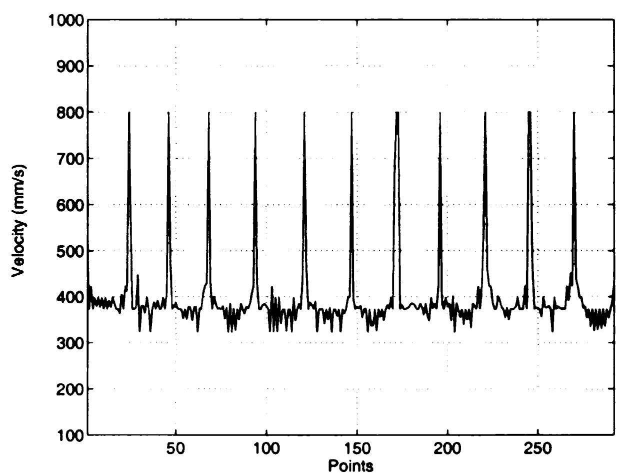

(b)

Figure 7.3: The optimized velocities for the optimal tool planning with optimal time: (a) the car hood; (b) the car door.

7.2.2 Optimal Tool Planning with Optimal Material Distribution

The optimal tool planning with optimal material distribution is formulated as,

$$\begin{aligned}
&\min J = (J2, J3) \\
&\text{subject to: } |q_j - q_d(x, y, z(x, y))| \leq \Delta q_d(x, y, z(x, y)) \\
&\text{with } q_j = \sum_{k=1}^{P} \frac{d_k}{M_k v_k} \sum_{i=1}^{M_k} f(htan\theta_i) \left(\frac{h}{l_i}\right)^2 \frac{cos\gamma_i}{cos^3\theta_i}.
\end{aligned} \tag{7.8}$$

The optimization for the optimal tool planning with optimal material distribution is performed. Using the trajectory verification model (equation (3.34)), the material thicknesses on the two parts are computed and shown in Figures 7.4(a) and 7.4(b), respectively. The optimized velocities are shown in Figures 7.5(a) and 7.5(b), respectively for the two parts. The simulation results are summarized in Table 7.2. The maximum thickness errors are within the given constraints.

Table 7.2: The results for the optimal tool planning with optimal material distribution

Part	Average thickness (μm)	Maximum thickness error (μm)	Spray time (s)
Hood	50.0	8.1	45.6
Door	49.8	5.1	46.6

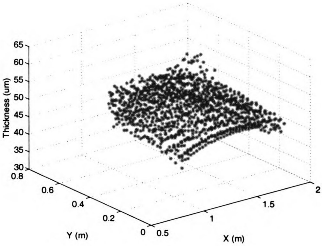

(a)

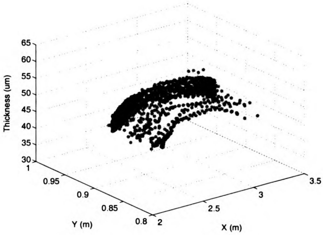

(b)

Figure 7.4: The optimized material thicknesses for the optimal tool planning with optimal material distribution: (a) the car hood; (b) the car door.

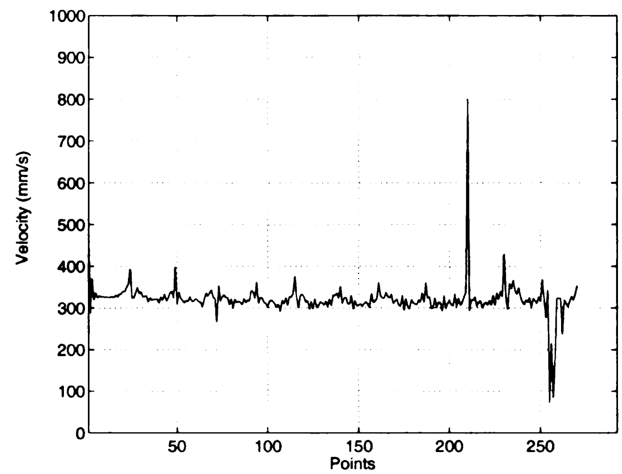

(a)

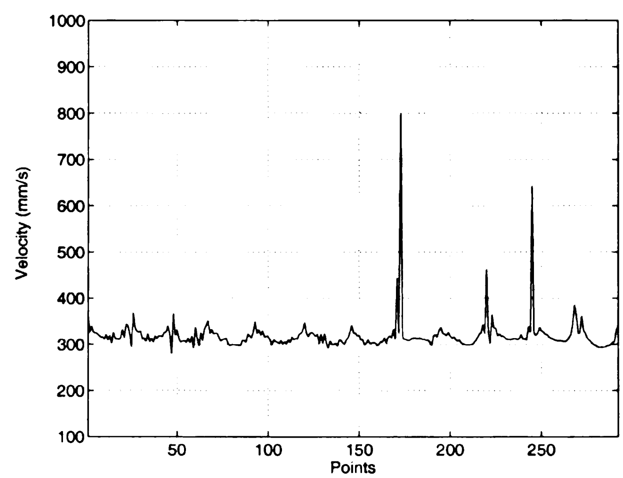

(b)

Figure 7.5: The optimized velocities for the optimal tool planning with optimal material distribution: (a) the car hood; (b) the car door.

7.2.3 Optimal Tool Planning with No Preference Articulation

The no preference articulation of optimal tool planning can be formulated using equations (7.3) and (A.4). The optimization for the optimal tool planning with no preference articulation is performed. Using the trajectory verification model (equation (3.34)), the material thicknesses on the two parts are computed and shown in Figures 7.6(a) and 7.6(b), respectively. The optimized velocities are shown in Figures 7.7(a) and 7.7(b), respectively. The simulation results are summarized in Table 7.3. The maximum and the minimum thickness errors are within the given constraints.

Table 7.3: The results for the optimal tool planning with no preference articulation

Part	Average thickness (μm)	Maximum thickness error (μm)	Spray time (s)
Hood	49.9	8.2	41.7
Door	49.3	8.9	44.9

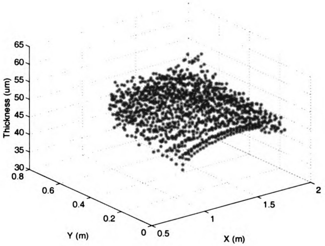

(a)

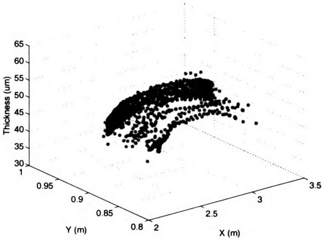

(b)

Figure 7.6: The optimized material thicknesses for the optimal tool planning with no preference articulation: (a) the car hood; (b) the car door.

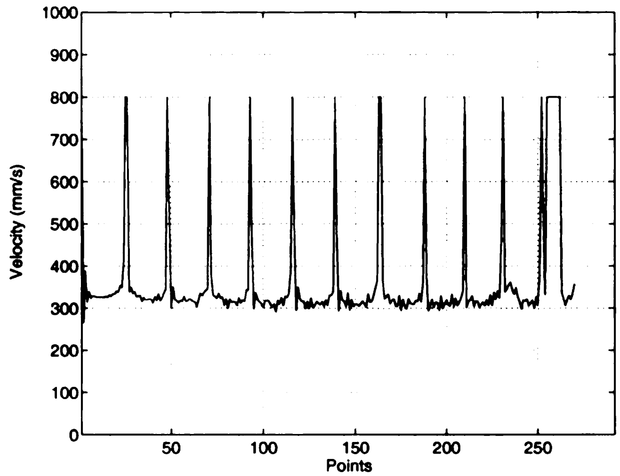

(a)

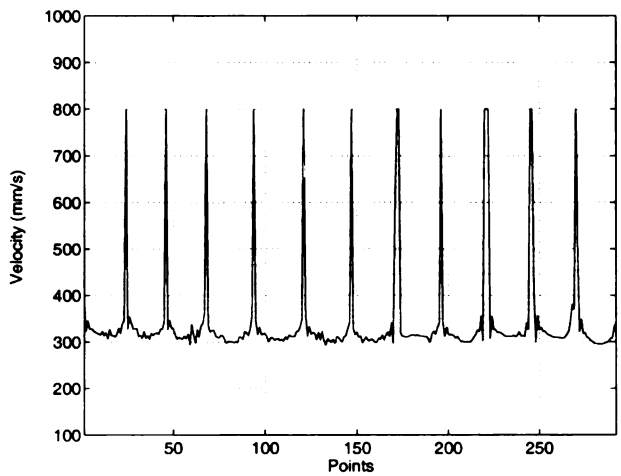

(b)

Figure 7.7: The optimized velocities for the optimal tool planning with no preference articulation: (a) the car hood; (b) the car door.

7.2.4 *Optimal Tool Planning with Preference Articulation*

The preference articulation of optimal tool planning can be formulated using equations (7.3) and (6.10). The optimization for the optimal tool planning with preference articulate is performed. The weights are set to:

$$w_1 = 0.8, \qquad w_2 = 0.1, \qquad w_3 = 0.1. \tag{7.9}$$

Using the trajectory verification model (equation (3.34)), the material thicknesses on the two parts are computed and shown in Figures 7.8(a) and 7.8(b), respectively. The optimized velocities are shown in Figures 7.9(a) and 7.9(b), respectively. The simulation results are summarized in Table 7.4. The maximum and the minimum thickness errors are within the given constraints.

Table 7.4: The results for the optimal tool planning with preference articulation

Part	Average thickness (μm)	Maximum thickness error (μm)	Spray time (s)
Hood	49.2	10.0	40.0
Door	49.0	10.0	44.5

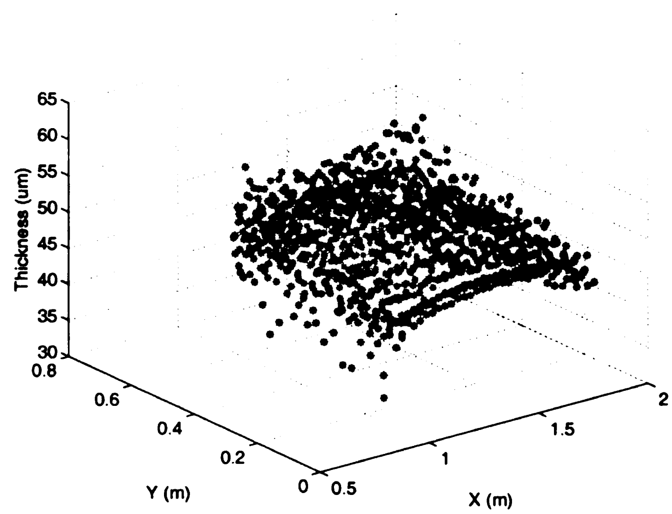

(a)

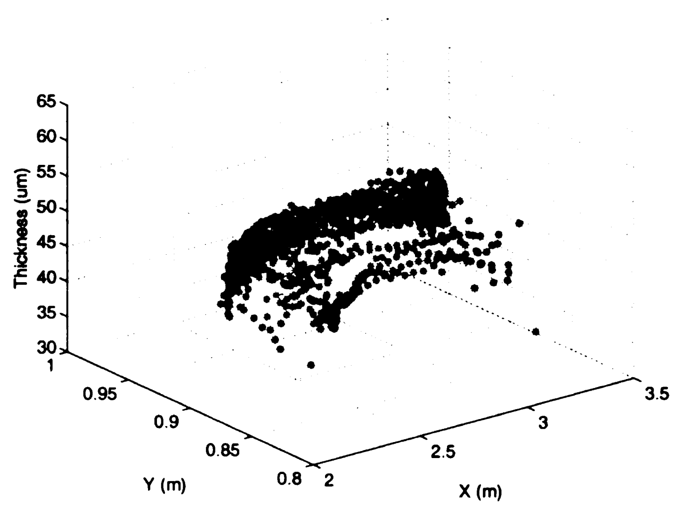

(b)

Figure 7.8: The optimized material thicknesses for the optimal tool planning with preference articulation: (a) the car hood; (b) the car door.

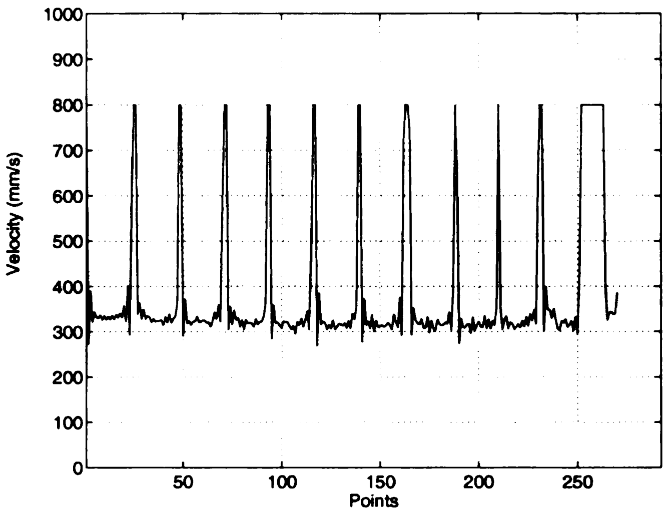

(a)

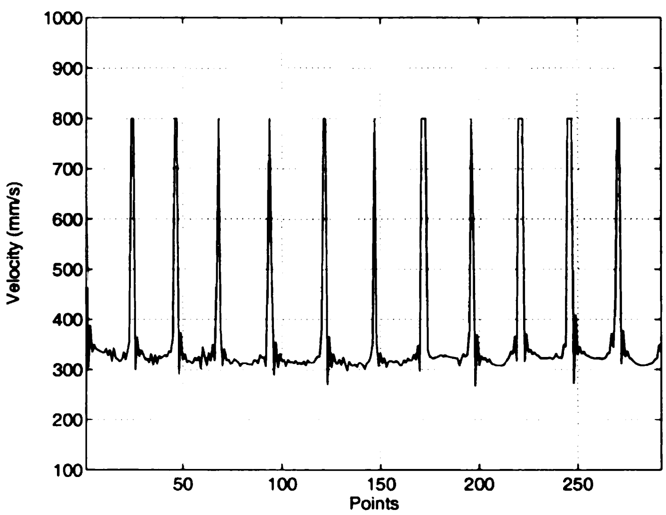

(b)

Figure 7.9: The optimized velocities for the optimal tool planning with preference articulation: (a) the car hood; (b) the car door.

7.2.5 Comparison among the Methods

The implementation results summarized in Tables 7.1, 7.2, 7.3 and 7.4 show that the maximum material thickness deviation is less than or equal to $10\mu m$ for both parts. The material distribution constraints are satisfied. The optimal tool planning with optimal time takes less time to spray a part, 35.8 s and 39.5 s for the car hood and door, respectively. However, the average material thickness deviation is about 10 μm. The optimal tool planning with optimal material distribution has the smallest material thickness deviation. But it takes the longest time to spray the parts, 45.6 s and 46.6 s for the car hood and door, respectively. For the optimal tool planning with no preference articulation and preference articulation, the average material thickness is close to the desired material thickness and also takes less time to spray the parts compared to the optimal tool planning with optimal material distribution and has better material distribution compared to the optimal tool planning with optimal time. With the preference set to time, the optimal tool planning with preference articulation takes less time to spray a part compared to the optimal tool planning with no preference articulation. Therefore, the weights can be set to satisfy the needs in optimal tool planning. These results are consistent with theoretical analysis.

CHAPTER 8

EXTENSIONS OF THE GENERAL FRAMEWORK

The developed general framework can also be extended to other applications. This chapter presents the extensions of the general framework to dimensional inspection and nanomanufacturing.

8.1 Extension to Dimensional Inspection in Manufacturing

Dimensional inspection is an important process in manufacturing industry. Quality and process control activities require that parts be measured, or dimensionally inspected [42]. Inspection generally is time-consuming, which has been creating serious bottlenecks in production lines [43]. Active optical inspection techniques have been developed and greatly reduces the time in dimensional inspection. Structured light, which obtains $3D$ coordinates by projecting specific light patterns on the surface of an object, is one of the active methods and it has been successfully implemented in various applications [44]. However, to achieve full automation and improve the efficiency of the inspection system, sensor planning, or finding the suitable configurations of sensors is very important so that the inspection task can be carried out satisfactorily. It is, therefore, highly desirable to develop a camera positioning system that is able to plan and realize the camera configurations in a fully-automated, accurate and efficient way. The general framework (Section 2.1) can be applied to generate a camera path for the dimensional inspection of a part. Sheng [28] developed a CAD-guided robot motion planning system for dimensional inspection in manufacturing. The system is one of the extensions of the general framework.

8.2 Extension to Nanomanufacturing

8.2.1 Introduction

Nanotechnology, a promising advanced technology for the forthcoming century, has been a recent hot research topic. The development of nanomanufacturing technologies will lead to potential breakthroughs in manufacturing of new industrial products. Nanoscale products with unique mechanical, electronic, magnetic, optical and/or chemical properties, open the door to an enormous new domain of nanostructures and integrated nanodevices. They have a variety of potential applications such as nanoelectromechanical systems (NEMS) and DNA computers etc. Nanomanufacturing requires positioning of nanoparticles in complex 2D or 3D structures. The techniques for nanomanufacturing can be classified into "bottom-up" and "top-down" methods.

Self-assembly in nanoscale is a promising "bottom-up" technique which is applied to make regular, symmetric patterns of nanoparticles [45]. However, many potential nanostructures and nanodevices are asymmetric patterns, which cannot be manufactured using self-assembly.

A "top-down" method is desirable to fabricate complex nanostructures. Atomic force microscopy [46] has been proven to be a powerful technique to study sample surfaces down to the nanometer scale. Not only can it characterize sample surfaces, but it can also change the sample surface through manipulation [47, 48], which is a promising "top-down" nanofabrication technique. In recent years, many kinds of nanomanipulation schemes have been developed [49, 50, 51] to position and manipulate nanostructures. The main problem of these manipulation schemes is that they go through the scan-design-manipulation-scan cycle manually, which is time consuming and makes mass production impossible. Recently, some researchers have been trying to combine an atomic force microscope (AFM) with haptic techniques and a virtual reality interface to facilitate nanomanipulation [52, 53]. Although virtual reality, which can display a static virtual environment and a dynamic tip position, has been constructed, it does not display any environment changing due to manipulation. Therefore operators are still blind because they cannot see the environment changing in real-time. The manual manipulation of nanoparticles also reduces the manipulation speed.

The complexity of nanomanufacturing requires positioning, manipulating and assembling nanoparticles to form a given pattern. Typical manual nanomanipulation is complex and time-consuming. Also, the paths are obtained in an interactive way between the users and the AFM images, which is inefficient. In order to increase efficiency in nanomanufacturing, automated manipulation using collision-free paths is necessary because particles are randomly distributed on a surface. Automated path planning is crucial to manufacture nanostructures and nanodevices. However, automated tool path planning for nanomanufacturing does not receive much attention. Makaliwe [54] developed a path planning algorithm for nanoparticle assembly. Object assignment, obstacle detection and avoidance, path finding and sequencing are addressed. The obstacles discussed in the paper are polygons, which do not occur often in nanoworld. Also the collision of nanoparticles during nanomanipulation is not discussed. In AFM manipulation, indirect path around obstacles should be avoided since manipulation using indirect path may lose nanoparticles. Therefore, direct path is desirable for nanomanipulation. To generate a path for nanomanufacturing, obstacle avoidance has to be considered. A combination of both theoretical (analytical and computational) and experimental methodologies is appropriate to address the underlying necessities for nanomanufacturing. The developed general framework (Section 2.1) can be applied for the tool path generation in nanomanufacturing.

8.2.2 Automated Nanomanipulation System

An automated nanomanipulation system has been developed to manipulate nanoparticles to manufacture nanodevices and nanostructures automatically. Figure 8.1 shows the automated nanomanipulation sytem.

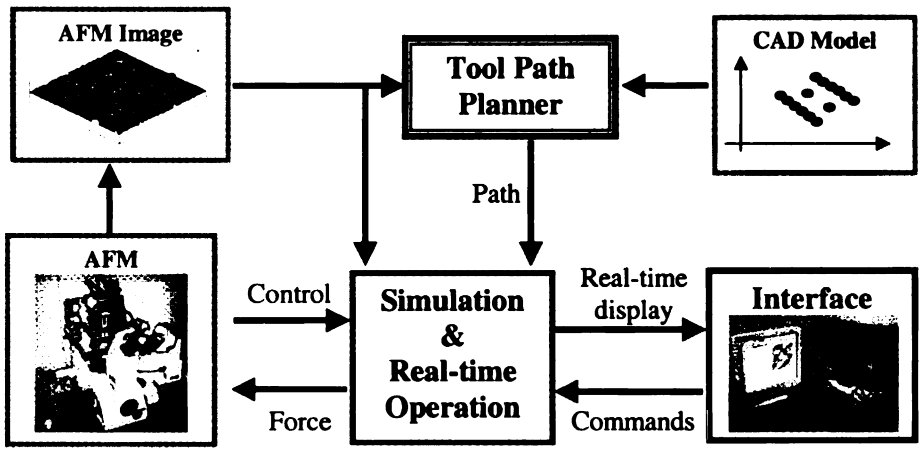

Figure 8.1: A general framework for nanomanufacturing.

Based on the CAD model of a nanopart and an AFM image of a surface with nanoparticles, a collision-free path is generated to manufacture the nanopart. After the path is generated, it is input to a nanomanipulation system assisted by augmented reality to perform the actual manufacturing process.

During nanomanipulation, it is desirable for the operator to observe the real-time changes of the nano-environment. Previous nanomanipulation using AFM has been blind work. Each operation is designed off-line based on a static AFM image and then downloaded to the AFM system to visualize the operation in open loop. Whether the operation is successful or not has to be verified by a new image scan. Obviously, this scan-design-manipulation-scan cycle is very time-consuming because it usually takes several minutes to obtain a new AFM image. Therefore, an augmented reality system [55] has been developed to provide operators with real-time visual display. The real-time visual display is a dynamic AFM image of the operating environment which is locally updated based on real-time force information. Here the augmented reality system is adopted to perform the nanomanufacturing process.

8.2.3 A General Framework

A general framework for the path planning is to find a path based on the CAD model of a 2D part and an AFM image of particles. Path planning is to plan the tip position and orientation of an AFM. A general framework of automated CAD-guided path planning for nanomanufacturing can be formulated as follows:

Given the CAD model of a 2D nanopart M and an AFM image of a surface Ω, find a path Γ such that the nanopart can be manufactured using an AFM, i.e.,

$$F(M, \Omega) = \Gamma. \tag{8.1}$$

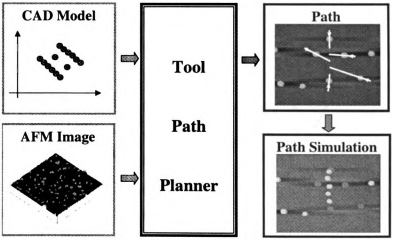

Figure 8.2: A general framework for the automated CAD-guided path planning system.

Figure 8.2 is the illustration of the general framework. Based on the CAD model of a 2D part and the AFM image, the path planner generates a path automatically to manufacture the part. The path is input to a simulation software to verify if the path can manufacture the part without any collisions. Finally, the path is implemented to manufacture a nanodevice or nanostructure.

The tool path planner is the core of the general framework. Figure 8.3 shows the steps for the tip path planner. Based on the CAD model of a nanopart and an AFM

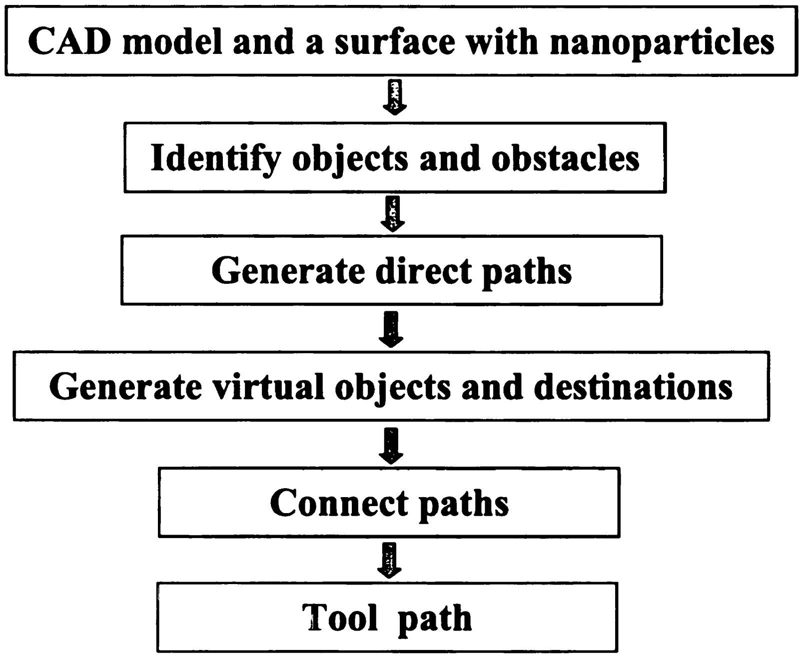

Figure 8.3: Tip path planner.

image of a surface with particles, objects and obstacles are identified. After that, direct paths are generated. Then, virtual objects and destinations are generated to avoid obstacles. Paths are connected to form an AFM tip path.

CAD Model

Since nanoparticles are manipulated to manufacture nanostructures or nanodevices, a part has to be designed using the nanoparticles. Based on the average size of nanoparticles, nanostructures and nanodevices are designed. Figure 8.4 shows a designed nanostructure.

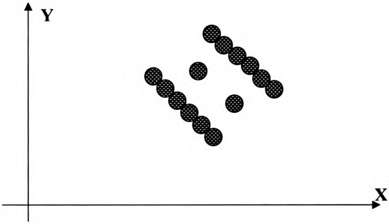

Figure 8.4: A designed nanopart.

Object and Obstacle Identification

An image of a surface with nanoparticles can be obtained using an AFM in the tapping mode. The data of the XY coordinates and height of each pixel are saved to a data file. Figure 8.5 shows the raw data from an AFM.

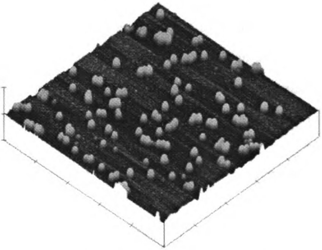

Figure 8.5: The raw data from an AFM.

Since the surface is not completely flat, a threshold height value is set for particle identification. If the height of a pixel is larger than the threshold, it is considered as an element of a particle. The particles can then be identified and the size of each particle can be determined. If the size of a particle is too large, it is difficult for the

AFM tip to manipulate it. If the size of a particle is too small, it is better not to be used as a component of a nanostructure since it may cause gaps between components. Therefore, the size of a particle must be in a certain range to be considered as an object, which is good for manufacturing nanodevices or nanostructures; otherwise, it is an obstacle, i.e.,

$$\text{Particle} = \begin{cases} \text{Obstacle} & S_p \leq \alpha_1 \text{ or } S_p \geq \alpha_2 \\ \text{Object} & \alpha_1 < S_p < \alpha_2 \end{cases} . \tag{8.2}$$

8.2.4 Automated Tool Path Planning

Once the destinations, objects and obstacles are determined, a collision-free path can be generated to manufacture a nanostructure or nanodevice.

Direct Path

A direct path is a connection between an object and an obstacle using a straight line. After the objects and obstacles are identified, each object is connected with each destination using a straight line. Figure 8.6 shows the connection. The path between O2 and D2 is a direct path; the path between O1 and D1 is not a direct path due to collision.

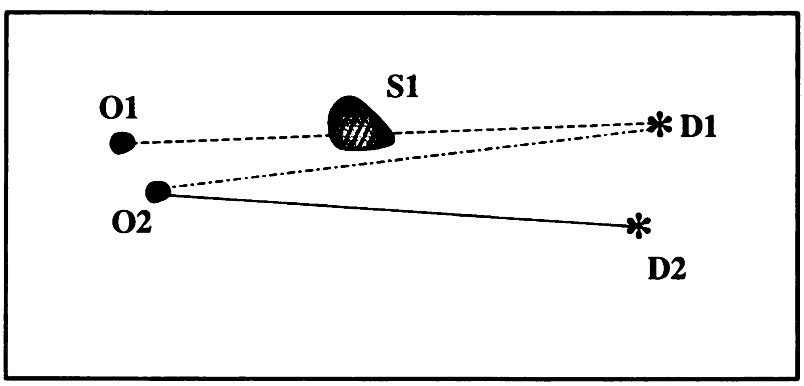

Figure 8.6: The straight line connection between an object and an destination. O1 and O2 are objects; D1 and D2 destinations; S1 is an obstacle.

Due to the van der Waals force between an object and an obstacle, the object maybe attracted to the obstacle if the distance between the object and the obstacle is too small. Therefore, the minimum distance has to be determined first to avoid the attraction. Figure 8.7 shows an object and an obstacle.

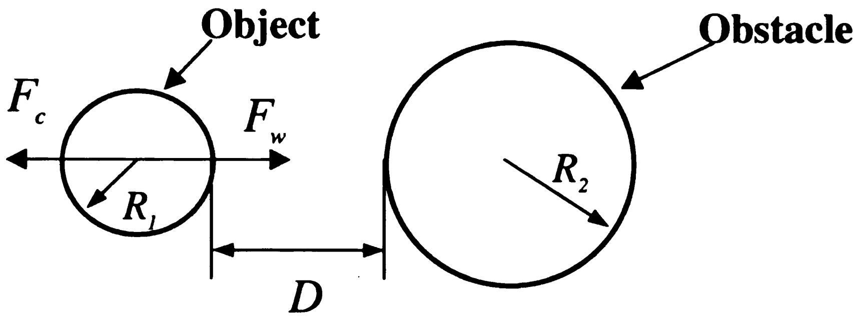

Figure 8.7: The van der Waals force between an object and an obstacle. R_1 and R_2 are the radius of the two spheres, respectively; D is the distance between the two spheres; F_w van der Waals force; F_c the friction force.

Suppose all objects and obstacles are spheres, then the van der Waals force can be expressed as [56]:

$$F_W = \frac{-A}{6D}\frac{R_1 R_2}{R_1 + R_2} \tag{8.3}$$

where F_W is the van der Waals force; A the Hamaker constant; D the distance between the two spheres; R_1 and R_2 are the radius of the two spheres. Different materials have different Hamaker constants. Nevertheless, the hamaker constants are found to lie in the range $(0.4 - 4)10^{-19}\ J$. If an object is not attracted to an obstacle, the van der Waals force has to be balanced by the friction force as shown in Figure 8.7. The friction force is caused by the repulsive and adhesive forces and can be formulated as [57]:

$$F_c = \mu_{os} F^r_{os} + \nu F^a_{os} \tag{8.4}$$

where F_c is the friction force; μ_{os} the sliding friction coefficient between an object and the substrate surface; ν the shear coefficient; F^r_{os} the repulsive force and F^a_{os} the adhesive force. When pushing an object, the repulsive force equals to 0. Then equation (8.4) becomes

$$F_c = \nu F_{os}^a. \tag{8.5}$$

The adhesive force F_{os}^a can be obtained using the tip adhesive force F_{ts}^a, which can be measured [57]:

$$F_{os}^a = \frac{A_{os}}{A_{ts}} F_{ts}^a \tag{8.6}$$

where A_{os} is the nominal contact area between an object and a substrate surface; A_{ts} the nominal contact area between the AFM tip and the substrate surface.

Since the van der Waals force has to be balanced by the friction force during manipulation, the minimum distance D_{min} can be calculated using equations (8.3, 8.5, 8.6):

$$D_{min} = \frac{A}{6} \frac{R_1 R_2}{R_1 + R_2} \frac{A_{ts}}{\nu A_{os} F_{ts}^a}. \tag{8.7}$$

The distance between an object and an obstacle must be larger than D_{min} during manipulation. If there is an obstacle which is close or on the straight line, the path formed by the straight line is not considered as a straight path. For example, the path between O2 and D1 in Figure 8.6 is not a direct path due to attraction. This means any obstacle cannot block the connection between an object and a destination if there is a direct path.

Virtual Objects and Destinations

After the direct paths are generated, objects are assigned to the destinations one by one. One object is assigned to one destination and vice verse. After the objects are assigned to the destinations, there are some destinations which may not have any objects assigned to them. Thus, paths that avoid the obstacles have to be generated. In nano-manipulation, the scanning time is much longer than the manipulation time. A surface has to be scanned again if an object is lost during manipulation. Therefore, the planned path should avoid losing objects during manipulation. A path with turns as shown in Figure 8.8 with much higher possibility of losing objects than a direct path. Therefore turns should be avoided during nanomanipulation.

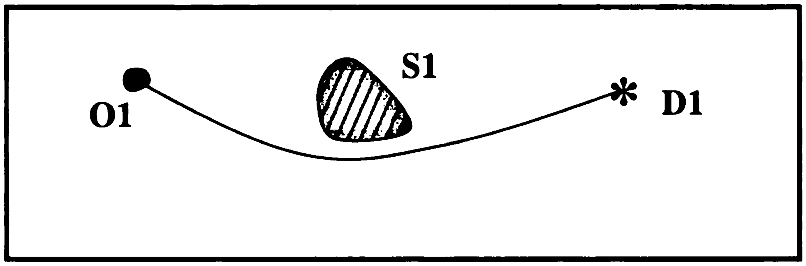

Figure 8.8: An object may be lost during turns. O1 is an object; D1 a destination and S1 an obstacle

A virtual object and destination algorithm is developed to solve the problem. Figure 8.9 shows a virtual object and destination (VOD).

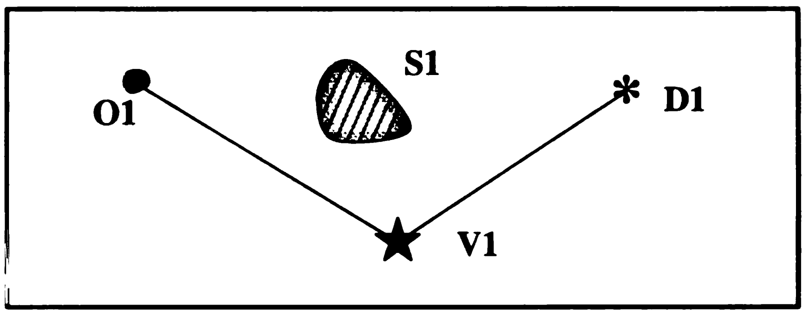

Figure 8.9: A virtual object and destination (VOD) connects an object and a destination. O1 is an object; D1 a destination; S1 an obstacle and V1 a VOD.

The object and the destination are connected using direct paths through the VOD. Since there are many possible VODs to connect an object and a destination, minimum distance criterion is applied to find the minimum distance VOD. The total distance to connect an object and a destination is,

$$d = \sqrt{(x_2 - x_0)^2 + (y_2 - y_0)^2} + \sqrt{(x_2 - x_1)^2 + (y_2 - y_1)^2} \tag{8.8}$$

where x_2, y_2 are the coordinates of the center of a VOD; x_0, y_0 the coordinates of the center of an object; x_1, y_1 the coordinates of the center of a destination.

The connections between the VOD, object and destination have to avoid the obstacles, i.e.,

$$\sqrt{(x-x_s)^2+(y-y_s)^2} \geq D_{min}+R_1+R_2 \tag{8.9}$$

where x, y are the coordinates of the object center along the path; x_s, y_s the coordinates of the center of the obstacle. Then a constrained optimization problem is formulated:

$$\begin{aligned} \min_{x_2,y_2} \; d = & \sqrt{(x_2-x_0)^2+(y_2-y_0)^2}+ \\ & \sqrt{(x_2-x_1)^2+(y_2-y_1)^2} \\ \text{subject to: } & \sqrt{(x-x_s)^2+(y-y_s)^2} \geq D_{min}+R_1+R_2 \;. \end{aligned} \tag{8.10}$$

This is a constrained optimization problem. A quadratic loss penalty function method [58] is adopted to deal with the constrained optimization problem. This method formulates a new function $G(\boldsymbol{x})$:

$$\min_{x_2,y_2} G = \min_{x_2,y_2} \; d + \beta\,(min[0,g])^2 \tag{8.11}$$

where β is a big scalar and g is formulated using the given constraints, i.e.,

$$g = \sqrt{(x-x_s)^2+(y-y_s)^2} - (D_{min}+R_1+R_2). \tag{8.12}$$

Then the constrained optimization problem is transferred into an unconstrained one using the quadratic loss penalty function method. The pattern search method [59] is adopted here to optimize the unconstrained optimization problem to obtain the VOD.

If one VOD cannot reach an unassigned destination, two or more Vods can be found to connect the object and destination. Figure 8.10 illustrates the process.

Similarly, a constrained optimization problem can be formulated to compute the

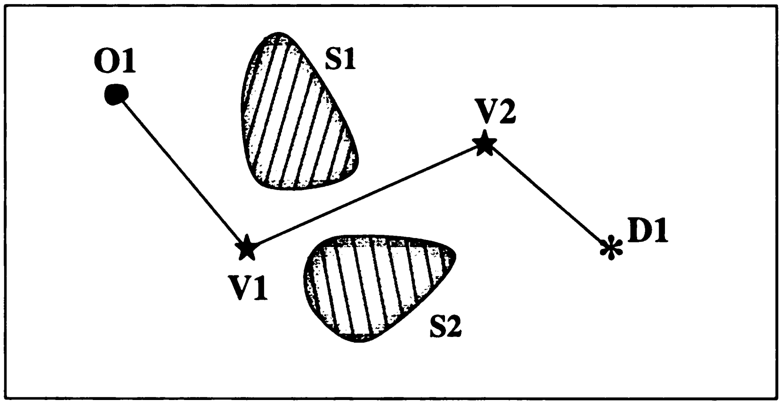

Figure 8.10: Two VODs connect an object with a destination. O1 is an object; D1 the destination; S1 and S2 are obstacles.

VODs.

Path Connection

When an object is manipulated to a destination, the destination becomes an obstacle (Destination Obstacle). Before an object is pushed to a destination, it could be an obstacle for other objects (Object Obstacle). The following definitions are used to find a collision-free path for nanomanufacturing.

Definition 8.2.1 Object Priority Index (OPI) *of an object is the number of objects, which are obstacles along the path between the object and a destination.*

The minimum OPI (MOPI) is 0.

Definition 8.2.2 Destination Priority Index (DPI) *of a destination is the number of destinations, which are obstacles along the path between the destination and an object.*

For a destination, minimum destination priority index (MDPI) can be defined.

Definition 8.2.3 The MDPI *of a destination is the minimum DPI among all DPIs.*

For all destinations, the maximum MDPI (MMDPI) can be found.

Definition 8.2.4 The MMDPI *is the maximum value of all MDPIs.*

Criterion: The destination with the MMDPI is filled with an object with the highest priority.

The following theorem can then be formulated:

Theorem 8.2.1 *There is no obstacle between an object with MOPI and a destination with MMDPI.*

Proof. According to the direct path, there is no actual obstacle between them.

If there is an object obstacle O between the object A and destination V as shown in Figure 8.11(a), then the OPI of O must be less than that of A. This is contrary to that the OPI of A is the minimum.

If there is an destination obstacle D between them as shown in Figure 8.11(b), D must be filled before V. According to the Criterion, the MDPI of D must be larger than that of V. This is contrary to that the MDPI of V is the maximum. ◁

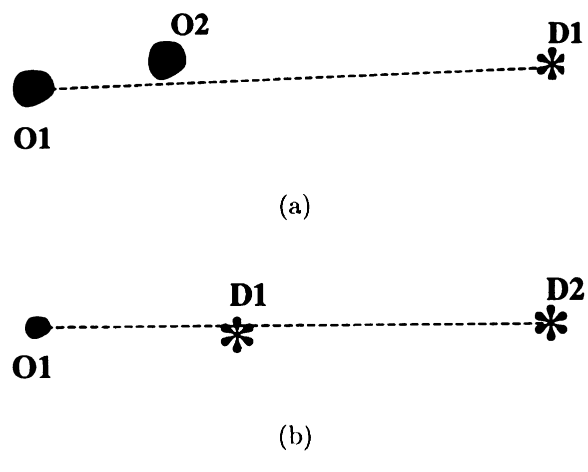

Figure 8.11: (a) Object obstacle; (b) Destination obstacle.

In path generation, the objects are assigned to the destinations using the minimum distance temporarily. Assume the number of objects is larger than or equal to that of destinations. One object is assigned only to one destination and vice versa. After that, destinations with MMDPI are found first. Then one of the destinations is chosen and one object with MOPI to the destination is assigned to it. Figure 8.12 shows the process to assign an object to a destination.

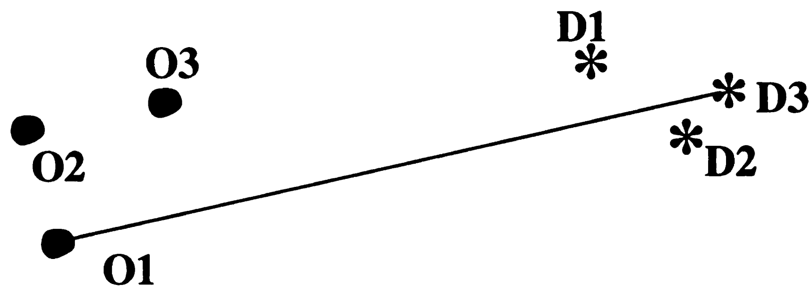

Figure 8.12: The assignment of an object to a destination.

After an object is assigned to a destination, a path is generated. Then all of the indices are updated and the path generation algorithm is applied again to generate another path. The process continues until all destinations are assigned. The path generation process of planning an AFM tip path is summarized in Figure 8.13.

All direct paths from objects to destinations are generated first. Then the objects are assigned to the destinations. If there are some destinations that are not assigned, VODs are generated. After that, a collision-free path is generated. Then the path is checked if there are any destination obstacles. If there are, the destination should be inserted before the obstacle destinations. Then the process continues until all destinations are assigned.

8.2.5 Implementation and Testing

The developed algorithm is implemented to generate paths to manipulate nanoparticles to manufacture nanostructures. The CAD models of two nanostructures are shown in Figures 8.14(a) and 8.14(b).

Two samples with 100 *nm* latex particles are prepared to perform the nanomanufacturing. Figure 8.15 shows two images taken by an AFM.

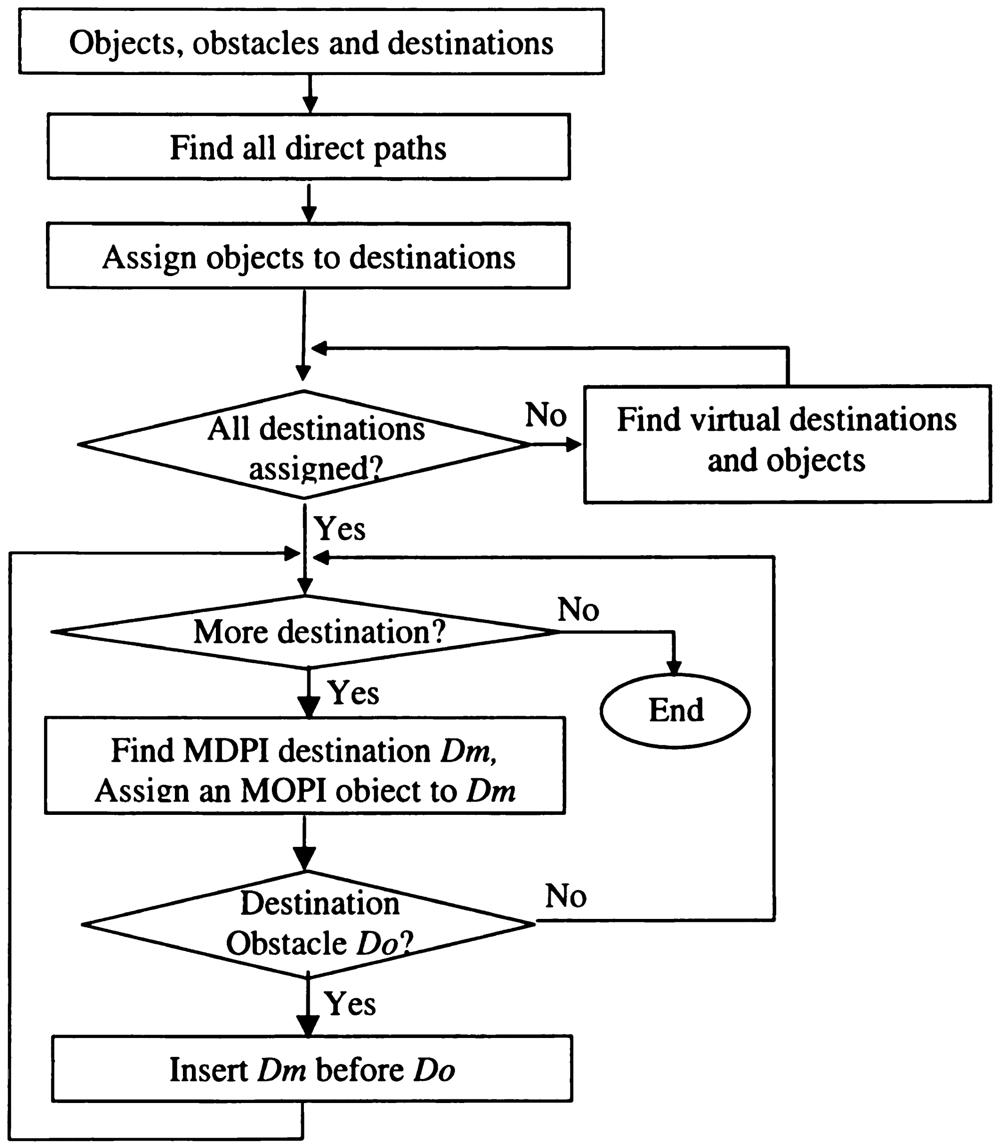

Figure 8.13: Path generation algorithm.

After applying the algorithms, objects and obstacles are identified. Two collision-free paths are generated. The simulation results show that there is no collision. Then the generated paths are implemented to control the AFM tip to perform the nanomanufacturing. The real-time images are shown in Figures 8.16(a) and 8.16(b), respectively.

After the processes are complete, the surfaces are re-scanned to check the actual results. Figures 8.17(a) and 8.17(b) show the actual manufactured nanostructures.

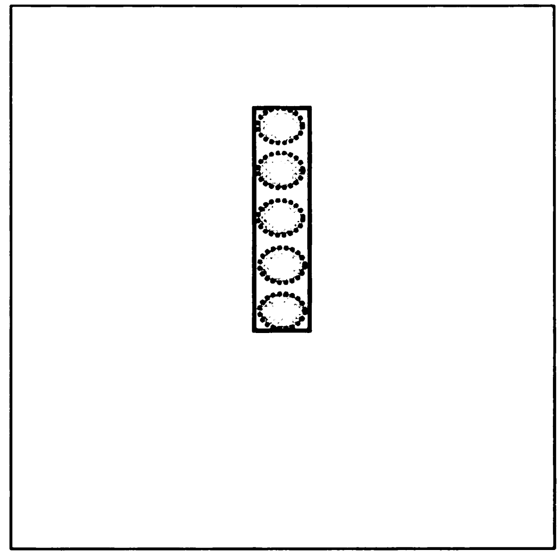

(a)

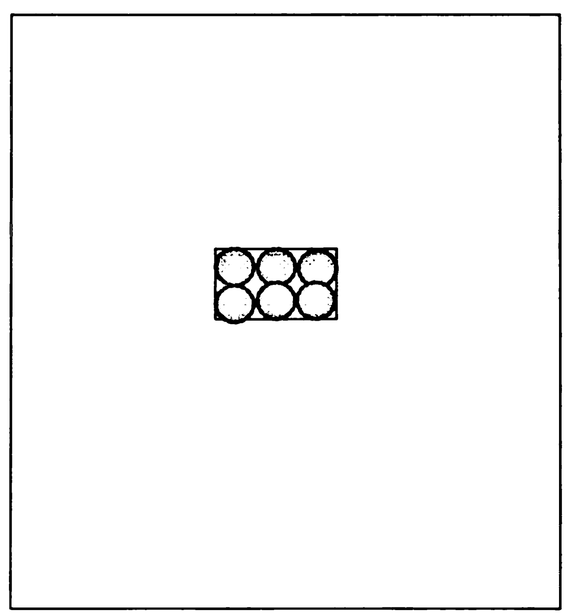

(b)

Figure 8.14: The CAD models of two nanostructures: (a) a line; (b) a rectangular.

The results are consistent with the real-time image shown in 8.16(a) and 8.16(b), respectively. In Figure 8.17(b), the objects are attracted together because the distances between the objects are smaller than the minimum distance D_{min}. The van der Waals

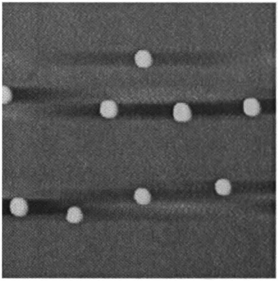

(a)

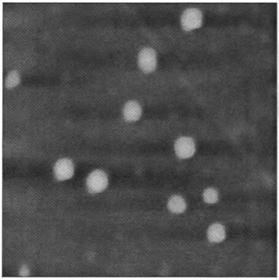

(b)

Figure 8.15: The AFM images with nanoparticles to manufacture: (a) a line; (b) a rectangular.

force attracts the particles closer.

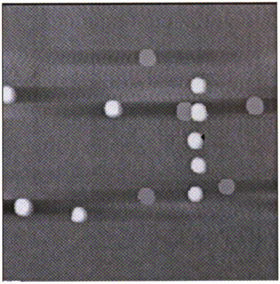

(a)

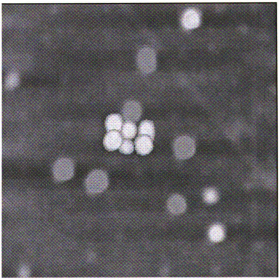

(b)

Figure 8.16: The real-time AFM images in the augmented reality system with manufactured nanostructures: (a) a line; (b) a rectangular.

8.3 Conclusion

The developed general framework of automated tool path planning has been implemented successfully to manufacture nanostructures in nanomanufacturing. The

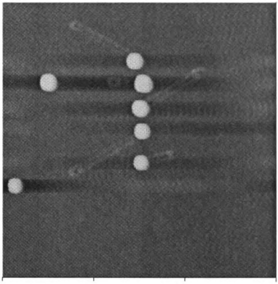

(a)

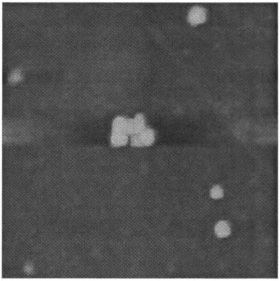

(b)

Figure 8.17: The manufactured nanostructures: (a) a line; (b) a rectangular.

collision-free paths have been generated using the CAD-guided automated path planning algorithm. Simulations have been performed to verify the generated paths. Experiments to manufacturing nanostructures have been implemented successfully and achieved satisfactory results. The simulation and experimental results show that the developed CAD-guided tool path planning system can be applied to manufacture nanostructures and nanodevices.

CHAPTER 9

CONCLUSIONS

A general framework for CAD-guided optimal tool planning in surface manufacturing has been developed and implemented successfully. In this chapter, the conclusions and the extensions of this framework are discussed.

9.1 Conclusions

Tool planning builds communication between the CAD model of a part and the product manufactured based on the CAD design. Automated tool planning process is highly desirable in today's manufacturing. A general framework of automated tool planning for surface manufacturing is developed based on the CAD model of a free-form surface, a tool model and constraints. Both material uniformity and coverage are considered in one constraint. Since different material deposition patterns are used in tool planning, a comparison between the raster and spiral material deposition patterns is made. The implementation results show that the raster material deposition pattern is better than the spiral one for continuous material deposition. A free-form surface is divided into one or several patches using the patch forming algorithm such that the given constraints are satisfied. The improved bounding box method has been implemented to generate a tool trajectory for a patch. To integrate the trajectories of the patches in a free-form surface, a trajectory integration algorithm has been developed. The tool orientation is determined based on the local geometry of a free-form surface. The automated tool planning algorithm is implemented to generate trajectories for different parts in different applications. Simulations are performed to compute the material deposition on free-form surfaces, and the results show that the generated trajectories satisfy the given constraints. A suboptimal velocity algorithm is developed to minimize the material thickness deviation from the required material constraints. Simulation results show that the automated tool planning algorithm can be applied to generate a trajectory for a free-form surface to satisfy the given constraints.

A general framework for optimal tool planning in surface manufacturing has also been developed based on the CAD model of a free-form surface, a tool model, constraints and optimization criteria. Multi-objective constraint optimization problems have been formulated. After the optimal tool planning algorithm is developed, simulations have been performed for the optimal tool planning with optimal time, optimal material distribution, no preference articulation and preference articulation. Simulation results for the four cases are presented and compared. The simulation results are consistent with theoretical analysis.

The developed general framework of automated CAD-guided tool planning and optimal tool planning has been implemented successfully. The developed tool trajectory planning algorithm has been tested in the Ford Motor Company and can greatly decrease the cost and increase the efficiency.

9.2 Extensions to Other Applications

The developed general framework has been extended to other applications such as dimensional inspection and nanomanufacturing.

Dimensional inspection is an important process in the manufacturing industry. It is highly desirable to develop a camera positioning system that is able to plan and realize the camera configurations in a fully-automated, accurate and efficient way. The general framework of automated tool planning and optimal tool planning has been applied to generate a camera path for the dimensional inspection of a part.

Nanotechnology, a promising, advanced technology for the forthcoming century, has been a recent hot research topic. The complexity of nanomanufacturing requires to position, manipulate, assemble nanoparticles to manufacture nanostructures, nanodevices and nanosensors. The general framework of automated tool planning has been applied to generate paths to manufacture nanostructures and nanodevices. Experimental results show satisfactory results.

The general framework can also be extended to other similar applications, such as demining [43, 60].

APPENDIX A

MULTI-OBJECTIVE CONSTRAINED OPTIMIZATION

In this appendix, a multi-objective constrained optimization problem is presented and the algorithm to solve the problem is discussed.

A.1 A Multi-objective Constrained Optimization Problem

A general multi-objective constrained optimization problem can be formulated using the objective functions, constraints and optimization parameters (decision variables), i.e.,

$$\begin{aligned}
&min\boldsymbol{F}(\boldsymbol{x}) = (f_1(\boldsymbol{x}), f_2(\boldsymbol{x}), ..., f_k(\boldsymbol{x}))^T \\
&\text{subject to: } \boldsymbol{e(x)} = (e_1(\boldsymbol{x}), e_2(\boldsymbol{x}), ..., e_m(\boldsymbol{x}))^T \text{ with } e_i(\boldsymbol{x}) \geq 0, \ i = 1, ..., m \\
&\boldsymbol{x} = (x_1, x_2, ..., x_n)^T
\end{aligned} \tag{A.1}$$

where $f_1(\boldsymbol{x}), f_2(\boldsymbol{x}), ..., f_k(\boldsymbol{x})$ are k objective functions; $(x_1, x_2, ..., x_n)$ n optimization parameters and $e_1(\boldsymbol{x}), e_2(\boldsymbol{x}), ..., e_m(\boldsymbol{x})$ m constraints.

The utopian solution is a set of minima of each respective objective function subject to the given constraints, i.e.,

$$F^* = (f_1^*, f_2^*, ..., f_k^*)^T \tag{A.2}$$

where $f_1^*, f_2^*, ..., f_k^*$ are the individual minima of the objective functions.

A.2 Optimization Method

There are different methods to perform the multi-objective optimization [61, 62, 63], such as weighted-sum approach, no preference articulation, nonlinear approach, utility theory, goal programming and STEM method [64]. No preference articulation method does not use any preference information. It is based on minimization of the relative distance from a candidate solution to the utopian solution, i.e.,

$$
\begin{aligned}
& minF(\boldsymbol{x}) = \left[\sum_{j=1}^{k}\left(\frac{f_j(\boldsymbol{x}) - f_j^*}{f_j^*}\right)^p\right]^{\frac{1}{p}} \\
& \text{subject to: } \boldsymbol{e(x)} = (e_1(\boldsymbol{x}), e_2(\boldsymbol{x}), ..., e_m(\boldsymbol{x}))^T \text{ with } e_i(\boldsymbol{x}) \geq 0,\ i = 1, ..., m \\
& \boldsymbol{x} = (x_1, x_2, ..., x_n)^T
\end{aligned} \tag{A.3}
$$

The most frequently used value for p is 1 [64]. Equation (A.3) can be transferred to:

$$
\begin{aligned}
& minF_1(\boldsymbol{x}) = \sum_{j=1}^{k} \lambda_j f_j(\boldsymbol{x}) \\
& \text{subject to: } \boldsymbol{e(x)} = (e_1(\boldsymbol{x}), e_2(\boldsymbol{x}), ..., e_m(\boldsymbol{x}))^T \text{ with } e_i(\boldsymbol{x}) \geq 0,\ i = 1, ..., m \\
& \boldsymbol{x} = (x_1, x_2, ..., x_n)^T
\end{aligned} \tag{A.4}
$$

where λ_j is defined as:

$$\lambda_j = \frac{1}{f_j^*} \tag{A.5}$$

After applying the no preference articulation approach, the multi-objective constrained problem is transferred into a single objective constrained problem. A quadratic loss penalty function method [58] is adopted to deal with the constrained problem. A new function $G(\boldsymbol{x})$ is formulated as:

$$minG(\boldsymbol{x}) = F_1(\boldsymbol{x}) + \beta \sum_{i=1}^{m} (min[0, e_i(\boldsymbol{x})])^2 \tag{A.6}$$

where β is a big scalar. Thus a constrained optimization problem is transferred into an unconstrained one using the quadratic loss penalty function method. Finally, a single objective unconstrained problem is formulated. The simplex method [59] is adopted to solve the single objective unconstrained problem.

AUTHOR'S PUBLICATION

1 H. Chen, N. Xi, W. Sheng, M. Song, Y. Chen. CAD-Based Automated Robot Trajectory Planning for Spray Painting of Free-Form Surfaces. *An International Journal of Industrial Robot*, 29(5):426-433, 2002.

2 H. Chen, N. Xi, Y. Chen, J. Dahl. CAD-Guided Spray Gun Trajectory Planning of Free-Form Surfaces in Manufacturing. *Journal of Advanced Manufacturing Systems*, 2(1):47-69, June 2003.

3 H. Chen, N. Xi, W. Sheng, Y. Chen. A General Framework of CAD-Guided Optimal Tool Planning for Free-form Surfaces in Surface Manufacturin. *The ASME Journal of Manufacturing Science and Engineering.*

4 H. Chen, N. Xi, S. K. Masood, Y. Chen. Software Development of Automated Chopper Gun Trajectory Planning for Spray Forming. *An International Journal of Industrial Robot.*

5 H. Chen, W. Sheng, N. Xi, M. Song, Y. Chen. CAD-Guided Uniformity Guaranteed Robot Trajectory Planning for Spray Painting of Free Form Surfaces . *IEEE International Conference on Mechatronics and Machine Vision in Practice 2001*, HongKong.

6 H. Chen, W. Sheng, N. Xi, M. Song, Y. Chen. Automated Robot Trajectory Planning for Spray Painting of Free-Form Surfaces in Automotive Manufacturing. *the International Conference on Robotics and Automation*, 2002, Washington D.C..

7 H. Chen, N. Xi, W. Sheng, Y. Chen, A. Roche, J. Dahl. A General Framework for Automatic CAD-Guided Tool Planning for Surface Manufacturing. *The International Conference on Robotics and Automation*, 2003.

8 H. Chen, N. Xi, Z. Wei, Y. Chen, J. Dahl. Robot Trajectory Integration for Painting Automotive Parts with Multiple Patches. *The International Conference on Robotics and Automation*, 2003.

9 H. Chen, N. Xi, Y. Chen. Multi-objective Optimal Robot Path Planning in Manufacturing, *IEEE/RSJ International Conference on Intelligent Robots and Systems*, 2003.

10 W. Sheng, N. Xi, H. Chen, M. Song and Y. Chen. Surface Partitioning in Automated CAD-Guided Tool Planning for Additive Manufacturing. *IEEE/RSJ International Conference on Intelligent Robots and Systems*, 2003.

11 W. Sheng, N. Xi, H. Chen, M. Song and Y. Chen. Part Geometric Understanding for Tool Path Planning in Additive Manufacturing. *IEEE International Symposium on Computational Intelligence in Robotics and Automation*, 2003.

12 H. Chen, N. Xi, W. Sheng, Y. Chen and J. Dahl. Chopper Gun Trajectory Integration for Spray Forming in Automotive Manufacturing. *The 8th International Conference on Numerical Methods in Industrial Forming Processes (NUMIFORM)*, 2004.

13 W. Sheng, H. Chen, N. Xi, M. Song and Y. Chen. Optimal tool path planning for compound surfaces in spray forming processes. *The International Conference on Robotics and Automation*, 2004.

14 H. Chen, N. Xi, W. Shen, Y. Chen. Automated Chopper Gun Trajectory Planning for Variational Distribution in Spray Forming. *The International Conference on Robotics and Automation*, 2004.

15 G. Li, N. Xi, H. Chen. A. Saeed, M. Yu. Assembly of Nanostructure Using AFM Based Nanomanipulation. *The International Conference on Robotics and Automation*, 2004.

16 Q. Shi, N. Xi, H. Chen,Y. Chen. Automated Dimensional Inspection of Automotive Parts by An Area Sensor. *The 2004 Japan USA Symposium on Flexible Automation (JUSFA)*, 2004.

17 H. Chen, N. Xi and Y. Chen. Theoretical Comparison of Raster and Spiral Tool Patterns for Material Deposition in Surface Manufacturing. *The 2004 Japan USA Symposium on Flexible Automation (JUSFA)*, 2004.

18 H. Chen, N. Xi, G. Li, A. Saeed and J. Zhang. Automated Assembly of Complicated Nanodevices Using Atomic Force Microscopy. *The 4th IEEE Conference on Nanotechnology*, 2004.

19 G.Y. Li, N. Xi, H. Chen, A. Saeed, W.J. Li, C.K.M. Fung, R.H.M. Chan, M. Zhang and T.-J. Tarn. Nano-assembly of DNA Based Electronic Devices Using Atomic Force Microscopy. *The IEEE/RSJ International Conference on Intelligent Robotics and Systems*,2004.

20 G.Y. Li, N. Xi, H. Chen, A. Saeed, J. B. Zhang, W.J. Li, C.K.M. Fung, R.H.M. Chan, M. Zhang and T.-J. Tarn. Experimental Studies of DNA Electrical Properties Using AFM Based Nano-Manipulator. *The 4th IEEE Conference on Nanotechnology*, 2004.

BIBLIOGRAPHY

[1] H. C. Zhang and L. Alting. *Computerized Manufacturing Process Planning Systems.* Chapman & Hall, London ; New York, 1994.

[2] H. Lau and B. Jiang. A generic integrated system for CAD to CAPP: a neutral file-cum-GT approach. *Computer Integrated Manufacturing Systems*, 11(1):67–75, 1998.

[3] R. Lee, Y. Chen, H. Cheng, and M. Kun. A framework of a concurrent process planning system for mold manufacturing. *Computer Integrated Manufacturing Systems*, 11(3):171–190, 1998.

[4] Y. Yang, H. T. Loh, J. Y. H. Fuh, and Y. G. Wang. Equidistant path generation for improving scanning efficiency in layered manufacturing. *Rapid Prototyping Journal*, 8(1):30–37, 2002.

[5] D. Dutta, V. Kumar, M. J. Pratt, and R. D. Sriram. Towards STEP-based data transfer in layered manufacturing. In *Proceedings of the Tenth International IPFP WG5.2/5.3 Conference PROLAMAT 98*, 1998.

[6] Y. K. Hwang, L. Meirans, and W. D. Drotning. Motion planning for robotic spray cleaning with environmentally safe solvents. In *IEEE/Tsukuba International Workshop on Advanced Robots*, pages 49–54, Tsukuba, Japan, Nov. 1993.

[7] N. Asakawa and Y. Takeuchi. Teachingless spray-painting of sculptured surface by an industrial robot. In *IEEE International Conference on Robotics and Automation*, pages 1875–1879, Albuquerque, New Mexico, April 1997.

[8] J. K. Antonio, R. Ramabhadran, and T. L. Ling. A framework for optimal trajectory planning for automated spray coating. *International Journal of Robotics and Automation*, 12(4):124–134, 1997.

[9] S. Suh, I. Woo, and S. Noh. Automatic trajectory planning system (ATPS) for spray painting robots. *Journal of Manufacturing Systems*, 10(5):396–406, 1991.

[10] J. K. Antonio. Optimal trajectory planning for spray coating. In *IEEE International Conference on Robotics and Automation*, pages 2570–2577, San Diego, California, May 1994.

[11] Painting Package. *CimStation User's Manual.* Silma, Inc., 1992.

[12] Painting Package. *IGRIP User's Manual.* Deneb Robotics, Inc., 1992.

[13] Tecnomatix. *ROBCAD/Paint Training.* Tecnomatix, Michigan, USA, 1999.

[14] N. G. Chavka and J. Dahl. P4 preforming technology: Development of a high volume manufacturing method for fiber preforms. In *ACCE/ESD: Advanced Composite Conference Proceedings*, September 1998.

[15] L. F. Penin, C. Balaguer, J. M. Pastor, F. J. Rodriguez, A. Barrientos, and R. Aracil. Robotized spraying of prefabricated panels. *IEEE Robotics and Automation Magazine*, 5(3):18–29, 1998.

[16] C. C. Kai and L. K. Fai. *Rapid Prototyping: Principles and Applications in Manufacturing.* John Wiley & Sons, Inc., New York, USA, 1997.

[17] R. E. Chalmers. Rapid tooling technology from Ford Country. *Manufacturing Engineering*, pages 36–38, Nov. 2001.

[18] R. C. Luo and J. H. Tzou. Investigation of a linear 2-d planar motor based rapid tooling. In *IEEE International Conference on Robotics and Automation*, pages 1471–1476, Washington, DC, USA, May 2002.

[19] K. A. Tarabanis. Path planning in the proteus rapid prototyping system. *Rapid Prototyping Journal*, 7(5):241–252, 2001.

[20] W. Sheng, N. Xi, M. Song, Y. Chen, and P. MacNeille. Automated CAD-guided robot path planning for spray painting of compound surfaces. In *IEEE/RSJ International Conference on Intelligent Robots and Systems*, pages 1918–1923, Takamutsa, Japan, October 2000.

[21] W. H. Huang. Optimal line-sweep-based decompositions for coverage algorithm. In *IEEE International Conference on Robotics and Automation*, pages 27–32, Seoul, Korea, May 2001.

[22] Y. Mizugaki, M. Sakamoto, and K. Kamijo. Fractal path application in a metal mold polishing robot system. In *Fifth International Conference on Advanced Robotics*, pages 431–436, Pisa, Italy, June 1991.

[23] Y. Takeuchi, D. Ge, and N. Asakawa. Automated polishing process with a human-like dexterous robot. In *IEEE*, pages 950–956, Barcelona, Spain, Oct. 1993.

[24] H. Hyotyniemi. Locally controlled optimization of spray painting robot trajectories. In *Proceedings of the IEEE International Workshop on Intelligent Motion Control*, pages 283–287, Istanbul, Turkey, August 1990.

[25] H. Hyotyniemi. Minor moves-global results: robot trajectory planning. In *Proceedings of the 2nd International IEEE Conference on Tools for Artificial Intelligence*, pages 16–22, Herndon, Virginia, Nov. 1990.

[26] R. Ramabhadran and J. K. Antonio. Fast solution techniques for a class of optimal trajectory planning problems with application to automated spray coating. *IEEE Transactions on Robotics and Automation*, 13(4):519–530, August 1997.

[27] J. Y. Lai and D. J. Wang. A strategy for finish cutting path generation of compound surface. *Computers in industry*, 25:189–209, 1994.

[28] W. Sheng. *CAD-based Robot Motion Planning for Inspection in Manufacturing.* Ph. D. Dissertation, Michigan State University, Michigan, USA, 2002.

[29] T. C. Chang, R. A. Wysk, and H. P. Wang. *Computer-aided manufacturing: second edition.* Prentice Hall, New Jersey, 1998.

[30] J. J. Shah and M. Mantyla. *Parametric and Feature-based CAD/CAM: concepts, techniques and applications.* John Wiley & Sons, Inc., New York, 1995.

[31] E. Freund, D. Rokossa, and J. Rossmann. Process-orientated approach to an efficient off-line programming of industrial robots. In *Proceedings of the 24th Annual Conference of the IEEE Industrial Electronics Society, IECON '98.*, volume 1, pages 208–213, 1998.

[32] W. Persoons and H. Van Brussel. CAD-based robotic coating with highly curved surfaces. In *International Symposium on Intelligent Robotics (ISIR'93)*, volume 14, pages 611–618, 1993.

[33] P. Hertling, L. Hog, R. Larsen, J. W. Perram, and H. G. Petersen. Task curve planning for painting robots: I. process modeling and calibration. *IEEE Transactions on Robotics and Automation*, 12(2):324–330, April 1996.

[34] E. D. Goodman and L. T. W. Hoppensteradt. A method for accurate simulation of robotic spray application using empirical parameterization. In *IEEE International Conference on Robotics and Automation*, volume 2, pages 1357–1368, Sacramento, California, April 1991.

[35] S. S. Rao. *Optimization: Theory and Application.* John Wiley & Sons, Inc., New York, USA, 1983.

[36] J. Kao and F. B. Prinz. Optimal motion planning for deposition in layered manufacturing. In *Proceedings of DETC'98 1998 ASME Design Engineering Technical Conferences*, Atlanta, Georgia, September 1998.

[37] W. Sheng, H. Chen, N. Xi, M. Song, and Y. Chen. Optimal tool path planning for compound surfaces in spray forming processes. In *submitted to the International Conference on Robotics and Automation*, 2004.

[38] M. A. A. Arikan and T. Balkan. Process modeling, simulation, and paint thickness measurement for robotic spray painting. *Journal of Robotic Systems*, 17(9):479–494, 2000.

[39] D. C. Conner, P. N. Atkar, A. A. Rizzi, and H. Choset. Development of deposition models for paint application on surfaces embedded in r^3 for use in automated path planning. In *IEEE/RSJ International Conference on Intelligent Robots and Systems*, pages 1844–1849, Lausanne, Switzerland, Oct. 2002.

[40] A. H. Lefebvre. *Atomization and sprays.* Hemisphere Publishing, New York, 1989.

[41] S. H. Suh, I. K. Woo, and S. K. Noh. Development of an automatic trajectory planning system(atps) for spray painting robots. In *IEEE International Conference on Robotics and Automation*, pages 1948–1955, Sacramento, California, April 1991.

[42] S. N. Spitz and A. A. G. Requicha. Hierchical constraint satisfaction for high-level dimensional inspection planning. In *Proceedings of the 1999 IEEE international Symposium on Assembly and Task Planning*, pages 374–380, 1999.

[43] Y. J. Lee and S. Hirose. Three-legged walking for fault tolerant locomotion of a quadruped robot with demining mission. In *IEEE/RSJ International Conference on Intelligent Robots and Systems*, pages 973–978, Takamatsu, Japan, Nov. 2000.

[44] G. Hu and G. Stockman. 3-d surface solution using structured light and constraint propagation. *IEEE transaction on pattern analysis and machine intelligence*, 11(4):390–402, 1989.

[45] H. McNally, M. Pingle, S. W. Lee, D. Guo, D. E. Bergstorm, and R. Bashir. Self-assembly of micro- and nano-scale particles using bio-inspired events. *Applied Surface Science*, pages 109–119, 2003.

[46] G. Binning, C. F. Quate, and C. Gerber. Atomic force microscope. *Physical Review Letters*, Vol. 56(9):930–933, 1986.

[47] D. M. Schaefer, R. Reifenberger, A. Patil, and R. P. Andres. Fabrication of two-dimensional arrays of nanometer-size clusters with the atomic force microscope. *Applied Physics Letters*, Vol. 66:1012–1014, February 1995.

[48] T. Junno, K. Deppert, L. Montelius, and L. Samuelson. Controlled manipulation of nanoparticles with an atomic force microscope. *Applied Physics Letters*, Vol. 66(26):3627–3629, June 1995.

[49] A. A. G. Requicha, C. Baur, A. Bugacov, B. C. Gazen, B. Koel, A. Madhukar, T. R. Ramachandran, R. Resch, and P. Will. Nanorobotic assembly of two-dimensional structures. In *Proc. IEEE Int. Conf. Robotics and Automation*, pages 3368–3374, Leuven, Belgium, May 1998.

[50] L. T. Hansen, A. Kuhle, A. H. Sorensen, J. Bohr, and P. E. Lindelof. A technique for positioning nanoparticles using an atomic force microscope. *Nanotechnology*, Vol. 9:337–342, 1998.

[51] G. Y. Li, N. Xi, M. Yu, and W. K. Fung. 3-d nanomanipulation using atomic force microscope. In *Proc. IEEE Int. Conf. Robotics and Automation*, Taipei, Taiwan, Sep. 2003.

[52] M. Sitti and H. Hashimoto. Tele-nanorobotics using atomic force microscope. In *Proc. IEEE Int. Conf. Intelligent Robots and Systems*, pages 1739–1746, Victoria, B. C., Canada, October 1998.

[53] M. Guthold, M. R. Falvo, W. G. Matthews, S. washburn S. Paulson, and D. A. Erie. Controlled manipulation of molecular samples with the nanomanipulator. *IEEE/ASME Transactions on Mechatronics*, Vol. 5(2):189–198, June 2000.

[54] J. H. Makaliwe and A. A. G. Requicha. Automatic planning of nanoparticle assembly tasks. In *Proc. IEEE Int'l Symp. on Assembly and Task Planning*, pages 288–293, Fukuoka, Japan, May 2001.

[55] G. Y. Li, N. Xi, M. Yu, and W. K. Fung. Augmented reality system for real-time nanomanipulation. In *Proc. IEEE Int. Conf. Nanotechnology*, San Francisco, CA, August 12-14 2003.

[56] J. Israelachvili. *Intermolecular and surface forces.* Academic Press London, London, UK, 1991.

[57] G. Y. Li, N. Xi, M. Yu, and W. K. Fung. Modeling of 3d interactive forces in nanomanipulation. In *IEEE/RSJ International Conference on Intelligent Robots and Systems*, Las Vegas, November 2003.

[58] P. M. Garth. *Nonlinear programming: theory, algorithm and applications.* John Wiley & Sons, Inc., New York, 1983.

[59] M. Avriel. *Nonlinear Programming: Analysis and Methods.* Prentice-Hall Inc., Englewood Cliffs, NJ, USA, 1976.

[60] J. D. Nicoud and M. K. Habib. The pemex-b autonomous demining robots perception and navigation strategies. In *IEEE/RSJ International Conference on Intelligent Robots and Systems*, pages 419–424, Pittsburgh, PA, USA, Aug. 1995.

[61] C. Hwang, S. Paidy, and K. Yoon. Mathematical programming with multiple objectives: a tutorial. *Computer & Operations Research*, 7:5–31, 1980.

[62] R. Steuer. *Multiple criteria optimization: theory, computation and application.* John Wiley & Sons, Inc., New York, 1986.

[63] H. Eschenauer, J. Koski, and A. Osyczka. *Multicriteria design optimization.* Springer-Verlag, Berlin, 1990.

[64] J. Andersson. A survey of multiobjective optimization in engineering design. Technical Report LiTH-IKP-R-1097, Department of Mechanical Engineering, Linköping University, Linköping, Sweden, 2000.